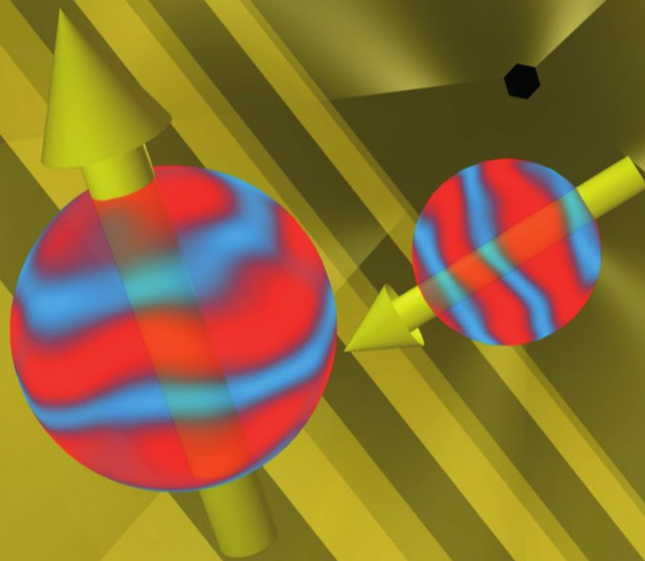


# Single Spins in Semiconductor Nanowires



Stevan Nadj-Perge

SINGLE SPINS IN SEMICONDUCTOR  
NANOWIRES



# SINGLE SPINS IN SEMICONDUCTOR NANOWIRES

## Proefschrift

ter verkrijging van de graad van doctor  
aan de Technische Universiteit Delft,  
op gezag van de Rector Magnificus prof. ir. K. C. A. M. Luyben,  
voorzitter van het College voor Promoties,  
in het openbaar te verdedigen op maandag 20 december 2010 om 15:00 uur

door

**Stevan NADJ-PERGE**

Diplomirani fizičar, Univerzitet u Beogradu, Srbija  
geboren te Kikinda, Servië.

Dit proefschrift is goedgekeurd door de promotor:

Prof. dr. ir. L. P. Kouwenhoven

Samenstelling van de promotiecommissie:

Rector Magnificus	voorzitter
Prof. dr. ir. L. P. Kouwenhoven	Technische Universiteit Delft, promotor
Prof. dr. C. W. J. Beenakker	Universiteit Leiden
Prof. dr. K. Ensslin	Eidgenössische Technische Hochschule Zürich, Switzerland
Prof. dr. Yu. V. Nazarov	Technische Universiteit Delft
Prof. dr. ir. B. J. van Wees	Rijksuniversiteit Groningen
Prof. dr. ir. L. M. K. Vandersypen	Technische Universiteit Delft
Dr. G. A. Steele	Technische Universiteit Delft
Prof. dr. H. W. M. Salemink	Technische Universiteit Delft, reservelid



*Keywords:* Nanowire, spin, qubit

*Printed by:* Gildeprint, Enschede

*Cover design:* Gemma Plum (back) and Stevan Nadj-Perge (front)

*Cover image:* (front) Two spins inside InAs nanowire; (back) Spin-orbit qubit – a quantum yo-yo;

Copyright © 2010 by S. Nadj-Perge

Casimir PhD Series, Delft-Leiden, 2010-31

ISBN 9789461081179

An electronic version of this dissertation is available at  
<http://repository.tudelft.nl/>.

# ACKNOWLEDGMENTS

I still remember my amazement, after my interview for a PhD position here at QT. Discussions with so many enthusiastic people working on very different, but equally fascinating projects in one day was really great. I was extremely happy when I got an offer to do a PhD here. On the other hand, being trained in theoretical physics, but almost without any experimental skills, I knew that coming to work at QT would be a big change and a huge challenge. Only one thing was clear from the start: doing a PhD was going to be an interesting experience. Now, after four years spent mostly in the lab, more than 10000 km on my bike and a few dozen *kroketten*, I can honestly say that this was a great journey.

I would like to thank my promotor Leo Kouwenhoven for giving me the opportunity to do my PhD project in QT. Leo, I am really impressed by your ability to explain things in a very clear way, to always find new, interesting research directions, to get enough money for the research and at the same time run a big group such as QT. For the last two years, I have been working closely with Sergey Frolov. Sergey, your drive and enthusiasm still amaze me sometimes. I have learned so many things about physics, paper writing and physicists from you. I am sure you will soon get your dream job.

When I started my PhD project, we were mostly fabricating samples. Marc Scheffler and Juriaan van Tilburg - thank you for showing me the first tricks in the cleanroom and sharing the frustration when things did not go well. Marc, I still admire your enthusiasm towards physics and museums. Juriaan, good luck in your new career. This research would obviously not be possible without nanowires, whose growth, would not be possible without Erik Bakkers. Erik, it has been really nice working with you. I am sure you will keep inventing new and interesting nanowires in the future. I would also like thank Magnus Borgström, Rienk Algra and Moïra Hocevar - thank you for maintaining a constant supply of nanowires over the years.

During my PhD, I (co-)supervised three master students: Ji Li, Sneha Eashwer and Kun Zuo. I really learned a lot from you. Good luck with your

PhD research. I would also like to acknowledge former QT members working on InAs nanowires Jorden van Dam and Silvano DeFranceschi. I would also like to wish all the best to the new members who recently joined - Vlad Pribiag, Johan van den Berg, Kun Zuo, Ilse van Weperen and Vincent Mourik. Good luck with spin-orbit qubits and Majorana fermions.

QT is truly a great place to work. I thank Hans Mooij, Leo Kouwenhoven, Kees Harmans, Lieven Vandersypen, Ad Verbruggen, Ronald Hanson, Erik Bakkers, Val Zwiller and Leo DiCarlo for their positive contribution to the group. Besides very talented researchers, in order for research to run smoothly you also need a good support team to keep things going. Bram van der Enden, Remco Roeleveld, Peter van Oossanen and Jelle Haanstra - thank you for taking care never to run out of helium and for fixing broken things. Raymond Schouten, thanks to you the experiments in which we measure 5fA currents are possible. Your knowledge of electronics is truly fascinating. Yuki Nakagawa, Angèle Fontijn and Marja Plas - thank you for always taking care of the paperwork. Yuki, many thanks for teaching me how to deal with the Japanese embassy. Angèle, thanks for helping me make the "Le tour du monde en dix-sept jours" trip. Thanks also to Ria van Heeren-van der Kramer and Stephanie Hensing for valuable logistic help at very beginning and the very end of my PhD.

In the cleanroom you can also meet very helpful people. I would like to thank Arnold van Run, Marco van der Krogt, Anja van Langen, Marco Bakker, Emile van der Drift and Rael Matteredne for their help.

Being part of a group as large as QT gives the opportunity to meet people with different expertise and interests. Discussing an issue with them may help when your project is stuck or you need results really, really fast. And talking to them is always fun. I would like to thank Gary Steele for invaluable physics discussions and sharing your cleanroom expertise. Good luck with the vibrating nanotubes. Katja Nowack, the EDSR spin-qubit expert, you are definitely the most cheerful physicist I know. I really wonder which field of physics you will end up in. Gijs De Lange, thank you for the crash course in dynamical decoupling. Pieter de Groot, thanks for sharing your qubit and programming expertise. It was a pleasure talking to you. You and Reinier Heeres made really nice measurement software - thank you both for that. Han Keijzers, Georg Götze, Victor Calado, Toeno van der Sar, Hubert Heersche and Jelle Plantenberg - it was fun sharing office with you. Han - it was nice

being your roommate in Veldhoven, thanks for all discussions about life and physics. I wish you, Ionica and Tex all the best. Georg - you were my first flatmate in the Netherlands, I liked sharing a house with you. Toeno - you are a real entertainer, I am sorry that you left the office. Victor - good luck with moving graphene around. Hubert - thanks for the first wire bonding lesson. I want to thank the QT members for nice moments at the conferences, uitjes and in the lab: Maarten van Kouwen - good luck with your job search; Maarten van Weert - it was nice talking to you, I am sure you will be a great father; Lan Liu - QT misses you, I hope you enjoy in Eindhoven; Umberto Perinetti - good luck with writing; Ivo Vink, Frank Koppens, Lars Schreiber, Floris Braakman - thanks for all the discussions; Mohammad Shafiei, Pasquale Scarlino - good luck with the qubits; Tristan Meunier - thanks for discussions and your hospitality in Grenoble; Floris Zwanenburg - QT misses a person like you; Barbara Witek, Sander Dorenbos, Gilles Buchs, Gabriele Bulgarini, Michael Reimer, Reinier Heeres, Maria Barkelid, Nika Akopian - good luck in the dark room; Lucio Robledo, Hannes Bernien, Wolfgang Pfaff - good luck in the dark room with diamonds; Pol Forn-Diaz - good luck in US; Thomas Picot - you are the funniest frenchman I know, good luck in Belgium; Amelia Barreiro Megino - I wish you to get used to the Dutch weather, good luck with your research; Stijn Goossens - you are really nice guy, I wish you some cool graphene QPCs; Diego Riste - you would be a perfect person to couple diamonds with superconducting qubits and Edward Laird - good luck with bending nanotubes and making qubits. I wish all QT members good luck with their projects, future careers and in life outside the lab.

Sometimes, measurements are not easy to understand. It is good to have smart people close by to ask for an explanation. I would like to thank Jeroen Danon and Yuli Nazarov for many nice discussions. They were essential for understanding spin-orbit interaction in our nanowires. Also, I would like to thank Slava Dobrovitski from Ames Laboratory for very insightful qubit discussions. Ciprian Padurariu, good luck with your PhD; the trip to Japan with you, Michael and Han was really amusing experience.

Although, I was lucky to have a captivating project, not all of my time was spent at work. In these moments, being far from home is not always easy. I was truly lucky to be a part of the Serbian community, which added so much quality to my life and made me feel almost as nice as at home. I would like to thank Aleksandar Borisavljević, Veronika Pišorn, Jasmina Omić, Darko Simonović,



Biljana Kaitović, Milena Jovanović, Marko Petrov, Mihailo Obućina, Ivan Lazić, Miloš Vulović, Jovana Ripić, Vladimir Milovanović, Vladimir Jovanović, Ivan Josifović, Dalibor Čvorić, Nemanja Filipović, Stevan and Maja Rudinac and Miloš and Jelena Popadić for many, many joyful moments and nice conversations. In particular, Dubravka Arandjelović and Marko Mihailović - thank you for constantly caring and always organizing fun activities.

Han and Marko - thank you for being my *paranimfen* and helping me during my defense. Also, wearing a penguin suit is much more fun when you have company.

I would also like to mention certain people in Serbia without whom I would probably never have become a member of QT in the first place. I would like to thank my master project supervisor Zoran Radović, who helped me take my first steps in physics and Ivan Bozović from Brookhaven National Laboratory for drawing my attention to the QT. I want to thank my friends from Serbia, not only for being such good friends, but also for inspiring me in so many different ways over the years: Stefan Salom, Teo Šarkić, Saša Lazović, Dejan Grabovičkić, Pedja Jovanović, Dragan Radisavljević, Vojislav Gajić, Ivana Božić, Marina Marinković, Gordana Olbina and Viktor Laza. In particular, I want to thank my cousin Borislav Novakov for teaching me important lessons about faith and persistence. Finally, I would like to thank my family and especially my parents for love and support.

*Stevan Nadj-Perge  
Delft, November 2010*

# CONTENTS

<b>1</b>	<b>Introduction</b>	<b>1</b>
1.1	Nanotechnology . . . . .	1
1.2	Semiconductor nanowires . . . . .	2
1.3	Computing with electron spin . . . . .	3
1.4	Outline of this thesis . . . . .	4
	References . . . . .	5
<b>2</b>	<b>Single spins in InAs nanowire quantum dots</b>	<b>9</b>
2.1	Quantum dots . . . . .	9
2.1.1	Single quantum dots . . . . .	10
2.1.2	Double quantum dots . . . . .	12
2.1.3	Pauli spin blockade . . . . .	13
2.2	Electron spin as a qubit . . . . .	16
2.2.1	Types of spin resonance . . . . .	17
2.2.2	Relaxation and decoherence . . . . .	18
2.3	Spin-orbit interaction . . . . .	23
2.3.1	Spin-orbit interaction in bulk wurtzite and zincblende crystals . . . . .	23
2.3.2	Spin-orbit interaction in wurtzite nanowires . . . . .	27
2.3.3	Spin-orbit eigenstates in single quantum dots . . . . .	28
2.3.4	Spin-orbit eigenstates and interdot tunnel coupling in double quantum dots . . . . .	30
2.4	Hyperfine interaction . . . . .	32
2.4.1	Electron spin dynamics in the nuclear field . . . . .	34
2.4.2	Dynamics of the nuclear field . . . . .	35
2.4.3	Hyperfine and spin-orbit effects in the spin blockade regime	39
	References . . . . .	41

<b>3</b>	<b>Device fabrication and measurement setup</b>	<b>49</b>
3.1	Nanowire growth . . . . .	50
3.2	Device fabrication . . . . .	52
3.2.1	Nanowire contacts . . . . .	53
3.2.2	Gates . . . . .	54
3.2.3	Gate leakage . . . . .	56
3.3	Measurement setup . . . . .	59
3.4	High-frequency signals . . . . .	59
	References . . . . .	61
<b>4</b>	<b>Anisotropic <math>g</math>-factor in a single electron nanowire quantum dot</b>	<b>63</b>
4.1	Introduction . . . . .	64
4.2	Few-electron quantum dot . . . . .	65
4.3	Zeeman splitting . . . . .	67
4.4	$g$ -factor anisotropy . . . . .	68
4.5	Additional information . . . . .	71
	References . . . . .	73
<b>5</b>	<b>Disentangling the effects of spin-orbit and hyperfine interactions on spin blockade</b>	<b>77</b>
5.1	Introduction . . . . .	78
5.2	Spin blockade . . . . .	78
5.3	Suppression of spin blockade . . . . .	79
5.4	Comparison with a transport model . . . . .	83
	References . . . . .	86
<b>6</b>	<b>Spin blockade anisotropy in InAs nanowire double quantum dots</b>	<b>91</b>
6.1	Introduction . . . . .	92
6.2	Spin blockade anisotropy . . . . .	94
6.3	Weak coupling . . . . .	97
	References . . . . .	99
<b>7</b>	<b>Spin-orbit qubit in a semiconductor nanowire</b>	<b>101</b>
7.1	Introduction . . . . .	102
7.2	EDSR detection . . . . .	102

7.3	Coherent oscillations . . . . .	105
7.4	Free evolution and dynamical decoupling . . . . .	107
7.5	Supplementary Information . . . . .	110
7.5.1	Additional methods . . . . .	110
7.5.2	Establishing the EDSR mechanism . . . . .	111
7.5.3	Lower limit measurement of the relaxation time . . . . .	115
7.5.4	Independent control of spin-orbit qubits in two quantum dots . . . . .	116
7.5.5	Fidelity estimates . . . . .	117
7.5.6	Possible decoherence mechanisms . . . . .	118
	References . . . . .	120
<b>8</b>	<b>Conclusions and future directions</b>	<b>125</b>
8.1	Current status . . . . .	125
8.2	Short-term goals . . . . .	126
8.2.1	Realization of a two-qubit gate . . . . .	127
8.2.2	Single-shot readout and measurement of the relaxation time . . . . .	127
8.2.3	Control over the nuclear spin bath . . . . .	128
8.2.4	Spin-orbit qubits in InSb nanowires . . . . .	128
8.3	Qubits in nanowires - Outlook . . . . .	129
	References . . . . .	130
	<b>Summary</b>	<b>135</b>
	<b>Samenvatting</b>	<b>139</b>
	<b>Curriculum Vitae</b>	<b>143</b>
	<b>List of Publications</b>	<b>145</b>



# 1

## INTRODUCTION

### 1.1 NANOTECHNOLOGY

*'There's Plenty of Room at the Bottom'* is the title of the famous lecture given by Nobel laureate Richard Feynman in 1959, discussing the idea of ultimate miniaturization. In the lecture, Feynman proposes various ideas to make nanoscale machines which in the end would enable manipulation of individual atoms. By arranging single atoms and combining them in a controllable way, one would synthesize complex materials and even do chemistry by simply placing atoms at the appropriate positions. Feynman was one of the first to set the goals and identify problems of the field 'nanotechnology'. However, the actual word 'nanotechnology' has been defined fifteen years later by Japanese professor Norio Taniguchi: "'Nano-technology' mainly consists of the processing of, separation, consolidation, and deformation of materials by one atom or by one molecule." [1, 2].

Nanotechnology has had huge impact on science and society in general. For a physicist fascinated by quantum mechanics, nanotechnology is particularly interesting since it provides perfect playground for studying various interesting phenomena. Fundamental problems of quantum mechanics, such as entanglement and decoherence, can be studied with devices created using nanotechnology. These problems which could have previously only been studied

theoretically are now finally within the reach of experiments.

## 1.2 SEMICONDUCTOR NANOWIRES

Semiconductor nanowires are one of the best examples of objects created using nanotechnology. In a carefully designed process, atoms from a vapor are assembled into a solid, quasi-1D object. Many of the nanowire parameters can be controlled during growth. The diameter of the nanowires is mainly determined by the size of the catalyst particle which initializes the growth. Length is set by the growth time. By introducing different vapor gases, one can also engineer the composition of the nanowire. This unique composition versatility is illustrated in Fig. 1.1. Nanowire consisting of alternating sections of gallium phosphide (GaP) and gallium arsenide (GaAs) is shown in Fig 1.1a. The interface between the different materials can be atomically sharp without dislocations. By changing the growth temperature, even crystal phase can be controlled. Figure 1.1b shows sections of zincblende and wurtzite crystal phases of an indium arsenide (InAs) nanowire. Finally, Figs. 1.1c and 1.1d show that growth of nanowires with shell structure is also possible.

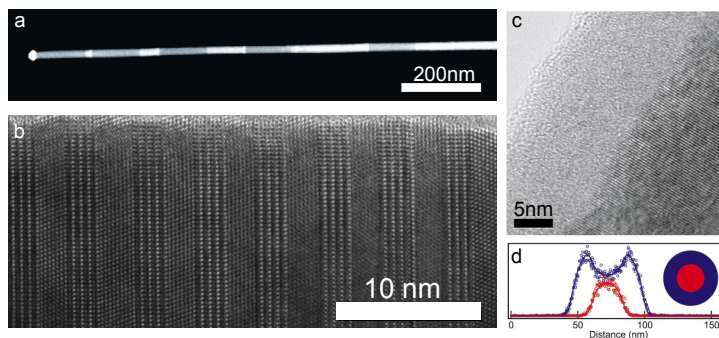


**Figure 1.1:** A few examples illustrating the high degree of freedom in nanowire growth. (a) Transmission electron microscopy (TEM) image of a nanowires with different segments of GaP and GaAs. Figure adapted from [3]. (b) Different segments of InAs nanowires with zinc-blende and wurtzite crystal structures. Figure adapted from [4]. (c) A Si nanowire with a Ge shell. Figure adapted from [5]. (d) Cross-sectional elemental mapping of the Si/Ge core shell nanowire obtained by a scanning transmission electron microscope.

It is not surprising that semiconductor nanowires have potential for applications in various fields. Many proofs of concept have been demonstrated

including field effect transistors [6], solar cells [7], light emitting diodes [8], lasers [9], biochemical sensors [10] and nanowire-based Josephson junctions [11].

## 1.3 COMPUTING WITH ELECTRON SPIN

Computers and information processing have become an important part of our every day life. Every year, computers become faster and faster and the size of transistors is getting smaller and smaller, both following Moore's law. However, the basic principle governing the computing process is equivalent of the abacus machine which dates to 2700BC. The principles of computing have not changed in the last 4000 years, following laws of classical physics. The important question one may ask is, what happens to a computing machine implemented on the atom scale where classical physics is not applicable? Perhaps, an even more important question is whether quantum mechanics allows the creation of a computing machine which can potentially outperform classical computer?

The answer to the latter question is "yes", in principle it is possible to build a *quantum computer* which operates according to the rules of quantum mechanics and outperforms a classical computer. The main advantage of a quantum computer comes from *quantum parallelism*. In simple words, quantum parallelism allows quantum computers to evaluate a given function for many different input values simultaneously [12]. This fundamental property of a quantum computer can be used to exponentially increase the speed of computing for some problems, such as factoring integers [13] or simulating a quantum system [14].

Although basic theoretical principles related to quantum computing are well understood, how to actually build such a computer remains unknown. Any quantum two-level system can, in principle, be used as a quantum bit (qubit), but in order to build a scalable quantum computer, a number of additional features are required [15]. Various two-level systems including trapped ions [16], nuclear spins [17], lattice defects in diamonds [18] and superconducting circuits [19] have been proposed as qubits. Typically, microscopic systems such as atoms or ions have good coherence properties, but are not easily scalable. On the other hand, larger systems like solid-state devices can be engineered and thus potentially scaled more easily, but often have short coherence timea.



A promising possibility which would allow to combine flexibility of the solid-state devices with long coherence of the microscopic objects, is to encode bit information (logical 0 and 1) in the spin states of an electron trapped in a quantum dot. This was first proposed by Loss and DiVincenzo [20]. The electron itself is a microscopic object, and its spin should be well protected from environmental noise. Thus, one can expect relatively long coherence times. A quantum dot, small box in which an electron is trapped, is a solid-state object. Many different aspects of a quantum dot, for example shape and material composition, can be fully engineered. Coupling between two different spins, which is important for quantum computation, can be also easily engineered or tuned *in situ*. The Loss and DiVincenzo proposal led to a huge experimental effort to implement basic building blocks of such spin-based quantum processor.

The main motivation for this thesis was to realize parts of the Loss and DiVincenzo proposal using electrons trapped in quantum dots inside an InAs nanowire. The reason for using InAs is the strong spin-orbit coupling in this material, which facilitates fast electrical control over the qubits. The main reason to use nanowires is the possibility of combining different materials to allow additional functionalities which may be important for future experiments. Integrating electrical qubit manipulation studied in this theses with an optical interface [21] for long-distance quantum communication is one interesting prospect.

## 1.4 OUTLINE OF THIS THESIS

The content of this thesis is as follows:

**Chapter 2** gives a brief introduction of the theoretical concepts related to the experiments presented in later chapters.

**Chapter 3** briefly outlines experimental techniques used in this thesis.

**Chapter 4** presents measurements of the Zeeman splitting of single electron trapped in a quantum dot. By changing magnetic field directions anisotropy of the  $g$ -factor is studied.

**Chapter 5** discusses the two-electron double quantum dots. The focus is spin blockade which is a commonly used tool for readout of spin states. In this chapter effects of the spin-orbit and hyperfine interactions on spin blockade

are carefully characterized.

**Chapter 6** discusses further spin blockade. More specifically in this chapter anisotropy of spin-blockade caused by the strong spin-orbit interaction is explored.

**Chapter 7** presents results on coherent manipulation of spin-orbit eigenstates with electric fields.

Finally, the last **chapter 8** includes concluding remarks and possible future directions.

## REFERENCES

- [1] N. Taniguchi, "*On the Basic Concept of 'Nano-Technology'* ", Proc. Intl. Conf. Prod. Eng. Tokyo, Part II, Japan Society of Precision Engineering (1974).
- [2] A. Sandhu, *Who invented nano?*, Nature Nanotechnology **1**, 87 (2006).
- [3] M. A. Verheijen, G. Immink, T. de Smet, M. T. Borgström, and E. P. A. M. Bakkers, *Growth Kinetics of Heterostructured GaP-GaAs Nanowires*, Journal of the American Chemical Society **128**, 1353 (2006).
- [4] K. A. Dick, C. Thelander, L. Samuelson, and P. Caroff, *Crystal Phase Engineering in Single InAs Nanowires*, Nano Letters **10**, 3494 (2010).
- [5] D. W. L. J. Lauhon, M. S. Gudiksen and C. M. Lieber, *Epitaxial core-shell and core-multishell nanowire heterostructures*, Nature **420**, 57 (2002).
- [6] Y. Li, F. Qian, J. Xiang, and C. M. Lieber, *Nanowire electronic and optoelectronic devices*, Materials Today **9**, 18 (2006).
- [7] B. Tian, X. Zheng, T. J. Kempa, Y. Fang, N. Yu, G. Yu, J. Huang, and C. M. Lieber, *Coaxial silicon nanowires as solar cells and nanoelectronic power sources*, Nature **449**, 885 (2007).
- [8] E. D. Minot, F. Kelkensberg, M. van Kouwen, J. A. van Dam, L. P. Kouwenhoven, V. Zwiller, M. T. Borgström, O. Wunnicke, M. A. Verheijen, and E. P. A. M. Bakkers, *Single Quantum Dot Nanowire LEDs*, Nano Lett. **7**, 367 (2007).

- [9] M. H. Huang, S. Mao, H. Feick, H. Yan, Y. Wu, H. Kind, E. Weber, R. Russo, and P. Yang, *Room-Temperature Ultraviolet Nanowire Nanolasers*, *Science* **292**, 1897 (2001).
- [10] Y. Cui, Q. Wei, H. Park, and C. M. Lieber, *Nanowire Nanosensors for Highly Sensitive and Selective Detection of Biological and Chemical Species*, *Science* **293**, 1289 (2001).
- [11] J. A. van Dam, Y. V. Nazarov, E. P. A. M. Bakkers, S. De Franceschi, and L. P. Kouwenhoven, *Supercurrent reversal in quantum dots*, *Nature* **442**, 667 (2006).
- [12] M. Nielsen and I. Chuang, *Quantum computation and information* (Cambridge University Press, Cambridge, UK, 2000).
- [13] P. W. Shor, *Algorithms for quantum computation: discrete logarithms and factoring*, Proceedings of 35th Annual Symposium on Foundations of Computer Science, IEEE Press pp. 124–134 (1994).
- [14] S. Lloyd, *Universal Quantum Simulators*, *Science* **273**, 1073 (1996).
- [15] D. DiVincenzo, *The physical implementation of quantum computation*, *Fortschr. Phys.* **48**, 771 (2000).
- [16] D. Leibfried, R. Blatt, C. Monroe, and D. Wineland, *Quantum dynamics of single trapped ions*, *Rev. Mod. Phys.* **75**, 281 (2003).
- [17] Lieven M. K. Vandersypen, Matthias Steffen, Gregory Breyta, Costantino S. Yannoni, Mark H. Sherwood and Isaac L. Chuang, *Experimental realization of Shor's quantum factoring algorithm using nuclear magnetic resonance*, *Nature* **414**, 883 (2001).
- [18] F. Jelezko, T. Gaebel, I. Popa, A. Gruber, and J. Wrachtrup, *Observation of coherent oscillations in a single electron spin*, *Phys. Rev. Lett.* **92**, 076401 (2004).
- [19] J. Mooij, T. Orlando, L. Levitov, L. Tian, C. van der Wal, and S. Lloyd, *Josephson Persistent-Current Qubit*, *Science* **285**, 1036 (1999).
- [20] D. Loss and D. P. DiVincenzo, *Quantum computation with quantum dots*, *Phys. Rev. A* **57**, 120 (1998).

- [21] M. H. M. van Weert, N. Akopian, U. Perinetti, M. P. van Kouwen, R. E. Algra, M. A. Verheijen, E. P. A. M. Bakkers, L. P. Kouwenhoven, and V. Zwiller, *Selective Excitation and Detection of Spin States in a Single Nanowire Quantum Dot*, *Nano Letters* **9**, 1989 (2009).



# 2

## SINGLE SPINS IN INAS NANOWIRE QUANTUM DOTS

We start this chapter with an introduction of the basic properties of single and double quantum dots. These quantum dot configurations are used for trapping single electrons and for single spin manipulation. We introduce the concept of spin blockade configuration, which is commonly used in the detection of spin states. After that we discuss the idea of using an electron spin degree of freedom as a quantum bit (*qubit*). We explain how spin trapped in a quantum dot can be manipulated by magnetic and electric fields, and introduce a simple model of spin relaxation and decoherence. Further, we briefly discuss interactions between trapped electron spins and the environment. We give a short introduction of spin-orbit and hyperfine interactions and discuss the roles of these interactions in spin qubit decoherence and in the detection of spin states.

### 2.1 QUANTUM DOTS

A quantum dot is a small semiconductor island in which electrons can be trapped. The dot can be coupled to reservoirs and to other quantum dots via tunnel barriers which allow the tunneling of electrons on and off the dot. In

this thesis we focus on single and double quantum dots that are coupled to the two reservoirs, called source and drain, to which we can attach current and voltage probes, see Fig. 2.1. The dot is also coupled capacitively to one or more gates which allow changes in the electrostatic potential, with respect to the reservoirs. In this work we focus on quantum dots that are formed inside a semiconducting nanowire by electrostatic gates. By applying voltages on metallic gates close to the wire the quantum dot size and tunnel coupling can be controlled *in situ*. All experiments have been performed by applying a voltage across the quantum dot and measuring the resulting current. These measurements can be easily understood via the constant interaction model [1]. In this section we briefly outline the essential concepts of this model.

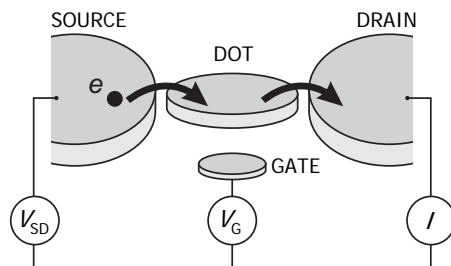


**Figure 2.1:** Schematic picture of a quantum dot. The dot is connected to the source and drain contacts via tunnel barriers. A gate is coupled capacitively to the electrons on the dot and controls their electrochemical potential. The current  $I$  flowing through the device is measured as a function of applied bias,  $V_{SD}$  and gate voltage  $V_G$ . Figure adapted from [1].

### 2.1.1 SINGLE QUANTUM DOTS

The electronic properties of a quantum dot are mainly determined by two factors. (i) Due to strong confinement in all directions, the energy spectrum is discrete. This is why quantum dots are also known as *artificial atoms* [2]. (ii) Since electrons are charged particles, they repel each other via Coulomb interaction. If we want to add an extra electron to the dot, we have to overcome the electrostatic potential set up by other electrons on the dot. Both factors can lead to a blockade of electron transport through the dot, also known as a *Coulomb blockade*, Fig. 2.2a.

By measuring the current as a function of the gate voltage  $V_g$ , we probe the electronic energy spectrum. If the voltage  $V_g$  is such that the electrochemical

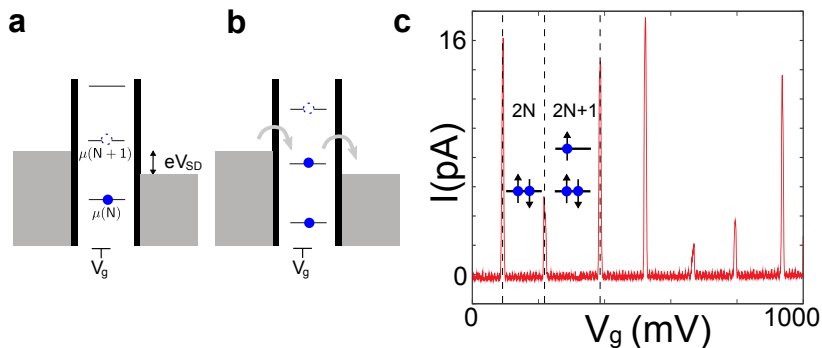


**Figure 2.2:** A single quantum dot coupled to two leads. (a,b) Energy diagrams for two different gate voltages  $V_g$ . In (a), the electrochemical potential  $\mu$  of the dot is outside the bias window  $eV_{SD}$ . Therefore, the current is blocked (Coulomb blockade). The addition energy of the quantum dot is the sum of the charging energy and the orbital level spacing:  $\mu(N+1) - \mu(N) = E_C + \Delta$ . (b) When the electrochemical potential of a dot is inside the bias window, current can flow and the blockade is lifted. (c) Current of the dot as a function of  $V_g$  when the small bias  $V_{SD} = 1$  mV is applied. The distance between the peaks alternates between being bigger and smaller depending of the number of electron on the dot. This suggests each orbital of the quantum dot can be occupied with two electrons, see inset. Data from a indium arsenide (InAs) nanowire quantum dot.

potential is within the bias window, current can flow (Fig. 2.2b). The current peaks shown in Fig. 2.2c indicate for which gate voltages the energy level lies within the bias window and contain information about the energy spectrum of the dot. More precisely, the spacing between the peaks is proportional to the addition energy of the dot.

The different addition energies observed for consecutive Coulomb peaks can be understood as follows: in order to add a new electron to the dot, we always have to overcome the Coulomb repulsion. Therefore, all current peaks are spaced at least by  $E_C$ , the electrostatic charging energy of the dot. However, if an electron is added to the new orbital, the peak spacing is larger:  $E_C + \Delta$ , where  $\Delta$  is the energy of the orbital level involved. The simple case shown in Fig. 2.2c occurs when the energy levels are only doubly degenerate due to electron spin. In this case, if the dot contains an even number  $2N$  of electrons the  $2N + 1$ st electron added to the dot has to go into the higher orbital.



### 2.1.2 DOUBLE QUANTUM DOTS

A double quantum dot consists of two quantum dots each coupled to a reservoir and to each other via a tunnel barrier, as schematically shown in Fig. 2.3a,b. The electrochemical potential in the two dots can be adjusted separately by changing the potential on the two gates,  $V_{gL}$  and  $V_{gR}$ , thereby controlling the electron number on the left and the right dot. For a fixed voltage on these gates the charge state  $(N_L, N_R)$  of the double dot is given by the equilibrium electron numbers  $N_L$  and  $N_R$ , on the left and right dot.

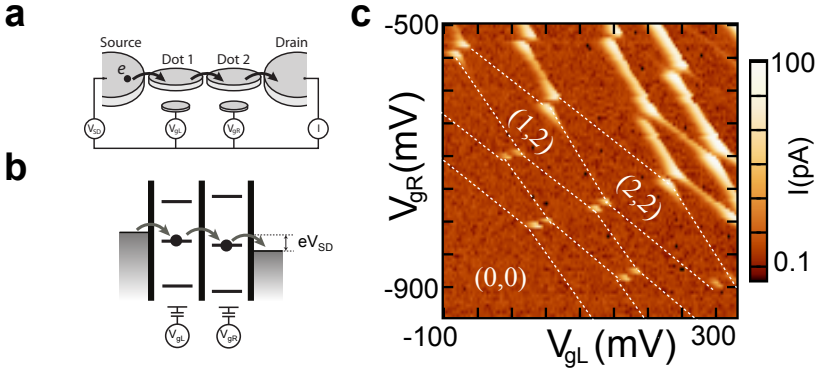


**Figure 2.3:** (a), (b) Schematics of the transport through a double quantum dot. Both dots are coupled to a reservoir and to the other dot via a tunnel barrier, allowing current through the device,  $I$ , to be measured as a function of the bias voltage  $V_{SD}$  and the gate voltages  $V_{gL}, V_{gR}$ . (b) Schematic diagrams showing the electrochemical potential on the left and right dot. A small bias  $V_{SD}$  is applied. Transport is possible if the electrochemical potentials are lined up and lie in the bias window. (c) Stability diagram of an InAs nanowire double dot. A double dot current as a function of gate voltages  $V_{gL}, V_{gR}$  for fixed bias  $V_{SD} = 1$  mV. Labels  $(N_L, N_R)$  indicate the numbers of electrons in the left and right dot. Transport occurs in the discrete points (*triple points*) at which the electrochemical levels of the two dots are aligned and within the bias windows. In the lower left region (0,0), we don't observe additional triple points. A finite cross capacitance between the left (right) dot and  $V_{gR}$  ( $V_{gL}$ ) causes the slope of the lines.

As in a single dot, current can provide information about the energy spectrum of the double quantum dot. At a small bias voltage, the current reveals at which values of the gate voltages transport occurs via the cycle  $(N_L, N_R) \rightarrow (N_L + 1, N_R) \rightarrow (N_L, N_R + 1) \rightarrow (N_L, N_R)$  through the double dot. This cycle is energetically allowed at the triple points, where the electrochemical

potentials of the three transitions  $(N_L, N_R) \rightarrow (N_L + 1, N_R), (N_L + 1, N_R) \rightarrow (N_L, N_R + 1)$  and  $(N_L, N_R + 1) \rightarrow (N_L, N_R)$  line up with the electrochemical potential of the electron reservoirs (Fig. 2.3b). The current measurement therefore allows us to map out regions in which the number of electrons on the two dots is constant. This map is called a charge stability diagram (Fig. 2.3c). At high applied bias, the triple points expand and become transport triangles in the  $(V_{gL}-V_{gR})$  plane [3] (see the next subsection). Transport occurs via the same cycle, when the electrochemical potentials of the transitions are within the bias window.

### 2.1.3 PAULI SPIN BLOCKADE

In double quantum dots, interdot charge transitions conserve spin and obey spin selection rules. This can lead to a phenomenon called *Pauli spin blockade*. The simplest case of spin blockade occurs in the regime where the occupancy of the double quantum dot can be (0,1), (1,1), or (0,2). In the (1,1) and (0,2) charge states the four possible spin states are the singlet state  $S = \uparrow\downarrow - \downarrow\uparrow$ , and the three triplets states  $T^0 = \uparrow\downarrow + \downarrow\uparrow$ ,  $T^+ = \uparrow\uparrow$ ,  $T^- = \downarrow\downarrow$ . (We omit normalization for simplicity). The ground state of the (0,2) configuration is a singlet due to the Pauli exclusion principle. The triplet (0,2) configuration involves a higher orbital state and is inaccessible for a smaller bias (in indium arsenide (InAs) nanowires the singlet-triplet splitting in a quantum dot is typically 5–7 meV). Current transport can occur via the cycle  $(0, 1) \rightarrow (1, 1) \rightarrow (0, 2) \rightarrow (0, 1)$  which involves the transition from a (1,1) to (0,2) state. However if the (1,1) triplet configuration is formed, transport is blocked. Transition from  $T_{11} \rightarrow S_{02}$  is prohibited since tunneling conserves spin.

One experimental signature of the Pauli spin blockade is the strong dependence of current on the bias direction. For forward bias, current is strongly suppressed because the current-carrying cycle is interrupted as soon as one of the triplet states is occupied (Fig. 2.4a,c). In the case of reverse bias, only singlet states can be loaded and current can always flow, *i.e.* no blockade occurs (Fig. 2.4b,d). Note that on the edges of the bias triangle in Fig. 2.4 current is high even for the forward bias. At the edges, the electrochemical potential of one of the dots is aligned with the lead. For this (1,1) configuration electron in the spin blockade can tunnel out and another electron with opposite spin can tunnel back to form the new (1,1) configuration. By this process, called *spin exchange* with the lead, electron from the triplet (1,1) state can escape

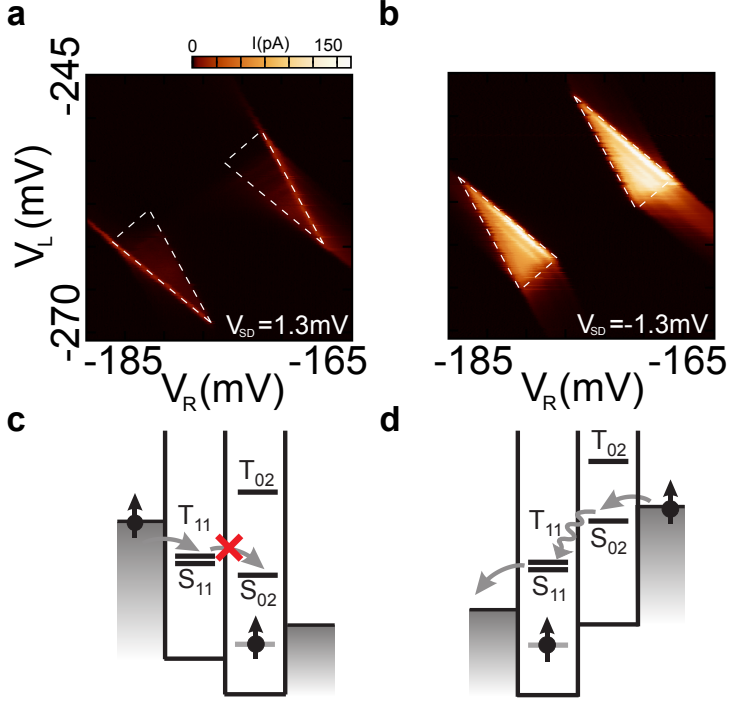


**Figure 2.4:** Transport measurements in the spin blockade regime. (a) Color-scale plot of the current through the double quantum dot under forward bias (1.3 meV), as a function of gate voltages controlling the left and right dot potentials ( $V_L$  and  $V_R$ ) at  $B_{\text{ext}} = 0$  mT. The white dotted triangles define the region where transport is energetically allowed. Transport is suppressed due to spin blockade. The two triangles correspond to two different current cycles, commonly known as the electron cycle and hole cycle. Outside the triangles, the number of electrons is fixed by Coulomb blockade. (b) Similar measurement as in (a), but for reverse bias (-1.3 meV). Current flows in the entire region in gate space where it is energetically allowed (within the white dotted triangles). (c) The schematics of spin blockade shows transport by the electron cycle,  $(1, 1) \rightarrow (0, 2) \rightarrow (0, 1) \rightarrow (1, 1)$ . The hole cycle  $(1, 2) \rightarrow (1, 1) \rightarrow (0, 2) \rightarrow (1, 2)$ , exhibits features similar to those visible in the electron cycle, although slight differences can exist. (d) When bias is reversed, singlet  $S(0, 2)$  is loaded and transport is allowed.

and another electron can enter to form a singlet  $(1, 1)$ . Spin exchange with the lead occurs on timescales determined by the tunneling rates of the incoming (or outgoing) dot barrier and it effectively lifts blockade at the edges of the bias triangle.

The second experimental signature of Pauli spin blockade is strong dependence of the leakage current on the strength and direction of the magnetic field. As we will see in the later sections, as well as in chapters 5 and 6, interactions between electron spin and the environment can induce spin-flips and lift the spin blockade, causing small leakage current to flow. Typically, the rates of spin-flip depend strongly on the magnetic field. Therefore, the magnetic field dependence of the leakage current is an even better signature for identifying spin blockade regime than measurement of current for forward and reverse bias. Spin blockade is used for reading out the spin configuration of a double dot. It is used in most of the spin manipulation experiments [4–6], as well as for the coherent control discussed in chapter 7.

Let us now discuss spin blockade and the energies of the states involved in the transport in a bit more detail. Due to the finite tunnel coupling  $t$  between the two dots, the (1,1) and (0,2) singlet states hybridize. As mentioned before, the triplet state (0,2) has much higher energy and can be ignored. The energy of the eigenstates can be calculated using the Hamiltonian, which is written in the basis of states  $S_{11}$ ,  $T_{11}^+$ ,  $T_{11}^-$ ,  $T_{11}^0$  and  $S_{02}$ . In this description the thermal energy  $kT$  can be neglected when the energy difference between the eigenstates and the Fermi energy of the left and right reservoir is much larger than  $kT$ . The Hamiltonian is given by:

$$\begin{aligned}
 H_0 = & - \delta |S_{02}\rangle \langle S_{02}| + \sqrt{2}t \left( |S_{11}\rangle \langle S_{02}| + |S_{02}\rangle \langle S_{11}| \right) \\
 & - g\mu_B B_{\text{ext}} \left( |T_{11}^+\rangle \langle T_{11}^+| - |T_{11}^-\rangle \langle T_{11}^-| \right),
 \end{aligned} \tag{2.1}$$

where  $\delta$  is level detuning (see Fig. 2.5a),  $t$  is the tunnel coupling between the  $S_{11}$  and  $S_{02}$  states, and  $B_{\text{ext}}$  is the external magnetic field in the z-direction. The eigenstates of the Hamiltonian (2.1) for a finite external field are shown in Fig. 2.5c. For  $|\delta| < t$ , the tunnel coupling  $t$  causes an anti-crossing between  $S_{11}$  and  $S_{02}$  states.

Let us now analyze transport via the  $(1, 1) \rightarrow (0, 2) \rightarrow (0, 1) \rightarrow (1, 1)$  cycle by using the energy diagram (Fig. 2.5). When  $\delta < 0$ , transport is blocked by a Coulomb blockade, because the (0,2) state  $S_{02}$  is at a higher energy than the (1,1) state  $S_{11}$ . When  $\delta \geq 0$ , two possibilities can occur.

(i) An electron that enters the left dot forms  $S_{11}$  with the electron in the right dot. It is then possible for the left electron to move to the right dot because the right dot singlet state  $S_{02}$  is energetically accessible. Transitions

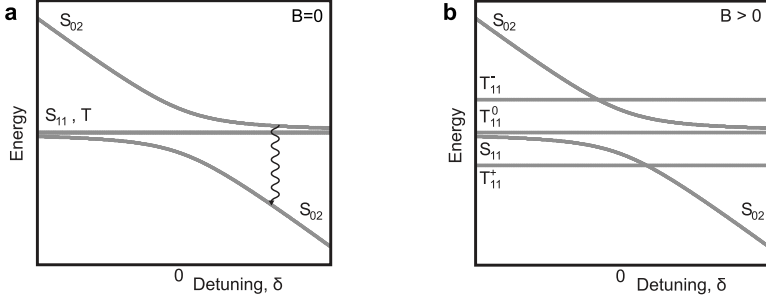


**Figure 2.5:** Energy levels for two-electron states in a double quantum dot. The tunnel coupling between the two dots leads to an anti-crossing between singlet energy levels. In the case of zero magnetic field as shown in (a), the (1,1) states are degenerate at large detuning. (b) In the case of a finite magnetic field, two triplets  $T_{11}^{\pm}$  shift in energy  $E_Z = \pm g\mu_B B$ .

from  $S_{02}$  to  $S_{11}$  are governed either by coherent coupling between the states or by inelastic relaxation (Fig. 2.5a). From  $S_{02}$ , one electron tunnels from the right dot to the right lead and another electron can tunnel into the left dot.

(ii) An electron entering the left dot forms a triplet state  $T_{11}$  with the electron in the right dot. In that case, the left electron cannot move to the right dot since tunneling conserves spin. Therefore, current is blocked as soon as any of the (1,1) triplet states is formed (see schematic at Fig. 2.4c).

## 2.2 ELECTRON SPIN AS A QUBIT

In 1998, Loss and DiVincenzo proposed the use of electron spin trapped in a quantum dot as a quantum bit [7]. Logical  $|0\rangle$  and  $|1\rangle$  states are encoded in spin states  $|\uparrow\rangle$  and  $|\downarrow\rangle$ . It was believed that environmental fluctuations only couple to the charge of electrons in a quantum dot and that a spin qubit would be well isolated from the environment. This proposal triggered large theoretical and experimental efforts in realizing a spin based quantum processor. Readout of spin states is possible in finite magnetic field. In an external magnetic field, spin up and spin down states are split by a Zeeman energy,  $E_z$ . Using this splitting it is possible to initialize and read out the spin qubit state [8, 9]. The complete set of requirements for quantum computation can also be realized. Single spin rotations can be achieved by applying a.c. magnetic or electric fields [5, 6]. Two qubit operation which entangles the two nearby spins can also be

realized. Such a gate can be realized, for example, by controlling exchange interaction [4]. Typically  $\sqrt{\text{SWAP}}$  is used as universal entangling two-qubit gate. Applied twice this gate swaps the spin states in the two neighboring quantum dots.

Similarly to the Loss and DiVincenzo's proposal, spin based quantum processing could be also achieved in a semiconductor nanowire. As will be shown in the following sections properties of electron spin depend strongly on the semiconductor environment *i.e.* on the host semiconductor. An advantage of using nanowire comes from the fact that the material composition of nanowires can be customized. In principle, the advantages of different materials can be utilized into a single nanowire. For example semiconductors with strong spin-orbit coupling, such as InAs, allow faster electrical spin manipulation. Semiconductors from group IV of the periodic table, such as silicon, have isotopes with no nuclear spin. It is believed that spin coherence time in these materials is very long.

### 2.2.1 TYPES OF SPIN RESONANCE

The most standard technique for driving transitions between Zeeman split levels is electron spin resonance (ESR) [10]. In ESR a rotating magnetic field  $B_1$  is applied perpendicular to the static external magnetic field  $B_{ext}$ . The rotating field rotates on resonance with the spin precession frequency:  $f_{ac} = g\mu_B B_{ext}/h$  ( $\mu_B$  is the Bohr magneton,  $g$  is the electron spin  $g$ -factor and  $f_{ac}$  is the excitation frequency at which  $B_1$  evolves). Fig. 2.6 shows the trajectory of the spin during ESR, both in the lab and the rotating frame. ESR is usually induced using oscillating magnetic field  $B_{ac}$  since is easier to generate than rotating magnetic field. Oscillating field has a similar effect since it can be decomposed into two counter rotating components with the amplitudes  $B_1 = B_{ac}/2$ . One component rotates with the spin and results in ESR, whereas the other rotates in the opposite way, being far off-resonant (assuming that  $B_{ext} \gg B_1$ ) and therefore having a negligible effect on spin rotation.

Spin rotation can be also achieved with electric dipole spin resonance (EDSR) [6, 11, 12]. During the EDSR a.c. electric fields on resonance are applied. The spin does not couple directly to the electric fields. However, coupling can be facilitated either by spin-orbit coupling or position-dependent magnetic field. It should be noted that, due to spin-orbit coupling, spin rotates as electron moves inside semiconductor. This effect was used for measuring

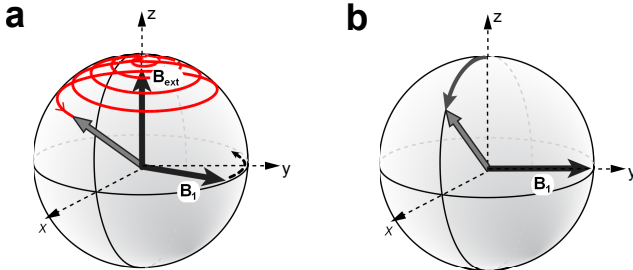


**Figure 2.6:** Spin trajectory during resonance. (a) In the laboratory reference frame spin spirals (red) over the surface of the Bloch sphere. (b) In the rotating frame which rotates with the Larmor frequency  $f_{ac}$  around the z-axis spin rotates around  $y$  (direction of magnetic field  $B_1$ ). When the resonance condition is not exactly fulfilled an offset field along the  $z$ -axis will be present.

ballistic spin resonance driven by free motion of electrons inside of narrow channel [13] or to rotate spins in the absence of external magnetic fields in strained semiconductors [14]. The spin-orbit mediated EDSR in quantum dots is further discussed in chapter 7, here we briefly discuss what happens in the case of electron placed in position-dependent magnetic field.

Due to a.c. electric fields the electron oscillates back and forth. At each point in time the electron is at the slightly different position, therefore experiencing different magnetic field. In the rest frame of the electron, the magnetic field oscillates. This oscillating magnetic field then induces a spin rotation, as in the case of ESR. A position dependent magnetic field can be achieved by, for example, fabricating a micromagnet [12, 15]. Another possibility is to use gradient in a magnetic field produced by polarized nuclear magnetic moments in the host semiconductor [11].

## 2.2.2 RELAXATION AND DECOHERENCE

Electron spin interacts with the environment through spin-orbit interaction and the hyperfine interaction with the host nuclei. These interactions can erase information stored in electron spin. We can distinguish two distinct processes which can erase spin information: *dephasing* and *relaxation*. In order to explain these two processes, let us start with the general spin state

which, up to the global phase, can be written as

$$|\Psi\rangle = \cos(\theta/2)|\downarrow\rangle + \sin(\theta/2)e^{i\phi}|\uparrow\rangle. \quad (2.2)$$

The two angles,  $\theta$  and  $\phi$ , define a point on the Bloch sphere whose poles correspond to the spin's excited  $|\downarrow\rangle$  and ground  $|\uparrow\rangle$  states, as shown in Fig. 2.7a. To represent states for which we only have partial information, called mixed states, points inside the Bloch sphere are used [16]. The distance from the center of the sphere, in this case, reflects the available information about the spin state. The center of the sphere, for example, corresponds to a fifty-fifty random mixture of  $|\uparrow\rangle$  and  $|\downarrow\rangle$  state. Pure superposition states in Eq. 2.2 correspond to a certain point *on* the sphere.

Dephasing corresponds to the loss of information stored in the phase  $\phi$  (Fig. 2.7b). For a completely dephased state, spin can be anywhere on the circle defined by  $\theta = \text{const}$ . The dephased state is then a projection of the initial spin onto the  $z$  axis of the Bloch sphere. Importantly, energy is conserved during dephasing. On the other hand, relaxation occurs when energy is dissipated into environment. After some time, spin relaxes from any prepared state to the ground state. During relaxation, information stored in the angle  $\theta$  disappears (Fig. 2.7c).

Relaxation can also be viewed as a decay of the initial longitudinal polarization  $\langle\hat{\sigma}_z\rangle$  to its equilibrium state ( $\hat{\sigma}_{x,y,z}$  are the Pauli matrices). The time scale of the relaxation decay is typically referred to as  $T_1$ . The term *decoherence* then refers to the decay of an initial transverse polarization  $\langle\hat{\sigma}_{x,y}\rangle$  and is associated with a timescale  $T_2$ . Decay of the transverse polarization can result from pure dephasing, when the information stored in the phase is lost. It is important to note that relaxation also contributes to the decay of a transverse polarization. It can be shown that  $1/T_2 = 1/(2T_1) + 1/T_\phi$ , where  $T_\phi$  is the timescale of pure dephasing [17].

To understand the processes leading to relaxation and dephasing, let us now briefly discuss a simple model which describes the environment coupling to spin [18, 19]:

$$H = E_Z\hat{\sigma}_z + \frac{\hbar}{2}[\delta\omega_z(t)\hat{\sigma}_z + \delta\omega_x(t)\hat{\sigma}_x + \delta\omega_y(t)\hat{\sigma}_y]. \quad (2.3)$$

Here  $E_Z$  is the energy splitting between the ground and excited spin states and  $\hbar\delta\omega_{x,y,z}(t)$  are fluctuations in the  $x, y, z$ -direction that are coupled to spin.



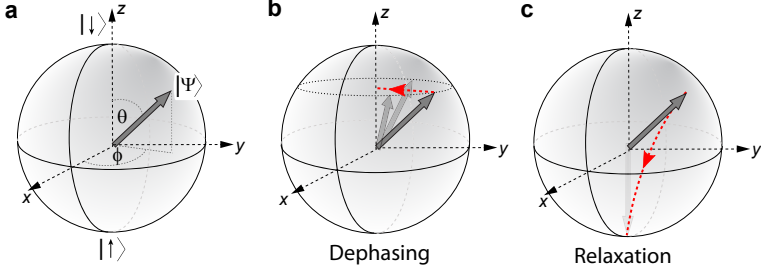


**Figure 2.7:** (a) Bloch sphere representation of the qubit state (eq. 2.2). (b) Dephasing corresponds to a loss of information of phase  $\phi$ . Energy stored in spin is conserved during dephasing. Uncertainty of the spin state due dephasing is described by differently shaded arrows on the sphere. Red dashed line with an arrow represents the evolution of the state in the Bloch sphere. After complete dephasing, final state is the projection of the initial state onto the  $z$ -axis. (c) Relaxation corresponds to the process in which energy is not conserved. Therefore information about the angle  $\theta$  is erased. Information stored in the phase  $\phi$  can also be randomized. Red dashed line with an arrow shows approximate evolution of the initial state inside the Bloch sphere.

A convenient way to characterize fluctuations is to consider the noise spectral density  $S_i(\omega) = \frac{1}{2\pi} \int_{-\infty}^{\infty} e^{i\omega\tau} C_i(\tau) d\tau$ , where  $C_i(t-t') = \langle \delta\omega_i(t) \delta\omega_i(t') \rangle$  is the autocorrelation function of  $\delta\omega_i(t)$  ( $i = x, y, z$ ). Note that the model applies for any qubit realization, not only spin.

Relaxation of spin is induced via the  $x, y$  components of  $\delta\omega_i$ , since these two terms couple the spin excited and ground states. Due to energy conservation in the combined system of the spin and its environment, only the  $\pm\omega_z$  frequency components of the power spectral density contribute to this process. This gives  $1/T_1 \propto S_x(\omega_z) + S_y(\omega_z)$ .

The longitudinal fluctuations  $\delta\omega_z$  lead to dephasing. Spin in a superposition state undergoes a Larmor precession in the  $x - y$  plane of the Bloch sphere. The Larmor precession frequency is changed by the fluctuations  $\delta\omega_z$  resulting in an extra unknown phase  $\Delta\phi = \int_0^\tau \delta\omega_z(t') dt'$  accumulated during time  $\tau$ . In contrast with relaxation where only one frequency component of the noise spectrum contributes, a wide range of frequency components of  $S_z(\omega)$  contribute to the loss of phase coherence.

The decay of the average transverse polarization is measured using the Ramsey sequence illustrated in Fig.2.8. For this discussion, let us use the rotating frame. The sequence starts with spin initialized in one of the eigen-

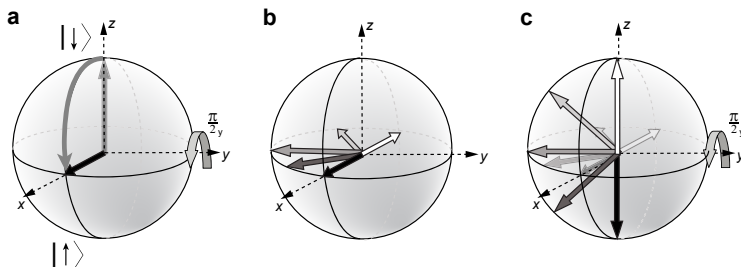


**Figure 2.8:** A Ramsey sequence seen from the rotating frame. (a) First,  $\pi/2$  pulse rotates spin in  $x - y$  plane. (b) Free evolution during time  $\tau$ . (c) a final  $\pi/2$  pulse. The arrows of different shade represent the spin state after the free evolution for the different values of  $\delta\omega_z$ . Figure adapted from [20].

states *e.g.*  $|\downarrow\rangle$ . First we apply a  $\pi/2$  pulse around the  $y$ -axis and align spin with the  $x$ -axis of the Bloch sphere. Spin then evolves freely during a time  $\tau$ . After the free evolution another  $\pi/2$  pulse around the  $y$ -axis is applied. If no dephasing has taken place during  $\tau$  we will find spin in the state  $|\uparrow\rangle$  after the sequence. If spin has rotated in the  $x$ - $y$  plane by  $\pi$  we will find the spin in the state  $|\downarrow\rangle$  after the sequence. The average decay of the transverse polarization due to information loss of the phase  $\phi$  is therefore mapped onto the decay of the longitudinal polarization using  $\pi/2$ -pulses.

The form and characteristic of the decay depend on the noise distribution of  $\delta\omega_z$ . For the case of Gaussian noise the average transverse polarization decays as [19]:

$$\langle \hat{\sigma}_x \rangle(\tau) \propto \exp\left(-\frac{\tau^2}{2} \int_{-\infty}^{\infty} S_z(\omega) W_R(\omega\tau) d\omega\right), \quad (2.4)$$

where  $W_R$  is the spectral filter function. The filter function  $W_R$  contains information about how certain pulse sequence preserves spin coherence. In the simplest case presented here, the filter function is given by  $W_R(\omega\tau) = \sin^2(\omega\tau/2)/(\omega\tau/2)^2$ . When low frequency fluctuations of  $\delta\omega_z$  are dominant, the contribution from the low frequencies  $\omega \ll 1/\tau$  gives the following decay  $\langle \hat{\sigma}_x \rangle(\tau) \propto \exp(-(\tau/T_2^*)^2)$ , where  $(1/T_2^*)^2 = 1/2 \int_{-\infty}^{\infty} S_z(\omega) d\omega$ .

The loss of coherence that is caused by the low frequency components of  $S_z(\omega)$  is often called inhomogeneous broadening. In Nuclear Magnetic Resonance (NMR) experiments on ensembles of spins, each spin experiences a

different but static  $\delta\omega_z$ . Therefore, the coherence decay is an effect of an ensemble average over the  $\delta\omega_z$  distribution. In single qubit experiments, dephasing can still occur when coherence measurements are averaged over long times, since in that case noise is sampled over the all values of the  $\delta\omega_z$  distribution.

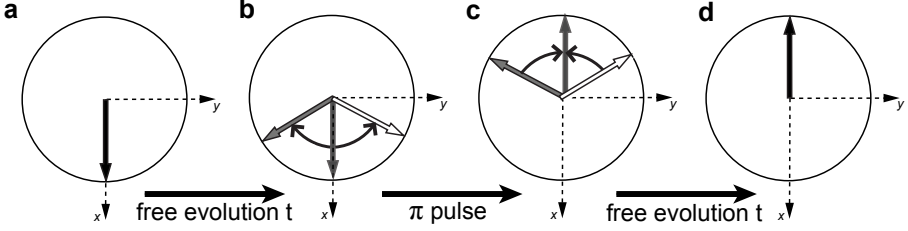


**Figure 2.9:** Spin echo sequence. First and last  $\pi/2$  pulses are omitted. Starting from spin oriented along  $x$ -axis (a), spins evolves freely for time  $t$  (b). (c) At time  $t$  refocusing  $\pi$  pulse is applied. (d) A spin is refocused after another time period  $t$  (that is at time  $2t$ ).

A Hahn echo decay sequence cancels out inhomogeneous broadening that arises from long averaging times, see Fig. 2.9. Again, a  $\pi/2$  pulse first aligns spin with the  $x$ -axis in the Bloch sphere. Then spin evolves freely during a time  $t$  after which a  $\pi$  pulse is applied. The pulse effectively interchanges  $|\uparrow\rangle$  and  $|\downarrow\rangle$  and thus leads to a refocusing of the transverse spin polarization after another time  $t$  if  $\delta\omega_z$  stayed constant during the entire evolution (see Fig.2.9). A final  $\pi/2$  pulse allows the measurement of the transverse spin polarization. The random phase acquired during an echo experiment is given by  $\Delta\phi = \int_0^t \delta\omega_z(t')dt' - \int_t^{2t} \delta\omega_z(t')dt'$ . The spin echo decay for a Gaussian noise spectral density is given by Eq. 2.4 as well, with the spectral filter function  $W_{\text{echo}} = \tan^2(\omega\tau/2)W_R(\omega\tau)$ <sup>1</sup>. The decay time from a spin-echo experiment  $T_{\text{echo}}$  can be much larger than  $T_2^*$ , especially when low-frequency components of  $S_z(\omega)$  are dominant. In the case of white noise ( $C_z(t') \propto \delta(t')$ ) the spin echo decay is exponential with the same time constant as the Ramsey decay, since the noise is uncorrelated in time.

The Hahn echo sequence can be generalized by using more  $\pi$ -pulses within the total time  $\tau$  (Carr-Purcell pulses [21]), further changing the spectral filter function to  $W_{\text{CP}} = \tan^2(\omega\tau/(N+1))W_R(\omega\tau)$ . Here  $N$  is the total number of

<sup>1</sup>Note that we use label  $t$  for the time between the pulses and  $\tau$  for the total evolution time.

In the case when the duration of the  $\pi$  pulse is negligible,  $\tau = 2t$

$\pi$  pulses. As the number of pulses is increased the decay is more and more insensitive to higher and higher frequencies. For specific shapes of the noise spectral density direct relations between Carr-Purcell coherence time  $T_{CP}(N)$ , Hahn echo time  $T_{echo}$  and  $T_2^*$  can be established [22].

## 2.3 SPIN-ORBIT INTERACTION

In atomic physics, a spin-orbit interaction comes from the interaction of electron spin with the electric field of the nucleus. An electron in an atom orbits around a positively-charged nucleus with the momentum  $p$  in the electric field  $\mathbf{E}$ . In the rest frame of the electron this motion gives rise to magnetic field  $B \propto \mathbf{p} \times \mathbf{E}$ , which interacts with electron spin. If we assume spherically symmetric potential, we can obtain a familiar dependence of the spin-orbit Hamiltonian  $H_{SO} \propto \mathbf{L} \cdot \mathbf{S}$  where  $\mathbf{L} = \mathbf{r} \times \mathbf{p}$  is the orbital angular momentum of the electron. The first order relativistic correction from the Dirac equation gives the following Hamiltonian for spin-orbit interaction:

$$H_{SO} = \frac{\hbar}{4m_0^2c^2} \boldsymbol{\sigma} \cdot (\mathbf{p} \times \mathbf{E}(\mathbf{r})). \quad (2.5)$$

Here,  $m_0$  is the mass of the free electron and  $\sigma = (\sigma_x, \sigma_y, \sigma_z)$  are the Pauli matrices, and  $\mathbf{E} = -\nabla V(\mathbf{r})$  with  $V(\mathbf{r})$  representing the electrostatic potential. It should be noted that the largest contributions to the spin-orbit coupling occur in the regions close to the atomic core, where the electric fields and electron speed are the largest. For that reason, spin-orbit interaction is larger for heavier atoms. (with large atomic numbers  $Z$ ).

### 2.3.1 SPIN-ORBIT INTERACTION IN BULK WURTZITE AND ZINCBLLENDE CRYSTALS

An electron moving through a crystal lattice of a semiconductor is influenced by the electric fields from charged atoms in the lattice. The electric fields give rise to spin-orbit coupling in the same way as for an electron orbiting the atomic nucleus. The effect of spin-orbit coupling in semiconductors is twofold: 1) it changes the energy band structure therefore changing the orbital motion of electrons in crystal lattice and 2) it affects the spin degree of freedom. Electrons in the lattice are affected by an effective internal magnetic field, which

can induce spin splitting even at zero external field. How spin-orbit coupling modifies the band structure and affects electron spins depends strongly on the symmetry of the underlying crystal structure. In this section we will discuss zincblende and wurtzite crystal structures. Although the nanowires used in this thesis are known to have wurtzite structure, it has been shown recently that InAs zincblende nanowires can also be grown [23, 24].

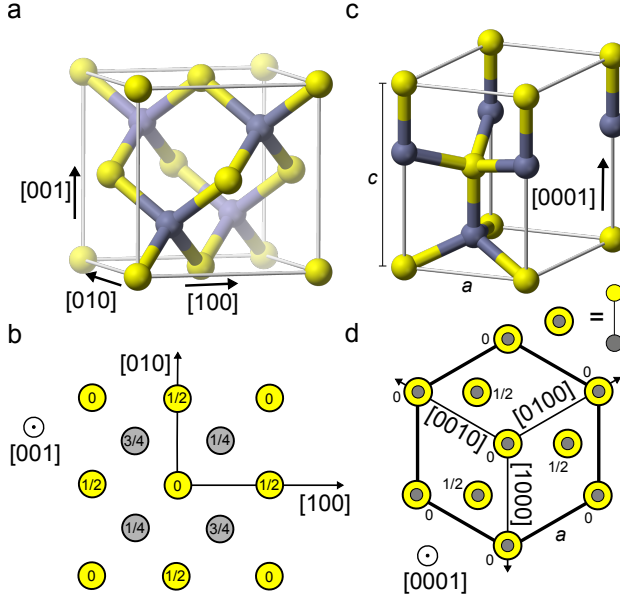


**Figure 2.10:** (a,b) zincblende crystal structure. The main crystallographic directions are labeled  $[100]$ ,  $[010]$  and  $[001]$ . In (b) the zincblende structure is shown seen from the  $[001]$  directions. The numbers give the height of the atoms in units of the lattice constant and the two colors encode the two different type of atoms. (c,d) wurtzite crystal structure. The main crystallographic direction is labeled  $[0001]$ . In (d) the wurtzite crystal structure is shown seen from the  $[0001]$  direction. The numbers give the height of the atoms in units of the lattice constant  $c$  and the two colors represent the two different type of atoms. Both crystal structures lack bulk inversion symmetry.

In a crystal with inversion symmetry, such as diamond, all electronic states are at least double degenerate. This is a consequence of time reversal (Kramers) symmetry and of the inversion symmetry. Time reversal symmetry implies  $E_{\uparrow}(k) = E_{\downarrow}(-k)$ . Here, we label the energy of the lowest conduction band

with  $E_{\uparrow,\downarrow}(k)$  and the two Kramers doublets with  $\uparrow,\downarrow$ . If the crystal also has spatial inversion symmetry then  $E_{\uparrow}(k) = E_{\uparrow}(-k)$  also holds. The two conditions combined give  $E_{\uparrow}(k) = E_{\downarrow}(k)$ , which means the bands are spin degenerate. However, crystal structures like zincblende and wurtzite (Fig. 2.10) do not have the inversion symmetry. Usually, they are referred to as crystals with bulk inversion asymmetry (BIA). In these crystal structures the second condition is not satisfied and spin splitting at zero magnetic field can occur.

The exact symmetry of the crystal structure imposes the form of the spin-orbit Hamiltonian. Let us focus on the electronic s-like states in the conduction band since this is the relevant band for electrons in InAs. The two structures of zincblende and wurtzite have a different form of spin-orbit Hamiltonian reflecting the difference in crystal structure symmetry. For the case of zincblende crystal structure, spin-orbit coupling in the lowest order can be written as [25]:

$$H_{\text{BIA}}^{\text{ZB}} = \gamma(p_x(p_y^2 - p_z^2)\sigma_x + p_y(p_z^2 - p_x^2)\sigma_y + p_z(p_x^2 - p_y^2)\sigma_z). \quad (2.6)$$

Here,  $\gamma$  is the coupling constant and x, y, z correspond to the main crystallographic directions [100], [010], [001]. For wurtzite crystals, due to a different symmetry spin-orbit Hamiltonian has a different form:

$$H_{\text{BIA}}^{\text{W}} = \lambda[\mathbf{p} \times \mathbf{c}] \cdot \boldsymbol{\sigma} + (\lambda_l(\mathbf{p} \cdot \mathbf{c})^2 + \lambda_t(\mathbf{p} \times \mathbf{c})^2)[\mathbf{p} \times \mathbf{c}] \cdot \boldsymbol{\sigma}. \quad (2.7)$$

Here  $\mathbf{c}$  is the unit vector along the [0001] axis of the wurtzite crystal. The first term is linear in  $\mathbf{p}$  while the second term describes the third order contributions.  $\lambda$ ,  $\lambda_l$  and  $\lambda_t$  are the coupling constants [26, 27]. It is important to note that for bulk zincblende structures there is no linear term in the spin-orbit Hamiltonian, while for a wurtzite structure there is such a term due to reduced symmetry. Note that in a 2D electron gas however, there are terms which are linear in  $p$ . This is due to an additional reduction of symmetry in 2D [28].

While knowing the symmetry of the crystal lattice is enough for deducing the functional form of the spin-orbit interaction, a band structure calculation is needed in order to estimate the coupling constants. The calculation starts from a Bloch wave description of the electronic states:  $\Psi(\mathbf{r}) = e^{i\mathbf{k}\mathbf{r}}u_{nk}(\mathbf{r})$ , where  $u_{nk}(r)$  is the Bloch part labeled with a  $\mathbf{k}$ -vector and a band index  $n$ . For an actual calculation, equations for the Bloch part are derived and expanded around a specific value of  $\mathbf{k}$ . This is called the  $\mathbf{k} \cdot \mathbf{p}$  method [29]. We

are interested in energy levels and interactions in the vicinity of the  $\Gamma$  point for  $\mathbf{k}=0$ . In the *extended Kane* model the topmost p-like valence band states ( $X, Y, Z$ ) and the s-like (S) and p-like ( $X', Y', Z'$ ) bands are actually taken into account for the band structure calculation (Fig. 2.11). Coupling of different bands is calculated via perturbation theory. The spin-orbit interaction modifies the coupling of different bands and for creates a so-called spin-orbit (split-off) gap, see Fig. 2.11.

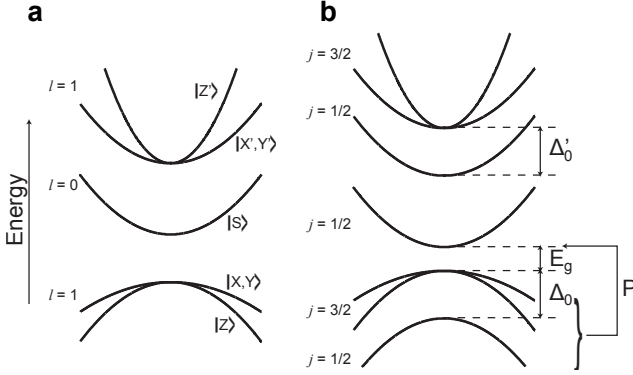


**Figure 2.11:** (a) Diagram showing the bands around the fundamental bandgap that are taken into account in the extended Kane model. Shown are the energy levels with their corresponding orbital angular momentum when spin is ignored. Note that the energies for  $|X\rangle$  ( $|X'\rangle$ ) and  $|Y\rangle$  ( $|Y'\rangle$ ) are degenerate. (b) When spin-orbit interaction is included, spin and orbital angular momentum quantum numbers are no longer well defined and we have to construct states of the total angular momentum  $\mathbf{j} = \mathbf{l} + \mathbf{s}$ . This lifts all degeneracies at finite  $k$  and produces the spin-orbit gaps  $\Delta_0$  and  $\Delta'_0$ .  $\mathcal{P} = \hbar/m_0 \langle S | p_x | X \rangle$  is the momentum matrix element that indicates the coupling of the upper valence bands to the lowest conduction band. For small bandgap materials this coupling is the most important momentum matrix element for determining the properties of the conduction band electrons. Figure adapted from [30]. Note that the extended Kane model also takes into account the coupling to higher bands.

The extended Kane model is important since it connects the parameters of the band structure (like the bandgap, the spin-orbit gap, and the transition matrix elements [30]) and quantities like the Landé  $g$ -factor and the effective mass in a semiconductor. It should be noted, however, that the parameters for bulk wurtzite InAs are not known. This is due to the fact that bulk InAs can only be produced with zincblende symmetry, and wurtzite crystal structure is only realized in nanowires. It is estimated that differences of crystal structure

modify the parameters of the band structure by roughly 10% [31]. Note that to the reduced symmetry in the bulk wurtzite structures the  $g$ -factor and the effective mass are actually anisotropic [31, 32].

### 2.3.2 SPIN-ORBIT INTERACTION IN WURTZITE NANOWIRES

Besides the bulk inversion asymmetry, which is a material property, confinement effects strongly modify spin-orbit interaction since they can further reduce symmetry. A well-known example is the Rashba Hamiltonian for electrons confined in 2D:  $H_R^{2D} \propto (-p_y\sigma_x + p_x\sigma_y)$ .

Nanowire geometry also strongly modifies the form of spin-orbit coupling. For the quantum dots defined in nanowires, we consider two extreme cases, following Refs. [27, 33]. In Fig. 2.12a, the dot confinement can be approximated as being an elongated cylinder, with the strongest confinement provided by the nanowire surface. In this limit contributions from Eq. 2.7 that are linear in momentum vanish when averaged over the transverse electron motion [27]. Besides contributions from third order terms, the spin-orbit coupling due to the structural inversion asymmetry at the radial edge of the nanowire surface becomes also important. For the case when the dot is not ideally cylindrical, when the dot is created electrostatically with gates, the spin-orbit interaction is given by [27, 33]:

$$H_{SO}^l = (\mathbf{p} \cdot \mathbf{c})(\boldsymbol{\eta} \cdot \boldsymbol{\sigma}). \quad (2.8)$$

The above Hamiltonian captures the effects of both structure and bulk inversion asymmetries [34, 35]. However, the direction and strength of the coupling vector  $\boldsymbol{\eta}$  depends on a concrete realization of the confinement (see supplementary information of [27] for more details).

In the opposite limit, in which the dot is strongly confined in the longitudinal direction (Fig. 2.12b), the spin-orbit interaction is given by [27, 33]:

$$H_{SO}^t = \alpha[\mathbf{p} \times \mathbf{c}] \cdot \boldsymbol{\sigma}. \quad (2.9)$$

The coupling parameter  $\alpha$  for this case also depends on concrete realization of confinement. This form of spin-orbit coupling corresponds to electric fields aligned with the nanowire axis. This is not surprising, taken into account the bulk Hamiltonian for the wurtzite crystal structure (Eq. 2.7). Experimentally, for the quantum dots discussed in this thesis, confinement is expected to be between these two extreme cases which makes the analysis more complicated.



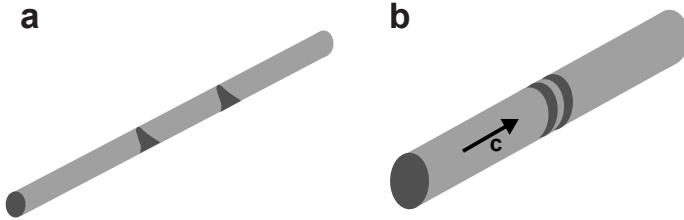


**Figure 2.12:** Schematic representation of quantum dots formed in nanowires. Dark-colored regions indicate tunnel barriers formed by a depleted nanowire region or a heterojunction. (a) The strongest confinement is provided by the nanowire surface. In this case, the spin-orbit interaction simplifies to a single vector of coupling constants. (b) Lateral confinement dominates the radial confinement. Wurtzite nanowires are grown along [0001] direction  $\mathbf{c}$  (marked with arrow), see chapter 3.

A rough estimate of the strength of spin-orbit coupling in nanowires can be obtained by measuring the spin-orbit length  $l_{SO}$ . As electron moves through the semiconductor, electron's spin is rotating due to spin-orbit coupling. The rotation speed is proportional to electron velocity, so the spin rotation angle depends only on the length. After a length of  $l_{SO}$ , the spin performs a  $\pi$  rotation [36]. In InAs nanowires  $l_{SO}$  is typically 100 – 200 nm [27, 37], which is about two orders of magnitude shorter compared to GaAs 2D electron gas. Note that the exact values of spin-orbit length depend on the electric fields in a nanostructure.

The  $g$ -factor is also modified due to confinement effects. The  $g$ -factor in nanowires is discussed further in [38] and in chapter 4 of this thesis. Due to confinement the energy gap is effectively increased by the orbital energy in a quantum dot  $E_g = E_g + \Delta$ . This modifies the resulting band structure and hence the  $g$ -factor.

### 2.3.3 SPIN-ORBIT EIGENSTATES IN SINGLE QUANTUM DOTS

Quantum dots are 0D objects. Since the electron is confined in all three directions average momentum is zero:  $\langle p_{x,y,z} \rangle = 0$ . For this reason, spin-orbit coupling does not directly couple the Zeeman split levels of a quantum dot, since  $\langle q \downarrow | H_{SO} | q \uparrow \rangle \propto \langle q | p_{x,y,z} | q \rangle \langle \downarrow | \sigma | \uparrow \rangle = 0$ , where  $q$  labels the orbitals of the quantum dot. However, states with different orbital numbers can still be coupled. The resulting states in the presence of spin-orbit interaction are admixtures of spin and orbital states. When the Zeeman splitting and spin-

orbit matrix elements are much smaller than the orbital level spacing, the eigenstates to the first order can be written as [36]:

$$\begin{aligned} |q \uparrow\rangle^{(SO)} &= |q \uparrow\rangle + \sum_{q' \neq q} \frac{\langle q' \downarrow | H_{SO} | q \uparrow \rangle}{E^q - E^{q'} - \Delta E_Z} |q' \downarrow\rangle; \\ |q \downarrow\rangle^{(SO)} &= |q \downarrow\rangle + \sum_{q' \neq q} \frac{\langle q' \uparrow | H_{SO} | q \downarrow \rangle}{E^q - E^{q'} + \Delta E_Z} |q' \uparrow\rangle. \end{aligned} \quad (2.10)$$

Labels  $q, q'$  refer to all the orbital quantum numbers, and  $\Delta E_Z$  corresponds to Zeeman splitting without spin-orbit coupling. To further simplify the last equation, let us look at the ground state spin doublet and take into account only the contributions of the first excited state:

$$|g \uparrow\rangle^{(SO)} = |g \uparrow\rangle + \frac{\langle e \downarrow | H_{SO} | g \uparrow \rangle}{E^{orb} - \Delta E_Z} |e \downarrow\rangle; \quad (2.11)$$

$$|g \downarrow\rangle^{(SO)} = |g \downarrow\rangle + \frac{\langle e \uparrow | H_{SO} | g \downarrow \rangle}{E^{orb} + \Delta E_Z} |e \uparrow\rangle. \quad (2.12)$$

Here,  $E_{orb}$  is the orbital energy of the first excited state. We see that the amount of admixture of spins increases with the strength of spin-orbit coupling, *i.e.* matrix elements of  $H_{SO}$ , and decreases for higher orbital energies. Note that the two spin-orbit modified eigenstates make Kramers doublet. Therefore, the corresponding labels  $\uparrow$  ( $\downarrow$ ) actually refer to one of the two Kramers states, not spin.

The mixing of spin and orbital degrees of freedom have several important consequences in single and double quantum dots. It mediates the coupling of spin with electric fields. If carefully controlled, electric fields can be used for controlling electron spin [6] (see also chapter 7 of this thesis). On the other hand, uncontrolled electric fields are considered to be the main source of spin relaxation. Besides electrical noise in the experimental setup, fluctuating electric fields may arise from lattice phonons. Phonons produce electrical fluctuations either by deforming the crystal lattice and locally changing the bandgap or via piezoelectric effect. Since in the spin-flip process a phonon with an energy  $E_Z$  is emitted, spin relaxation rate depends strongly on magnetic field. In general, the relaxation rate depends on (i) the phonon density of states, (ii) the coupling of the phonon to the dot, (iii) the electric field strength associated with single field and (iv) the strength of spin-orbit interaction. For

single spins in GaAs relaxation times over  $\sim 1$ s are measured in low magnetic fields [39]. Furthermore, the predicted  $1/T_1 \propto B_{ext}^5$  dependence for coupling to piezoelectric phonons [40] was observed experimentally [36]. At the moment, there is no experimental data for spin relaxation time  $T_1$  in quantum dots in InAs nanowires, although measurements presented in chapter 7 give a lower bound of  $T_1 \gg 1\mu s$  for fields  $B = 100 - 150$  mT. For these values of magnetic field relaxation time of  $T_1 \sim 1 - 10$  ms is predicted for InAs nanowires [33]. Also, magnetic field dependence of relaxation time is greatly modified by the nontrivial phonon spectrum in nanowires and it is different for the two quantum dot geometries shown in Fig. 2.12.

### 2.3.4 SPIN-ORBIT EIGENSTATES AND INTERDOT TUNNEL COUPLING IN DOUBLE QUANTUM DOTS

When electron tunnels from one dot to the other, due to spin-orbit interaction, its spin changes slightly. The simple physical picture is that during tunneling electron experiences an effective magnetic field. For a general spin-orbit Hamiltonian  $H_{SO} = \mathbf{h}(\mathbf{p}) \cdot \mathbf{S}$ , effective spin-orbit field that acts upon an electron during tunneling from the first to the second dot is given by  $\langle \Psi_1 | \mathbf{h}(\mathbf{p}) | \Psi_2 \rangle$  [41]. Here  $|\Psi_{1(2)}\rangle$  are the orbital eigenstates of an electron in the two dots. Importantly, if external magnetic field is aligned with the effective spin-orbit field, spin state will be conserved during tunneling. Another important note is that direction of the spin-orbit field depends on the details of the eigenstates in the two dots as well as on the spin-orbit Hamiltonian.

This simple physical picture explains how spin can be flipped during tunneling. Similar conclusion can be reached if we consider eigenstates of an electron in a quantum dot. As shown in the previous section, the electron eigenstates in a quantum dot are modified by the spin-orbit interaction. We can use Eq. 2.12 to estimate the wavefunction overlap between the states in the two dots with opposite 'spin' (that is with different Kramers index):

$$\langle g_1 \uparrow^{(SO)} | g_2 \downarrow^{(SO)} \rangle = \frac{\langle e_1 \downarrow | H_{SO} | g_1 \uparrow \rangle}{E_1^{orb} - \Delta E_Z} \langle e_1 | g_2 \rangle + \frac{\langle e_2 \uparrow | H_{SO} | g_1 \uparrow \rangle}{E_2^{orb} + \Delta E_Z} \langle e_2 | g_1 \rangle. \quad (2.13)$$

Here labels 1(2) correspond to first and second dot. The resulting wavefunction overlap given by Eq. 2.13 is not zero meaning that the two 'anti-parallel'

spin-orbit states are not orthogonal. Therefore, tunneling matrix element between these states is also, in general, non-zero. Coupling in Eq. 2.13 is linear in the spin-orbit strength and depends on the overlap between the ground state of dot 1(2) and excited state of dot 2(1).

In materials like InAs, in which spin-orbit length is comparable to quantum dot size, things are more complicated. The admixture of spin and orbital degrees of freedom is considerable and the spin-orbit coupling can not be treated as a small perturbation. Additionally, we are interested in the two-electron states which complicates calculations further. A phenomenological model which describes the states of the double quantum dot and includes the effects of spin-orbit coupling is developed in Ref. [42]. In the following, we will briefly explain this model.

Let us focus on the spin blockade  $(1,1) \rightarrow (0,2)$  transition. The simple picture in which triplet states  $T_{11}$  are decoupled from singlet  $S_{02}$ , discussed in section 2.1.3, is modified. The three triplet (1,1) spin-orbit eigenstates constructed from Kramers doublets of the first and the second dot, have a spin singlet component and thus may be coupled to  $S_{02}$ . Since spin-orbit coupling has to satisfy time-reversal symmetry, tunneling Hamiltonian can be written in the following form:

$$H_t = \vec{t}|\vec{T}\rangle\langle S_{02}| + t_0|S_{11}\rangle\langle S_{02}| + h.c. \quad (2.14)$$

Here  $|\vec{T}\rangle = \{|T_x\rangle, |T_y\rangle, |T_z\rangle\}$ , corresponds to the triplet basis  $|T_{x,y}\rangle = i^{3/2\pm 1/2} \{|T_{11}^-\rangle \mp |T_{11}^+\rangle\}/\sqrt{2}$  and  $|T_z\rangle = i|T_{11}^0\rangle$ . These states form an unpolarized basis along x, y and z direction. The first part of the Hamiltonian 2.14 results from spin-orbit coupling while the second corresponds to the usual singlet (1,1) to singlet (0,2) tunneling. The reason for the unusual choice of the triplet basis states is twofold:

1) The basis states are invariant with respect to time reversal symmetry. This implies that matrix elements  $t_x$ ,  $t_y$  and  $t_z$  for this choice of basis are real numbers.

2) The basis  $\{|T_x\rangle, |T_y\rangle, |T_z\rangle\}$  transforms in the same way as the real space basis  $\{\vec{e}_x, \vec{e}_y, \vec{e}_z\}$  under rotations, which is convenient for considering anisotropy effects. For example, if we rotate the coordinate system to the new basis, the corresponding coefficients  $t'_x$ ,  $t'_y$  and  $t'_z$  will change in the same way as the coordinates of any real space vector. Therefore,  $\vec{t}_{SO} = \{t_x, t_y, t_z\}$  may be considered as a vector pointing in a certain direction in space.

In general, the magnitude of coupling  $|t_{SO}| = \sqrt{t_x^2 + t_y^2 + t_z^2}$  is of the order of  $\sim (E_{SO}/E_{orb})t$  where  $E_{SO}$  is the energy scale of the matrix elements in Eq. 2.13. Since the structure of the electron wavefunction depends on the details of the confinement potential, the direction of  $\vec{t}_{SO}$  is hard to predict. However, the vector nature of the coupling  $\vec{t}_{SO}$  has a simple physical consequence: if we align magnetic field with the direction of  $\vec{t}_{SO}$  then  $T_{11}^\pm$  will not be coupled to the singlet  $S_{02}$ . This is similar to the case of  $(1, 0) \rightarrow (0, 1)$  transition considered above. Further discussion of the anisotropy of spin blockade in InAs nanowires is presented in chapter 6.

## 2.4 HYPERFINE INTERACTION

All nuclei in III-V semiconductor materials have non-zero spins, which can also interact with electron spin. The name 'hyperfine interaction', comes from atomic physics where the interaction manifests itself in the hyperfine structure of atomic spectra. The coupling between the magnetic moment of the nucleus  $\mu_N$  and the magnetic moment associated with the electron spin  $\mu_e$  is described by  $H = \frac{\mu_e \mu_N}{r^3} - \frac{3(\mu_e \mathbf{r})(\mu_N \mathbf{r})}{r^5}$  where  $\mathbf{r}$  is relative position of the nucleus and the electron. This Hamiltonian can be used to calculate the hyperfine interaction for electrons which do not overlap with the nucleus (this holds for electrons with non-zero orbital momentum such as, for example, the electrons in p- or d- orbitals), just by averaging over the electron wavefunction. However, for an electron in s-type orbital, which is the relevant case for electrons of the conduction band in InAs nanowires, there is a finite probability of finding the electron at the position of the nucleus  $\mathbf{r} = 0$ . Note that for  $\mathbf{r} = 0$  the hyperfine Hamiltonian diverges. The large electromagnetic interaction at the position of the nucleus requires a relativistic correction which dominates the coupling between electron and nuclear spins [21, 43]:

$$H_{\text{HF}} = \frac{2\mu_0}{3} g_0 \mu_B \gamma_n \hbar |\psi(0)|^2 \mathbf{I} \cdot \mathbf{S}. \quad (2.15)$$

This is called the Fermi contact hyperfine interaction [44]. Here  $g_0$  is the free-electron  $g$ -factor,  $\gamma_n$  the nuclear gyromagnetic ratio and  $|\psi(0)|^2$  is the magnitude of the electron wave function  $\psi(\mathbf{r})$  at the position of the nucleus. In contrast to an electron in an atom, an electron in a quantum dot interacts with many nuclear spins in the host material. In this case the Hamiltonian for the

	I	$\gamma_j$ (rad T <sup>-1</sup> s <sup>-1</sup> )	$A_j$ ( $\mu$ eV)	$Q_j$ (mb)
<sup>69</sup> Ga	3/2	$6.43 \times 10^7$	74	171
<sup>71</sup> Ga	3/2	$8.18 \times 10^7$	96	107
<sup>75</sup> As	3/2	$4.60 \times 10^7$	86	314
<sup>113</sup> In	9/2	$5.88 \times 10^7$	110	759
<sup>115</sup> In	9/2	$5.90 \times 10^7$	110	770

**Table 2.1:** Nuclear spin, gyromagnetic ratios, contact hyperfine coupling strengths in  $\text{In}_x\text{Ga}_{1-x}\text{As}$ , and quadrupole moments  $eQ$ , where  $e$  is electron charge, see discussion in section 2.4.2. Note that 1 mb (millibarn) =  $10^{-31}$  m<sup>2</sup>. Table adapted from [46].

Fermi contact hyperfine interaction is given by the sum over the contributions from all  $N$  nuclei:

$$H_{HF} = \frac{2\mu_0}{3} g_0 \mu_B \hbar \sum_{i=1}^N \gamma_n^i |\psi(\mathbf{r}_i)|^2 \mathbf{I}_i \cdot \mathbf{S}, \quad (2.16)$$

where  $\mathbf{I}_i$  denotes the nuclear spin at position  $\mathbf{r}_i$ . In a crystal the electron wavefunction can be written as a product of a Bloch function  $u(\mathbf{r})$ , which depends on the specifics of the crystal unit cell and is periodic with respect to the crystal lattice, and an envelope wave function  $\Psi(\mathbf{r})$ , which depends on the macroscopic confinement potentials. This allows us to define the hyperfine coupling strength as  $A = \frac{2\mu_0}{3} g_0 \mu_B \gamma_n \hbar |u(0)|^2 / v_0$  with the volume of the crystal unit cell  $v_0$  [45]. If the electron was smeared out homogeneously over the unit cell in the crystal, we would have  $|u(0)|^2 = 1$ . However the electron density has a sharp maximum at the nucleus, typically  $|u(0)|^2 \sim 10^3$  [43]. Typically, it is useful to rewrite, Eq. 2.16 by using the coupling constant  $A_i$ :

$$H_{HF} = \sum_{i=1}^N A_i \mathbf{I}_i \cdot \mathbf{S}. \quad (2.17)$$

Relevant constants for different isotopes of In, Ga and As, are given in table 2.1. Quadrupole coupling is discussed further in section 2.4.2. Note, that in materials containing several nuclear isotopes  $j$ , each with associated abundance  $v_j$ , r.m.s. average value of hyperfine coupling constant is used:  $A = \sqrt{\sum_j v_j (A_j)^2}$ .

### 2.4.1 ELECTRON SPIN DYNAMICS IN THE NUCLEAR FIELD

In general, the hyperfine interaction can give rise to very rich dynamics. The electron spin state is not only affected by the nuclear spins, but also the electron spin affects the dynamics of the nuclear spin bath and may lead to the complex effects like dynamic nuclear polarization [47–49]. Here, however, we will consider the simplest case when nuclear spins are not affected by the electron. In the following, we use the fact that the dynamics of nuclear spin bath is slow compared to the evolution of the electron spin. In addition, we approximate the effect of the nuclear spin bath on the electron spin evolution as an effective magnetic field acting on electron spin [50]:

$$H_{HF} = \sum_{i=1}^N A_i \mathbf{I}_i \cdot \mathbf{S} = g\mu_B \mathbf{B}_N \mathbf{S}. \quad (2.18)$$

Here  $N$  is the total number of nuclear spins interacting with electron spin and  $\mathbf{B}_N = \sum_{i=1}^N A_i \mathbf{I}_i / g\mu_B$  is the *Overhauser* field originating from nuclear spin bath. In this approximation, the effect of nuclear spins is considered to be a random classical field, that is  $\mathbf{I}_i$  is not considered to be an operator. When all nuclear spins in InAs quantum dot are fully polarized, we have  $|\mathbf{B}_N| \sim 2$  T independent of  $N$ . However, for the temperatures ( $\sim 100$  mK) and magnetic fields ( $\leq 10$  T) in the present experiments, the thermal energy  $k_B T$  dominates the nuclear Zeeman energy and only a small fraction of the nuclear spins are polarized. In addition, the fluctuations of the nuclear field follow a Gaussian distribution with a spread  $\sigma_N \sim A/\sqrt{N}$  [50–52]. The last expression holds in the limit of large  $N$  and for a typical value of  $N \sim 10^6$  nuclei, this results in  $\sigma_N \sim 1$  mT. The measurements of statistical nuclear field distribution are consistent with this estimate for optical dots [53, 54] as well as for electrically measured quantum dots in GaAs [55, 56] and InAs nanowires [48].

As shown in section 2.2.2, a random offset in magnetic field leads to dephasing of electron spin by changing its Larmor precession frequency. For a typical value of nuclear field in a quantum dot  $B_{N,z} \sim 1$  mT, electron spin picks up an extra phase of  $\pi$  within  $\lesssim 5$  ns (assuming  $g = 9$  and  $\mathbf{B}_{\text{ext}}$  to be along  $z$ ). More precisely, the loss of coherence due Gaussian-distributed nuclear fields gives rise to an  $e^{-(t/T_2^*)^2}$  decay of the transverse spin component with  $T_2^* = \sqrt{2\hbar g\mu_B B_{N,z}}$ . This can be obtained by averaging the spin precession over the nuclear field distribution. It should be noted that at large

external magnetic field ( $B_{\text{ext}} \gg B_{\text{N}}$ ) the transverse component of the nuclear field has only a negligible effect on the electron spin dephasing. The transverse component slightly tilts the precession axis by an angle  $\sim B_{\text{N}}/B_{\text{ext}}$  and effectively changes the precession frequency by  $g\mu_{\text{B}}B_{\text{N}}^2/B_{\text{ext}}$  [57].

Several ways are proposed in order to suppress dephasing. Polarizing the nuclear system by a fraction  $p$  suppresses the field distribution by a factor  $1/\sqrt{N(1-p^2)}$  [58, 59]. To achieve an enhancement of  $T_2^*$  by a factor of 100 a very large polarization of 99.99% is needed. Such large polarizations are difficult to achieve experimentally. Several proposals explore the idea of reducing the nuclear field uncertainty by performing measurements of the nuclear field [60–63]. More recently, experiments in lateral GaAs quantum dots showed that by manipulating electron spin, the fluctuations of the nuclear spin bath can be reduced [47, 64, 65]. By reducing nuclear fluctuations, dephasing time was enhanced by more than an order of magnitude [64, 65].

## 2.4.2 DYNAMICS OF THE NUCLEAR FIELD

The electron spin dynamics due to the statistical nuclear field can be reversed by a Hahn echo or dynamical decoupling techniques (see section 2.2.2) as long as the nuclear field is static. However, the nuclear field is changing in time which effectively limits the coherence time. We discuss three interactions which mainly affect evolution of the nuclear spins in InAs nanowires: (i) hyperfine interaction, (ii) dipole interaction between neighboring nuclear spins and (iii) quadrupole coupling of individual nucleus with electric field gradient. The last interaction may be important in the case of indium nuclear spin for which quadrupole moment is relatively large (see table 2.1).

We first consider the hyperfine interaction. From the Hamiltonian in Eq. 2.17 we see that each nucleus experiences a magnetic field  $\sim A/N$ , known as the Knight field, through the hyperfine interaction with the electron spin. At low external magnetic field  $B_{\text{ext}} \ll A/N$  this causes a precession and accordingly a change of the nuclear field. At large magnetic field  $B_{\text{ext}} \gg A/N$  electron and nuclear spins precess around the external magnetic field and the longitudinal component of the nuclear field is preserved, since the change due to precession in the Knight field is strongly suppressed. The quantum mechanical analogue of this picture can be understood by rewriting the hyperfine



interaction Hamiltonian 2.17 in the following way:

$$H = \sum_i^N A_i (\sigma^z I_i^z + \sigma^+ I_i^- + \sigma^- I_i^+). \quad (2.19)$$

Here  $\sigma^\pm$  and  $I^\pm$  correspond to raising and lowering operators for electron and nuclear spin. The last two terms represent electron-nuclear flips-flops that cause fluctuations of the nuclear field. However, due to the difference in Zeeman energy between electron and nuclear spin, this process does not conserve energy. Therefore, it is suppressed by an external magnetic field  $B_{\text{ext}}$ . Still, virtual processes involving two electron-nuclear flip-flops can result in a nuclear-nuclear flip-flop. First a flip-flop between the electron spin and nucleus  $i$  occurs, followed by a flip-flop between the electron spin and nucleus  $j$ . This effectively results in a flip-flop between nucleus  $i$  and nucleus  $j$ . In the whole process electron spin stays the same so the difference in energy between the two configuration ( $\sim A_i - A_j$ ) is small. For  $A_i \neq A_j$  this process changes the nuclear field. While the rate of direct electron-nuclear flip-flops is reduced efficiently with external field ( $1/B_{\text{ext}}^2$ ), the rate of the first order virtual processes scales with  $1/B_{\text{ext}}$ . Therefore, these hyperfine-mediated nuclear flip-flops are harder to suppress. The resulting dynamics due to the nuclear-nuclear flip-flop are a complex many body problem. Hyperfine mediated nuclear flip-flops may be suppressed by inhomogeneous  $A_i$  due to the energy mismatch  $\sim A_i - A_j$  of a flip-flop. Furthermore, because the nuclear dynamics are affected by the electron spin, the coupled electron-nuclear system can lead to coherence decay characteristics different than the usual exponential decay [59].

A second process driving nuclear dynamics is the dipole-dipole interaction between neighboring nuclear spins, which is given in the secular approximation (valid for Zeeman energies larger than the interaction strength  $D$ ) by:

$$H_{i,j} = D(I_i^+ I_j^- + I_i^- I_j^+ - 4I_i^z I_j^z)/2, \quad (2.20)$$

with  $D \sim 1/50 \mu\text{s}$  for InAs [66]. Here, we assume external magnetic field to point in the  $z$ -direction. The first two terms describe flip-flops of nuclear spin pairs which changes  $B_{N,z}$  and therefore affects the electron spin coherence. The timescale of the drift in  $B_{N,z}$  is difficult to evaluate due to various reasons. Most importantly, the flip-flop rate is suppressed when  $A_i - A_{i+1} > D$  due to the associated energy mismatch [67]. For lateral dots in GaAs  $B_{N,x,y}$  is

expected to evolve on a  $100 \mu\text{s}$  timescale while the drift in the longitudinal component  $B_{N,z}$  due to the dipole-dipole interaction may be much longer. The contribution from the dipole-dipole interaction to the electron coherence time is estimated theoretically as  $\sim 10\text{--}100 \mu\text{s}$  [68–71] for GaAs, much faster than the  $B_{N,z}$  drift time. It should be noted that the time scale on which spin decoherence occurs is not only dependent on the typical correlation time of the nuclear spin bath, but also on the amplitude of nuclear field fluctuations. Recent measurements in lateral GaAs quantum dots show typical coherence times of  $\sim 1 \mu\text{s}$  for  $B_{ext} \approx 100 \text{ mT}$  to  $20 \mu\text{s}$  for  $B_{ext} \approx 700 \text{ mT}$  measured by spin echo technique [72, 73]. Surprisingly, for lower magnetic fields ( $\leq 200 \text{ mT}$ ) coherence revivals were observed: coherence is suppressed and revived after a certain time [73]. These oscillations are explained by the precession of Ga and As nuclear spins in the external magnetic field [22, 73].

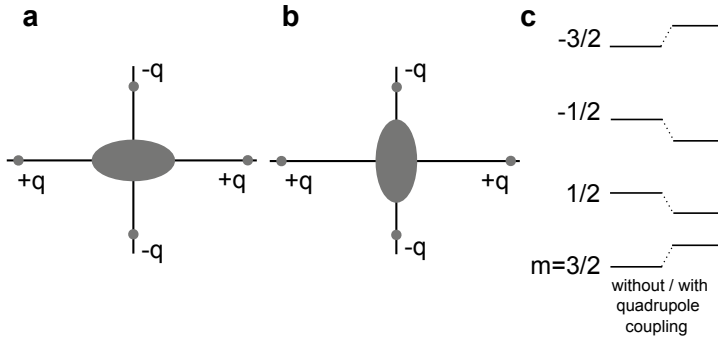


**Figure 2.13:** (a,b) Positively charged nucleus in the field of four charges,  $+q$  on the  $x$ -axis and  $-q$  on the  $y$ -axis. The configuration in (b) has a lower energy. (c) Effect of quadrupole coupling in the first order when Zeeman splitting is larger than quadrupole coupling. In this example  $I=3/2$ . On the left, energies of the Zeeman split states are shown without taking into account quadrupole coupling. The quadrupole coupling shifts energies non-uniformly depending on the projection of the nuclear spin  $m$  (shown on the right). The figure adapted from [17].

A third process which might be important for nuclear dynamics in InAs nanowires is the quadrupole coupling of individual nuclear spins with electric field gradients. Electric field gradients may be present due to, for example, imperfections of a crystal lattice. The quadrupole coupling may be especially important for the dynamics of nuclear spins of In, since the In nuclear quadrupole moment is large (see table 2.1). Importantly, quadrupole coupling may give

rise to shifts in Zeeman energy [17] and facilitate faster nuclear relaxation [74].

The nucleus, in general, is not spherical and the electrostatic energy of the nucleus therefore depends on its orientation in the presence of electric fields (Fig. 2.13a,b). Note that in equilibrium nucleus experiences zero average electric field. However, electric field gradients can still be non-zero which gives rise to the quadrupole Hamiltonian [17]:

$$H_Q = \frac{eQ}{6I(2I-1)} V_{\alpha,\beta} \left[ \frac{3}{2}(I^\alpha I^\beta + I^\beta I^\alpha) - \delta^{\alpha,\beta} I^2 \right]. \quad (2.21)$$

Here,  $eQ$  is the quadrupole moment of the nuclei and  $V_{\alpha,\beta} = \frac{\partial^2 V}{\partial x_\alpha \partial x_\beta}$  are the electric field gradients at the position of the nucleus ( $x_{\alpha,\beta}$  can correspond to any of the three directions in space  $x$ ,  $y$  or  $z$ ), and  $I^\alpha$  corresponds to the nuclear spin component along  $\alpha$ . In order to see which kind of transitions of the nuclei this Hamiltonian induces, it is useful to rewrite it as following:

$$H_Q = \frac{eQ}{6I(2I-1)} [V_0(3I_z^2 - I^2) + V_{+1}(I^- I_z + I_z I^-) + V_{-1}(I^+ I_z + I_z I^+) + V_{+2}(I^-)^2 + V_{-2}(I^+)^2]. \quad (2.22)$$

Here  $V_{0,\pm 1,\pm 2}$  are linear combinations of the gradients defined previously. In general case, when magnetic the field is not aligned to one of the principal axis of electric field gradient tensor, all elements are non-zero. Therefore, the quadrupole coupling may facilitate transitions between nuclear states corresponding to different longitudinal polarizations. Also, the simple picture of equidistant Zeeman levels of nuclear spins is no more valid if the quadrupole coupling is taken into account (Fig. 2.13c). Inhomogeneous quadrupole coupling may lead to suppression of nuclear flip-flops due to dipole-dipole interaction [46]. On the other hand, quadrupole coupling is also expected to lead to fast relaxation of nuclear spins and therefore to faster nuclear dynamics. When large electric field gradients are present in a nanostructure, the nuclear relaxation rates may be as high as  $\sim 3$  MHz [74]. Possible reasons for the existence of electric field gradients in the nanowire quantum dots include strain, wurtzite crystal symmetry, defects in the crystal lattice and at the nanowire surface. Gradients generated by the gates or by charged impurities in the dielectric can also contribute.

### 2.4.3 HYPERFINE AND SPIN-ORBIT EFFECTS IN THE SPIN BLOCKADE REGIME

In the section 2.1.3 we introduced concept of spin blockade which is used for detection of spin states. Here, we briefly explain how the two interactions, spin-orbit and hyperfine, lift the spin blockade, therefore limiting detection fidelity. As we have seen in previous sections nuclear spins create an effective Overhauser field which is felt by electron spin. In a double quantum dot, the Overhauser field for the right dot  $\mathbf{B}_N^R$  and the left dot  $\mathbf{B}_N^L$  is in general different. This leads to an extra term in the Hamiltonian from equation 2.1):

$$\begin{aligned}
 H_{\text{nucl}} &= -\frac{g\mu_B}{\hbar}(\mathbf{B}_N^L \cdot \mathbf{S}_L + \mathbf{B}_N^R \cdot \mathbf{S}_R) \\
 &= -\frac{g\mu_B}{\hbar}(\mathbf{B}_N^L - \mathbf{B}_N^R) \cdot (\mathbf{S}_L - \mathbf{S}_R)/2 \\
 &\quad -\frac{g\mu_B}{\hbar}(\mathbf{B}_N^L + \mathbf{B}_N^R) \cdot (\mathbf{S}_L + \mathbf{S}_R)/2,
 \end{aligned} \tag{2.23}$$

with  $\mathbf{S}_{L(R)}$  being spin operator for the left (right) electron. The average value of the Overhauser field in the two dots  $(\mathbf{B}_N^L + \mathbf{B}_N^R)/2$  simply adds to the Zeeman energy of both dots. The difference  $\Delta\mathbf{B}_N \equiv \mathbf{B}_N^L - \mathbf{B}_N^R$  on the other hand couples the triplet states to the singlet state, as can be seen by combining the spin operators in the following way:

$$\begin{aligned}
 S_L^x - S_R^x &= \frac{\hbar}{\sqrt{2}}\left(|S_{11}\rangle\langle T_{11}^-| - |S_{11}\rangle\langle T_{11}^+| + h.c.\right) \\
 S_L^y - S_R^y &= \frac{\hbar}{\sqrt{2}}\left(i|S_{11}\rangle\langle T_{11}^-| - i|S_{11}\rangle\langle T_{11}^+| + h.c.\right) \\
 S_L^z - S_R^z &= \hbar\left(|S_{11}\rangle\langle T_{11}^0| + |T_{11}^0\rangle\langle S_{11}|\right).
 \end{aligned} \tag{2.24}$$

The first two expressions reveal that the inhomogeneous field in the transverse plane  $\Delta B_N^x$ ,  $\Delta B_N^y$  mixes the  $T_{11}^+$  and  $T_{11}^-$  states with  $S_{11}$ . The longitudinal component  $\Delta B_N^z$  mixes  $T_{11}^0$  with  $S_{11}$  (third expression). The degree of mixing between the two states will depend strongly on the energy difference between them [56].

This is illustrated in Fig. 2.14 where the energies corresponding to the eigenstates of the Hamiltonian  $H_0 + H_{\text{nucl}}$  are plotted as a function of detuning  $\delta$ . We first discuss the case when  $\delta \gg t$ . For small magnetic fields  $B_{\text{ext}} < \sqrt{(\Delta B_N^2)}$

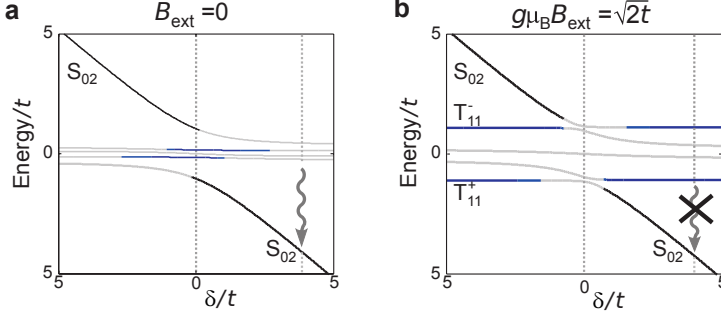


**Figure 2.14:** Energies corresponding to the eigenstates of  $H_0 + H_{\text{nuc}}$  as a function of  $\Delta_{\text{LR}}$  for (a)  $B_{\text{ext}} = 0$  and (b)  $B_{\text{ext}} = \sqrt{2}t$ . Singlet and triplet eigenstates are denoted by dark gray lines. Hybridized states (of singlet and triplet) are denoted by light gray lines. For  $\Delta_{\text{LR}} \gg t$  and  $B_{\text{ext}} \gg |\Delta \mathbf{B}_{\text{N}}|$ , the split-off triplets ( $T_{11}^+$  and  $T_{11}^-$ ) are hardly perturbed and current flow is blocked when they become occupied. Parameters:  $t = 0.2 \mu\text{eV}$ ,  $g\mu_B \mathbf{B}_{\text{N,L}} = (0.03, 0, -0.03) \mu\text{eV}$ ,  $g\mu_B \mathbf{B}_{\text{N,R}} = (-0.03, -0.06, -0.06) \mu\text{eV}$ . The figure adapted from [20].

(Fig. 2.14a), the three triplet states are close in energy to the  $S_{11}$  state. Their intermixing will be strong, and will lift spin blockade. For  $B_{\text{ext}} \gg \sqrt{\langle \Delta B_{\text{N}}^2 \rangle}$  (Fig. 2.14b)  $T_{11}^+$  and  $T_{11}^-$  states are split off in energy by  $g\mu_B B_{\text{ext}}$ . Consequently the perturbation of these states caused by the nuclei will be small. Although  $T_{11}^0$  remains mixed with  $S_{11}$  state, the occupation of one of the two split-off triplet states can block the current. The situation for  $\delta \sim 0$  is more complicated due to a competition between the exchange interaction and nuclear and external magnetic fields. In contrast with the previous case, increasing  $B_{\text{ext}}$  from 0 to  $\sqrt{2}t/g\mu_B$  gives an increase of singlet-triplet mixing, as illustrated in Fig. 2.14b. Theoretical calculations of the nuclear spin-mediated current, obtained from a master equation approach, are discussed in Ref. [75, 76].

As discussed in section 2.3.4, strong spin-orbit interaction hybridizes triplet  $T_{11}$  states with  $S_{02}$ . This may lead to finite leakage current in the spin blockade regime at finite magnetic field. At zero magnetic field, due to the time-reversal symmetry, spin-orbit interaction does not have an observable effect. Out of four (1,1) states, three are blocked as in the case when spin-orbit coupling is zero. The leakage current may still occur via hyperfine interaction as discussed earlier.

Let us consider now the case of finite magnetic field when the triplet states  $T_{11}^{\pm}$  are well separated in energy. Because of the hybridization with  $S_{02}$  (see section 2.3.4), these states are no longer blocked. Effectively, there are three

states which are coupled to the  $S_{02}$  and only one state,  $T_{11}^0$ , which is blocked<sup>2</sup> [42]. As in the case of zero magnetic field, the hyperfine interaction may couple the remaining blocked state to the one of the three unblocked states and lift spin blockade.

The interplay between hyperfine and spin-orbit interaction is discussed further in chapter 5. Depending on the tunnel coupling between the dots, and the thickness of the outgoing barrier leakage current can be larger or smaller at zero magnetic field. Also, the hybridization between the (1,1) states and  $S_{02}$  depends on the orientation of magnetic field with respect to the nanowire. Anisotropy of spin blockade is discussed in chapter 6.

## REFERENCES

- [1] L. P. Kouwenhoven, C. M. Marcus, P. L. McEuen, S. Tarucha, R. M. Westervelt, and N. S. Wingreen, *Electron transport in quantum dots* (Kluwer, 1997).
- [2] L. P. Kouwenhoven, D. G. Austing, and S. Tarucha, *Few-electron quantum dots*, Rep. Prog. Phys. **64**, 701 (2001).
- [3] W. G. van der Wiel, S. D. Franceschi, J. M. Elzerman, T. Fujisawa, S. Tarucha, and L. P. Kouwenhoven, Rev. Mod. Phys. **75**, 1 (2002).
- [4] J. R. Petta, A. C. Johnson, J. M. Taylor, E. A. Laird, A. Yacoby, M. D. Lukin, C. M. Marcus, M. P. Hanson, and A. C. Gossard, *Coherent Manipulation of Coupled Electron Spins in Semiconductor Quantum Dots*, Science **309**, 2180 (2005).
- [5] F. H. L. Koppens, C. Buizert, K.-J. Tielrooij, I. T. Vink, K. C. Nowack, L. P. Meunier, T. Kouwenhoven, and L. M. K. Vandersypen, *Driven coherent oscillations of a single electron spin in a quantum dot*, Nature **442**, 776 (2006).
- [6] K. C. Nowack, F. H. L. Koppens, Y. V. Nazarov, and L. M. K. Vandersypen, *Coherent Control of a Single Electron Spin with Electric Fields*, Science **318**, 1430 (2007).

---

<sup>2</sup>In the case of strong spin-orbit interaction the blocked state can be superposition of  $S_{11}$  and  $T_{11}^0$ , see Ref. [42].

- [7] D. Loss and D. P. DiVincenzo, *Quantum computation with quantum dots*, Phys. Rev. A **57**, 120 (1998).
- [8] R. Hanson, L. H. Willems van Beveren, I. T. Vink, J. M. Elzerman, W. J. M. Naber, F. H. L. Koppens, L. P. Kouwenhoven, and L. M. K. Vandersypen, *Single-Shot Readout of Electron Spin States in a Quantum Dot Using Spin-Dependent Tunnel Rates*, Phys. Rev. Lett. **94**, 196802 (2005).
- [9] J. M. Elzerman, R. Hanson, L. H. Willems van Beveren, B. Witkamp, L. M. K. Vandersypen, and L. P. Kouwenhoven, *Single-shot read-out of an individual electron spin in a quantum dot*, Nature **430**, 431 (2004).
- [10] C. Poole, *Electron Spin Resonance, 2nd ed.* (Wiley, New York, 1983).
- [11] E. A. Laird, C. Barthel, E. I. Rashba, C. M. Marcus, M. P. Hanson, and A. C. Gossard, *Hyperfine-Mediated Gate-Driven Electron Spin Resonance*, Phys. Rev. Lett. **99**, 246601 (2007).
- [12] M. Pioro-Ladriere, T. Obata, Y. Tokura, Y. Shin, T. Kubo, K. Yoshida, T. Taniyama, and S. Tarucha, *Electrically driven single-electron spin resonance in a slanting Zeeman field*, Nature Physics **4**, 776 (2008).
- [13] S. Frolov, S. Lüscher, W. Yu, Y. Ren, J. Folk, and W. Wegscheider, *Ballistic spin resonance*, Nature **458**, 868 (2009).
- [14] Y. Kato, R. C. Myers, A. C. Gossard, and D. D. Awschalom, *Coherent spin manipulation without magnetic fields in strained semiconductors*, Nature **427**, 50 (2004).
- [15] T. Obata, M. Pioro-Ladrière, Y. Tokura, Y.-S. Shin, T. Kubo, K. Yoshida, T. Taniyama, and S. Tarucha, *Coherent manipulation of individual electron spin in a double quantum dot integrated with a micromagnet*, Phys. Rev. B **81**, 085317 (2010).
- [16] M. Nielsen and I. Chuang, *Quantum computation and information* (Cambridge University Press, Cambridge, UK, 2000).
- [17] C. P. Slichter, *Principles of Magnetic Resonance, 3rd ed.* (Springer-Verlag, Berlin, 1990).

- 
- [18] J. M. Martinis, S. Nam, J. Aumentado, K. M. Lang, and C. Urbina, *Decoherence of a superconducting qubit due to bias noise*, Phys. Rev. B **67**, 094510 (2003).
- [19] G. Ithier, E. Collin, P. Joyez, P. J. Meeson, D. Vion, D. Esteve, F. Chiarello, A. Shnirman, Y. Makhlin, J. Schrieffer, et al., *Decoherence in a superconducting quantum bit circuit*, Phys. Rev. B **72**, 134519 (2005).
- [20] K. C. Nowack, Ph.D. thesis, Delft University of Technology (2009).
- [21] A. Abragam, *The Principles of Nuclear Magnetism*, Clarendon (Oxford, 1961).
- [22] Ł. Cywiński, W. Witzel, and S. Das Sarma, *Electron spin dephasing due to hyperfine interactions with a nuclear spin bath*, Phys. Rev. Lett. **102**, 57601 (2009).
- [23] H. J. Joyce, J. Wong-Leung, Q. Gao, H. H. Tan, and C. Jagadish, *Phase Perfection in Zinc Blende and Wurtzite III-V Nanowires Using Basic Growth Parameters*, Nano Letters **10**, 908 (2010).
- [24] K. A. Dick, C. Thelander, L. Samuelson, and P. Caroff, *Crystal Phase Engineering in Single InAs Nanowires*, Nano Letters **10**, 3494 (2010).
- [25] G. Dresselhaus, *Spin-Orbit Coupling Effects in Zinc Blende Structures*, Phys. Rev. **100**, 580 (1955).
- [26] I. Zorkani and E. Kartheuser, *Resonant magneto-optical spin transitions in zinc-blende and wurtzite semiconductors*, Phys. Rev. B **53**, 1871 (1996).
- [27] C. Fasth, A. Fuhrer, L. Samuelson, V. N. Golovach, and D. Loss, *Direct Measurement of the Spin-Orbit Interaction in a Two-Electron InAs Nanowire Quantum Dot*, Phys. Rev. Lett. **98**, 266801 (2007).
- [28] M. I. Dyakonov, *Spin Physics in Semiconductors - springer series in solid-state physics 157* (Springer-Verlag, Berlin Heidelberg, 2008), ISBN 978-3-540-78819-5.
- [29] L. Lew Yan Voon and M. Willantzen, *The kp method* (Springer-Verlag Berlin Heidelberg, 2009).



- [30] R. Winkler, *Spin-Orbit Coupling Effects in Two-Dimensional Electron and Hole Systems* (Springer-Verlag, 2003).
- [31] A. De and C. E. Pryor, *Calculation of Landé  $g$  factors for III-V nanowhisker quantum dots and comparison with experiment*, Phys. Rev. B **76**, 155321 (2007).
- [32] A. De and C. E. Pryor, *Predicted band structures of III-V semiconductors in the wurtzite phase*, Phys. Rev. B **81**, 155210 (2010).
- [33] M. Trif, V. N. Golovach, and D. Loss, *Spin dynamics in InAs nanowire quantum dots coupled to a transmission line*, Phys. Rev. B **77**, 045434 (2008).
- [34] C. Flindt, A. S. Sørensen, and K. Flensberg, *Spin-Orbit Mediated Control of Spin Qubits*, Phys. Rev. Lett. **97**, 240501 (2006).
- [35] L. S. Levitov and E. I. Rashba, *Dynamical spin-electric coupling in a quantum dot*, Phys. Rev. B **67**, 115324 (2003).
- [36] R. Hanson, L. P. Kouwenhoven, J. R. Petta, S. Tarucha, and L. M. K. Vandersypen, *Spins in few-electron quantum dots*, Rev. Mod. Phys. **79**, 1217 (2007).
- [37] A. E. Hansen, M. T. Björk, C. Fasth, C. Thelander, and L. Samuelson, *Spin relaxation in InAs nanowires studied by tunable weak antilocalization*, Phys. Rev. B **71**, 205328 (2005).
- [38] M. T. Björk, A. Fuhrer, A. E. Hansen, M. W. Larsson, L. E. Fröberg, and L. Samuelson, *Tunable effective  $g$  factor in InAs nanowire quantum dots*, Phys. Rev. B **72**, 201307 (2005).
- [39] S. Amasha, K. MacLean, I. P. Radu, D. M. Zumbühl, M. A. Kastner, M. P. Hanson, and A. C. Gossard, *Electrical Control of Spin Relaxation in a Quantum Dot*, Phys. Rev. Lett. **100**, 046803 (2008).
- [40] A. V. Khaetskii and Y. V. Nazarov, *Spin-flip transitions between Zeeman sublevels in semiconductor quantum dots*, Phys. Rev. B **64**, 125316 (2001).
- [41] K. V. Kavokin, *Anisotropic exchange interaction of localized conduction-band electrons in semiconductors*, Phys. Rev. B **64**, 075305 (2001).

- 
- [42] J. Danon and Y. V. Nazarov, *Pauli spin blockade in the presence of strong spin-orbit coupling*, Phys. Rev. B **80**, 041301 (2009).
- [43] D. Paget, G. Lampel, B. Sapoval, and V. I. Safarov, *Low field electron-nuclear spin coupling in gallium arsenide under optical pumping conditions*, Phys. Rev. B **15**, 5780 (1977).
- [44] E. Fermi, *Über die magnetischen Momente der Atomkerne*, Zeitschrift für Physik **60**, 320 (1930).
- [45] F. Meier and B. P. Zakharchenya, *Optical orientation. Modern problems in condensed matter sciences* (North-Holland, 1984), ISBN 978-04-448-6741-4.
- [46] W. A. Coish and J. Baugh, *Nuclear spins in nanostructures*, physica status solidi (b) **246**, 2203 (2009).
- [47] Vink I. T., Nowack K. C., Koppens F. H. L., Danon J., Nazarov Y. V. and Vandersypen L. M. K., *Locking electron spins into magnetic resonance by electron-nuclear feedback*, Nature Physics **5**, 764 (2009).
- [48] A. Pfund, I. Shorubalko, K. Ensslin, and R. Leturcq, *Suppression of Spin Relaxation in an InAs Nanowire Double Quantum Dot*, Phys. Rev. Lett. **99**, 036801 (2007).
- [49] K. Ono and S. Tarucha, *Nuclear-Spin-Induced Oscillatory Current in Spin-Blockaded Quantum Dots*, Phys. Rev. Lett. **92**, 256803 (2004).
- [50] I. A. Merkulov, A. L. Efros, and M. Rosen, *Electron spin relaxation by nuclei in semiconductor quantum dots*, Phys. Rev. B **65**, 205309 (2002).
- [51] A. V. Khaetskii, D. Loss, and L. Glazman, *Electron Spin Decoherence in Quantum Dots due to Interaction with Nuclei*, Phys. Rev. Lett. **88**, 186802 (2002).
- [52] J. Taylor, J. Petta, A. Johnson, A. Yacoby, C. Marcus, and M. Lukin, *Relaxation, dephasing, and quantum control of electron spins in double quantum dots*, Phys. Rev. B **76**, 35315 (2007).

- [53] P. F. Braun, X. Marie, L. Lombez, B. Urbaszek, T. Amand, P. Renucci, V. K. Kalevich, K. V. Kavokin, O. Krebs, P. Voisin, et al., *Direct Observation of the Electron Spin Relaxation Induced by Nuclei in Quantum Dots*, Phys. Rev. Lett. **94**, 116601 (2005).
- [54] M. V. G. Dutt, J. Cheng, B. Li, X. D. Xu, X. Q. Li, P. R. Berman, D. G. Steel, A. S. Bracker, D. Gammon, S. E. Economou, et al., *Stimulated and spontaneous optical generation of electron spin coherence in charged GaAs quantum dots*, Phys. Rev. Lett. **94**, 227403 (2005).
- [55] A. C. Johnson, J. R. Petta, J. M. Taylor, A. Yacoby, M. D. Lukin, C. M. Marcus, M. P. Hanson, and A. C. Gossard, *Triplet-singlet spin relaxation via nuclei in a double quantum dot*, Nature **435**, 925 (2005).
- [56] F. H. L. Koppens, J. A. Folk, J. M. Elzerman, R. Hanson, L. H. Willems van Beveren, I. T. Vink, H.-P. Tranitz, W. Wegscheider, L. P. Kouwenhoven, and L. M. K. Vandersypen, *Control and Detection of Singlet-Triplet Mixing in a Random Nuclear Field*, Science **309**, 1246 (2005).
- [57] S. I. Erlingsson, Y. V. Nazarov, and V. I. Fal'ko, *Nucleus-mediated spin-flip transitions in GaAs quantum dots*, Phys. Rev. B **64**, 195306 (2001).
- [58] J. Schliemann, A. V. Khaetskii, and D. Loss, *Spin decay and quantum parallelism*, Phys. Rev. B **66**, 245303 (2002).
- [59] W. A. Coish and D. Loss, *Hyperfine interaction in a quantum dot: Non-Markovian electron spin dynamics*, Phys. Rev. B **70**, 195340 (2004).
- [60] D. Klauser, W. A. Coish, and D. Loss, *Nuclear spin state narrowing via gate-controlled Rabi oscillations in a double quantum dot*, Phys. Rev. B **73**, 205302 (2006).
- [61] D. Stepanenko, G. Burkard, G. Giedke, and A. Imamoglu, *Enhancement of Electron Spin Coherence by Optical Preparation of Nuclear Spins*, Phys. Rev. Lett. **96**, 136401 (2006).
- [62] O. Cakir and T. Takagahara, *Quantum Dynamics of Electron-Nuclei Coupled System in a Double Quantum Dot*, Arxiv preprint cond-mat/0609217 (2006).

- 
- [63] G. Giedke, J. M. Taylor, D. D'Alessandro, M. D. Lukin, and A. Imamoglu, *Quantum measurement of a mesoscopic spin ensemble*, Phys. Rev. A **74**, 32316 (2006).
- [64] D. Reilly, J. Taylor, J. Petta, C. Marcus, M. Hanson, and A. Gossard, *Suppressing Spin Qubit Dephasing by Nuclear State Preparation*, Science **321**, 817 (2008).
- [65] H. Bluhm, S. Foletti, D. Mahalu, V. Umansky, and A. Yacoby, *Enhancing the Coherence of a Spin Qubit by Operating it as a Feedback Loop That Controls its Nuclear Spin Bath*, Phys. Rev. Lett. **105**, 216803 (2010).
- [66] R. G. Shulman, B. J. Wyluda, and H. J. Hrostowski, *Nuclear Magnetic Resonance in Semiconductors. III. Exchange Broadening in GaAs and InAs*, Phys. Rev. **109**, 808 (1958).
- [67] C. Deng and X. Hu, *Analytical solution of electron spin decoherence through hyperfine interaction in a quantum dot*, Phys. Rev. B **73**, 241303(R) (2006).
- [68] R. de Sousa and S. Das Sarma, *Theory of nuclear-induced spectral diffusion: Spin decoherence of phosphorus donors in Si and GaAs quantum dots*, Phys. Rev. B **68**, 115322 (2003).
- [69] R. de Sousa and S. Das Sarma, *Electron spin coherence in semiconductors: Considerations for a spin-based solid-state quantum computer architecture*, Phys. Rev. B **67**, 33301 (2003).
- [70] W. Yao, R. B. Liu, and L. J. Sham, *Theory of electron spin decoherence by interacting nuclear spins in a quantum dot*, Phys. Rev. B **74**, 195301 (2006).
- [71] W. Witzel and S. Das Sarma, *Quantum theory for electron spin decoherence induced by nuclear spin dynamics in semiconductor quantum computer architectures: Spectral diffusion of localized electron spins in the nuclear solid-state environment*, Phys. Rev. B **74**, 35322 (2006).
- [72] F. Koppens, D. Klauser, W. Coish, K. Nowack, L. Kouwenhoven, D. Loss, and L. Vandersypen, *Universal phase shift and nonexponential decay of driven single-spin oscillations*, Phys. Rev. Lett. **99**, 106803 (2007).

- [73] H. Bluhm, S. Foletti, I. Neder, M. Rudner, D. Mahalu, V. Umansky, and A. Yacoby, *Long coherence of electron spins coupled to a nuclear spin bath*, ArXiv e-prints (2010), 1005.2995.
- [74] C. Deng and X. Hu, *Selective dynamic nuclear spin polarization in a spin-blocked double dot*, Phys. Rev. B **71**, 033307 (2005).
- [75] O. N. Jouravlev and Y. V. Nazarov, *Electron transport in a double quantum dot governed by a nuclear magnetic field*, Phys. Rev. Lett. **96**, 176804 (2006).
- [76] J. Inarrea, G. Platero, and A. MacDonald, *Double-dot transport in the spin blockade regime*, Phys. Rev. B **76**, 085329 (2007).

# 3

## DEVICE FABRICATION AND MEASUREMENT SETUP

This chapter describes the steps involved in making tunable quantum dots in nanowires. The InAs nanowires used in this thesis are grown at Philips Research in Eindhoven. After growth, further device processing was done at the Delft Institute of Microelectronics and Submicron-technology (DIMES) and in the TU Delft Nanolab / VLL (Van Leeuwenhoek laboratory).

### 3.1 NANOWIRE GROWTH

The historically dominant top-down fabrication method becomes technologically increasingly difficult when it comes to submicron- or even nano-sized structures. This is mainly due to the wavelength of light limiting the resolution in photolithography. Despite the great deal of effort that has been put into lowering this wavelength, it is not surprising that research is also shifting towards bottom-up fabrication, where self-alignment, self-assembly and self-organization are key ingredients. Concerning nanowires, both top-down and bottom-up approaches can be used. Top-down fabrication method typically starts with bulk material that is etched away to form a nanostructure, whereas in the bottom-up fabrication nanowires are grown from catalyst particles when precursor gases are supplied.

To grow InAs nanowires, 5 to 20 nm diameter gold colloids are spun on an InP substrate. The substrate is then placed in a metal organic vapour phase epitaxy (MOVPE) chamber, where it is annealed at 550°C under phosphine (PH<sub>3</sub>) to desorb any oxide which is present at the surface (Fig. 3.1a). At this temperature the gold melts and forms a metal-semiconductor alloy with In. After this step the temperature in the chamber is lowered to 420°C and the PH<sub>3</sub> precursor gas is replaced by arsine (AsH<sub>3</sub>) and trimethylindium (TMIn). This initiates nanowire growth via the vapour-liquid-solid (VLS) mechanism [1]. At this temperature, the precursor gas trimethylindium decomposes into elemental In by successively releasing its methyl groups. The gold particle which acts as a catalyst is believed to facilitate this decomposition [2]. In the process, the elemental In is absorbed by the gold liquid droplet. This droplet serves as a seed for the nanowire growth: when the In concentration reaches the supersaturation, the In condenses under the catalyst and reacts with the As to form InAs. This effectively pushes the liquid droplet upwards as more and more mono-layers are formed.

The nanowire growth temperature of 420°C is below the eutectic temperature of Au-In, 455°C and the exact composition of the gold nanoparticle (liquid or solid) during growth is not known with certitude. In fact InAs nanowire growth from solid catalyst particles has also been observed [3]. Here the Au particle shows clear crystal structure during growth. This is why a vapour-solid-solid (VSS) mechanism [4] was suggested as an alternative explanation. However, based on the relatively high growth rate in our nanowires, the droplet

is considered to be liquid.

The surface mobility of In gives rise to a relatively large size of the material collection area. Therefore, the nanowire growth rate is influenced by the distance between wires. If they are too close, the collection areas overlap and the wires compete for material. If the wires are far away from each other, their growth is independent. In the intermediate or synergetic regime, a more complicated dependence of growth rate on nanowire distance can be seen [2]. Wires that are closer together have an increased growth rate due to an enhanced catalyst surface ratio [2, 5]. For our nanowires the catalyst particles are randomly dispersed on the substrate, which gives rise to different growth rates ultimately yielding wires with different lengths. For our experiments nanowires with a typical length of 5-20  $\mu\text{m}$  and diameters of 40 - 250 nm have been used. The diameter at the top of the nanowires, near the catalyst particle, is roughly determined by the particle size. Due to parasitic radial growth the nanowires are tapered and can have larger diameters depending on growth time.

Position control of nanowires on the growth substrate can be gained by controlling the position of the catalyst particles prior to growth. This can be done using lithography or nanoimprint techniques. An advantage of this control is that the wires can be regularly spaced over the substrate, which will eliminate growth differences due to differences in collection area or synergetic processes.

Despite the fact that bulk InAs has a zincblende crystal symmetry, InAs nanowires often grow in a wurtzite crystal symmetry. For nanowires, wurtzite is more common because of a lower structure formation energy at the catalyst-nanowire interface during growth [6], however adjusting the growth conditions allows also the zincblende structure to be grown [7, 8]. The nanowire grows along the wurtzite [0001] (hexagonal) axis, which corresponds to the zincblende [111] (cubic) direction. Along this axis, wurtzite has an *ABABAB* stacking whereas zincblende has *ABCABC*. Our nanowires have a wurtzite structure determined by transmission electron microscopy (Fig. 3.1c), however stacking faults may be present when a single bilayer is misplaced. This can be considered as a zincblende stacking sequence inserted into the wurtzite crystal [9].



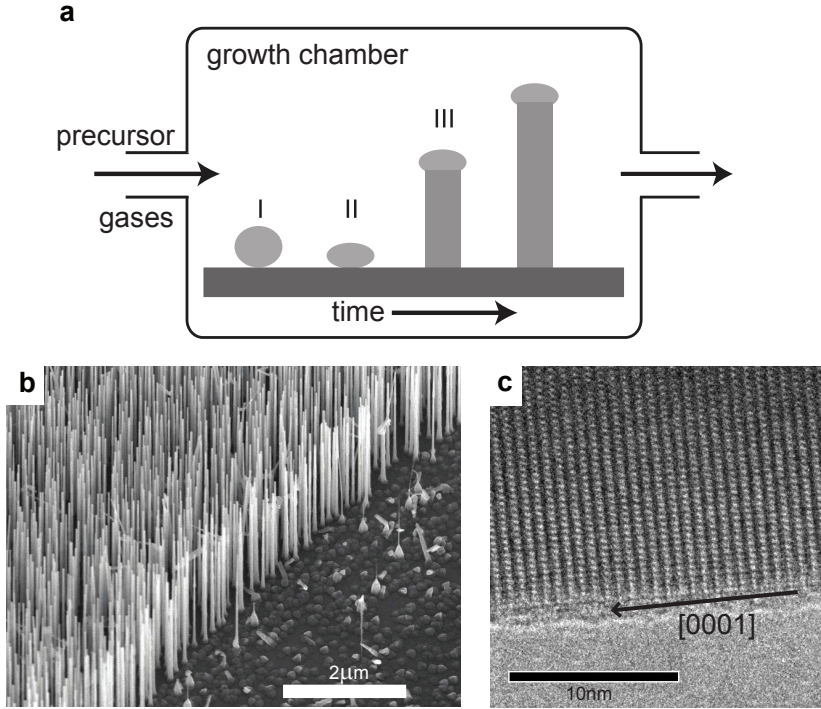


**Figure 3.1:** (a) Schematic of nanowire growth using catalytic metal organic vapour phase epitaxy (MOVPE). (I) Gold catalyst particles are spun on a InP wafer. (II) An annealing step forms an alloy between the gold particle and the In from the substrate. (III) During growth, semiconductor material crystallizes directly under the catalyst, which in turn pushes the gold particle upwards. (b) Scanning electron microscope (SEM) image showing the growth chip with nanowires grown on top of it along an intentionally made scratch. (c) Transmission electron microscope (TEM) image of an InAs nanowire showing wurtzite crystal structure.

## 3.2 DEVICE FABRICATION

Nanowires on a (111) substrate grow vertically, as can be seen in Fig. 3.1b. They can be used directly in a device using the substrate as one contact and the gold particle as the other [10, 11]. For the purpose of this project, however, the wires are broken off and transferred to a degenerately p-doped Si substrate covered with 285 nm of thermally-grown  $\text{SiO}_2$ . This substrate has already been

prepared with position markers and gates. All the fabrication processes after this step involve top-down methods.

There are several ways to transfer the wires: 1) direct contact between the growth chip and the Si substrate, 2) putting the growth chip into a solution and breaking the wires off through sonication and depositing a droplet of the solution onto the substrate or 3) gently touching the growth chip and then the substrate with a tip made from cleanroom paper. We found that the latter method is the most accurate way to get wires from a certain area on the growth chip and deposit them in a designated region on the substrate. The other two methods cause much stronger wear on the wires and the growth chip, making it hard to continue getting good quality wires after a couple of depositions. All wires shown in this work were transferred using the paper tip method.

### 3.2.1 NANOWIRE CONTACTS

In order to be able to send current through the nanowires and measure their resistances, ohmic contacts have been attached to either side of the InAs nanowire. InAs has a strong Fermi-level pinning in the conduction band, which gives rise to an electron accumulation channel close to the surface [12]. The absence of a Schottky barrier at the interface between the contact and the InAs facilitates electron injection and allows low resistance contacts.

Contacts are fabricated via electron beam (e-beam) lithography, see Fig. 3.2. First, a double layer of organic polymers is spun. The bottom layer consists of a low density/length poly-methyl-methacrylate and methyl-acetoacetate mixture (PMMA-MAA 17.5%, 495K in 6% anisole) and the top layer is made with a thinner, higher density PMMA (PMMA 950K, 2% anisole). The contact pattern is defined by writing in the resist with a focused electron beam. The electron beam locally breaks up the polymer chains, which allows them to be removed by a developer (mixture of methyl isobutyl ketone, MIBK and 2-propanol, IPA in 1:3 ratio), followed by a rinse in IPA to stop the development. As the first polymer layer is more sensitive to the ebeam exposure a typical undercut develops which facilitates metal lift-off later on.

Prior to metal deposition in the evaporator, the native oxides that are present on the nanowire surface are removed at the regions of the nanowire that were exposed after e-beam lithography (by etching in Ammonium buffered HF for 10-15 s). Then, metal Ti(10 nm)/Al(100-150 nm) is deposited, only making

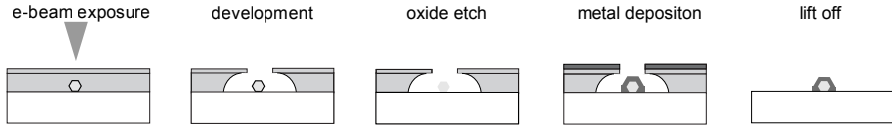


**Figure 3.2:** Successive steps for fabricating nanowire contacts. From left to right: resist deposition and e-beam writing, development of exposed resist with the typical undercut formation, etching of the nanowire oxide, metal deposition in the evaporator and finally the lift-off of the remaining resist.

contact with the parts of the nanowire where the resist has been exposed with the e-beam and removed during development.

The last step is to remove the remaining resist with acetone. The metal that was deposited onto the resist is removed in this lift-off step. The undercut that has formed in the resist profile greatly facilitates the lift-off. In the end, the metal contacts are only present in the area where the e-beam has initially written a pattern.

### 3.2.2 GATES

The degenerately-doped Si substrate can be used as a global back gate to change the electrostatic potential of the nanowire and fill or empty it with electrons. This is done by simply attaching an electrode to the backside of the Si chip. Local gates have been fabricated to allow position control of the electrostatic potential in the wires. Two different gate geometries, i.e. top-gates and bottom-gates have been tried. As all of the measurements in this thesis are done using bottom-gates the focus will be on this geometry. The top-gates will be discussed briefly in section 3.2.3.

Bottom gates are fabricated on an empty Si/SiO<sub>2</sub> chip by spinning a single layer of e-beam resist (PMMA 950K, 2% anisol) and writing an e-beam pattern that consists of roughly 30000 sets of gates with contact pads. After development, evaporation (Ti(5 nm)/Au(10 nm)) and lift-off, the sample looks like the one in Fig. 3.3a. The darker strips in the SEM image consist of 20 nm sputtered Si<sub>3</sub>N<sub>4</sub> dielectric that electrically isolates the gates from the nanowires that are deposited on top of it. Nanowires are dispersed randomly from the growth-chip onto the gate patterns using a paper tip. On a typical sample, a large number of long nanowires can be found that overlap a set of gates (inset Fig. 3.3a). In the last step, we fabricate the contacts for individual

nanowires and metal gates (see Fig. 3.3b).

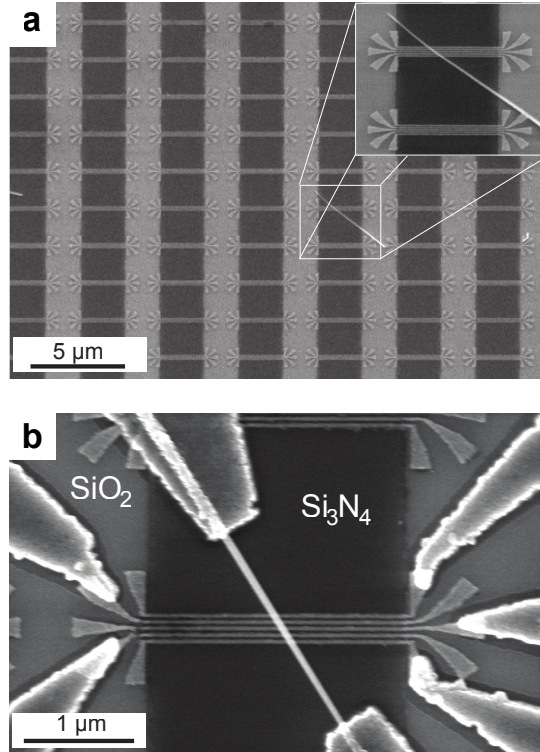


**Figure 3.3:** (a) SEM image showing predefined bottom gates with an InAs nanowire crossing a set of five. The wire is electrically isolated from the gates by a sputtered  $\text{Si}_3\text{N}_4$  dielectric. The areas at the ends of the gates have no dielectric on top. Here electrical contacts will be made in a later processing step. (b) SEM image of the final device, showing the electrical connections to the nanowire and the gates.

An advantage of this gate geometry is that very narrow gates (25nm width, 30 nm spacing) can be written on a flat and clean substrate. Furthermore, post-selection can be done on the deposited nanowires to select only the ones where the gate fabrication was successful. This boosts the yield of nanowires with properly working gates to nearly 100%. Only one last processing step is performed after depositing the nanowires. This reduces the chance of pollution on the wires due to processing residues. This last step is the fabrication of metal contacts. Importantly, in this step the wire is only exposed to the e-

beam at its two far ends, leaving the vital section where the quantum dots will be formed away from its possible detrimental effects.

After the final processing step, the sample is glued onto a 32-pin chip carrier using conducting silver paint. Aluminum bond wires connect the on-chip bonding pads to the ones on the chip carrier. The conducting paint ensures contact to the Si substrate for back gate operation. The chip carrier can be mounted into a cryostat where metal wires connect it to voltage and current probes to perform transport measurements at low temperatures, see Fig. 3.5.

Before cooling down the chip we keep the sample in high vacuum ( $P \sim 10^{-5}$  mbar) for at least 48h. This can lower the nanowire two terminal resistance by one or two orders of magnitude. We presume the drop in resistance for InAs nanowires can be attributed to a change in the surface states due to desorption of water molecules, which changes the electron density or mobility.

### 3.2.3 GATE LEAKAGE

An important demand on the gates is that they should have virtually zero leakage current to the nanowire. The presence of an accumulation layer at the surface of InAs, however makes it in practice difficult to gate without charge leakage [12]. Putting Al or Au directly on top of GaAs produces a Schottky barrier, whereas doing this on InAs produces low resistance contacts. For 2-dimensional InAs systems a dielectric layer has been effective in suppressing the gate leakage [13, 14]. For InAs nanowires, the native surface oxide that forms after growth is often used [15, 16].

However, the native surface oxide on the nanowires we used is not a reliable dielectric. Small leakage currents are present in over 90% of the devices that we measured without additional dielectric. The small leakage is not measurable directly but leads to severe instabilities in the data. An example is shown in Figure 3.4. Applying negative voltages to the top gates forms a quantum dot inside the nanowire. As can be seen in Figure 3.4b, the corresponding Coulomb diamonds show large charge switches that are random in time and gate voltage. We attribute these instabilities to the presence of several quasi-stable charge configurations in the dielectric near the quantum dot. Electrons from the gates can hop through the dielectric via these intermediate states [17]. Due to the close proximity of these states to the dot, the change in capacitive coupling produces a shift in the dot potential.

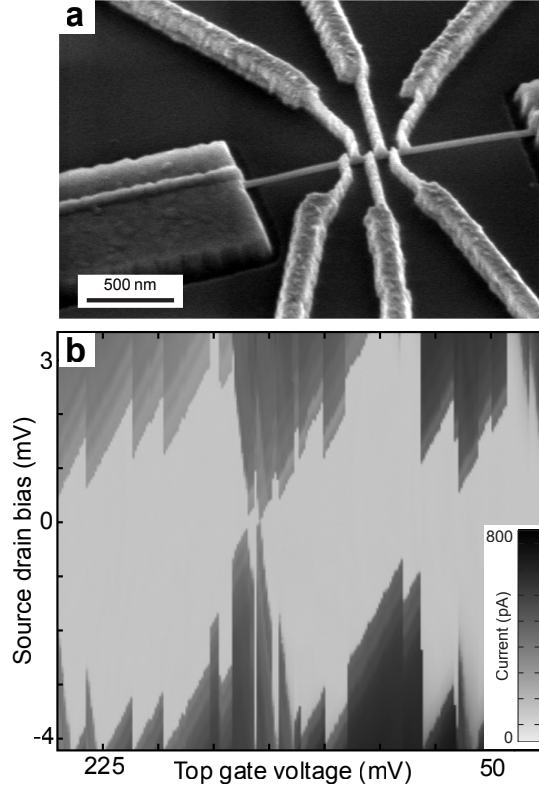


**Figure 3.4:** (a) Nanowire with six top gates. (b) Coulomb diamonds of a quantum dot created by top gates showing strong charge instabilities due to gate leakage.

Several tests confirmed that charge switches in the data are due to poor native oxide on the InAs surface. Besides instabilities observed in top-gated devices, similar problems were observed if we use bottom gates without depositing dielectric between gates and the wire. On the other hand, almost all devices (yield > 95%) in which the gates were separated from the wire by  $\approx 20\text{nm}$  of  $\text{Si}_3\text{N}_4$  show data with no charge switches. It should be noted that in top-gated devices leakage was suppressed, when we separated the gates from the nanowire by depositing the dielectric before the top-gates.

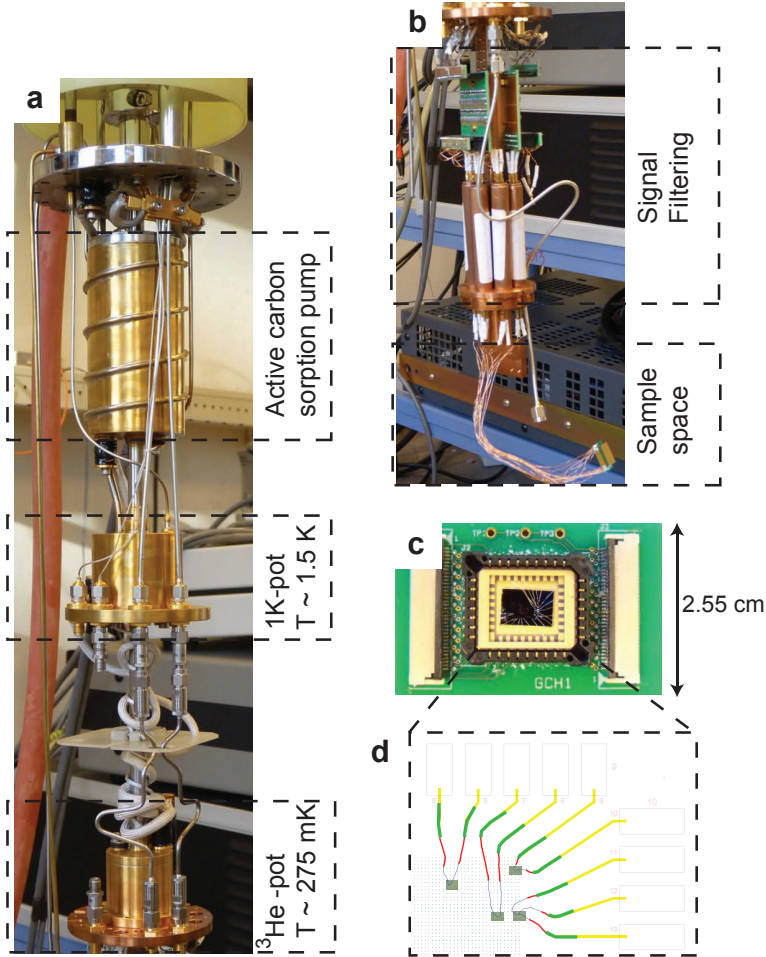


**Figure 3.5:** (a) Insert of the  $^3\text{He}$  refrigerator showing the elements through which base temperature can be reached. The entire insert is immersed into liquid He at 4.2K. The 1K pot fills with He, which is pumped to reduce its vapour pressure and consequently its temperature to 1.5 K. At the 1K pot,  $^3\text{He}$  from a separated circuit will condense and form a liquid inside the  $^3\text{He}$ -pot. When cooled below 30 K the active carbon reduces the pressure in the  $^3\text{He}$  circuit to cool down to  $\sim 250 \text{ mK}$ . (b) Several filtering elements reduce the interference of high-frequency signals with our measurement signal. Shown are low temperature RC-filters and copper powder filters. At room temperature the signal wires are filtered with  $\pi$ -filters. (c) The image of the sample which is mounted and bonded to a chip carrier (d) Design of the electrical contacts to the nanowires made using Computer Aided Design (CAD) program.

### 3.3 MEASUREMENT SETUP

The typical charging and orbital energies in the few-electron quantum dots are on the order of a few meV. The quantum mechanical and spin properties we are interested in occur on an even smaller energy scale. To study them we need to cool our samples to low temperatures, ranging from 1.7 K down to 30 mK. To reach such low temperatures, samples are usually cooled in either a  $^3\text{He}$  sorption ( $\sim 250$  mK) or a dilution refrigerator ( $\sim 30$  mK).

The measurement electronics that are connected to the device, *i.e.* current-to-voltage (IV) converter, voltage sources and digital-to-analog converters are in-house-built <sup>1</sup>. In order to avoid coupling of interference coming from external measurement devices and data-acquisition equipment to the device optical isolation is used. All circuitry at the sample side is analog, battery-powered and can use a ground separate from the ground of the power grid. Figure 3.5 shows the insert of a  $^3\text{He}$  refrigerator that was used for measurements.

### 3.4 HIGH-FREQUENCY SIGNALS

For the experiment discussed in chapter 7, the original design of the devices and sample holders was changed in order to enable high frequency signals to reach the sample, minimizing the losses and crosstalk between microwave and d.c. lines. To minimize crosstalk on the sample between different gates we used Si/SiO<sub>2</sub> substrates <sup>2</sup> with an undoped Si layer which is not conductive at low temperatures. To control the electrochemical potential of InAs nanowire, we fabricated additional gates which are used to induce charge carriers at low temperatures, Fig. 3.6a. Before bonding, the chips with the devices are glued using non-conductive glue to the PCB board with 2 SMA connectors connected to gates 2 and 4 Fig. 3.6b. High frequency signals are combined with d.c. signals using a in-house-built low temperature bias tee.

Phase-controlled microwave bursts are generated by a vector microwave source (Agilent E2867C). Two channel outputs of arbitrary wave generator (Tektronix AWG520) are connected to the high frequency lines which are in turn connected to the two gates on the device. One of the lines is combined

---

<sup>1</sup>Designed and build by Raymond Schouten at TU Delft

<sup>2</sup>room temperature resistivity: 8,000-12,000 ohm-cm; Manufacturer NOVA:  
[www.novawafers.com](http://www.novawafers.com)



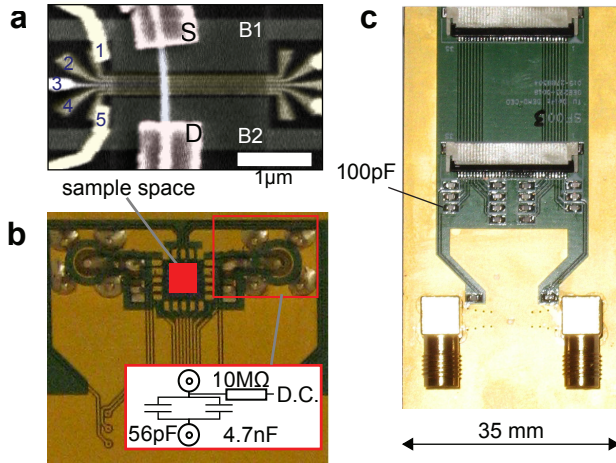


**Figure 3.6:** (a) SEM image of the modified sample design. An additional layer with two extra gates B1 and B2 is added in order to tune the electrochemical potential of the leads (marked green). Numbers 1-5 label local gates. (b) Zoom in on the part of PCB board with two bias-tees and SMA connectors. (c) PCB board. The wires enter lines on the PCB via d.c. connector. All d.c. lines on the board are fitted with a 100 pF capacitor to ground, to reduce crosstalk to the high frequency connections.

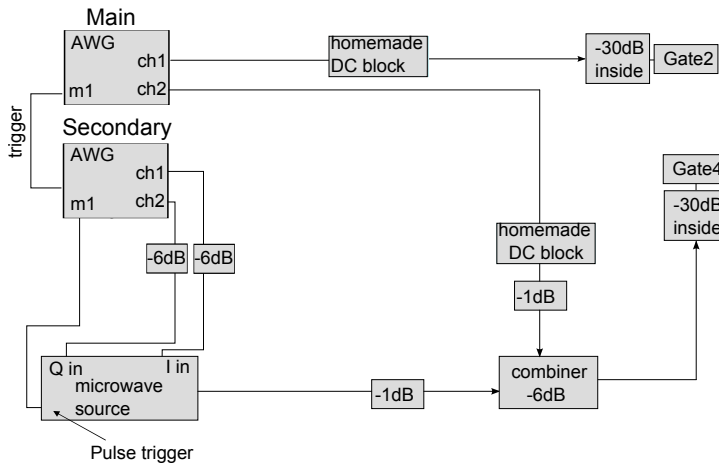


**Figure 3.7:** Block diagram of the setup used for the experiment described in chapter 7. Main arbitrary wave generator (AWG) controls voltage pulses ( $\sim 1\mu\text{s}$ ) on the gates 2 and 4 and triggers a secondary AWG. The secondary AWG is used for controlling the microwave vector source.

with the microwave output using a standard combiner (see block diagram, Fig. 3.7).

## REFERENCES

- [1] R. S. Wagner and W. Ellis, *Vapor-liquid-solid mechanism of single crystal growth*, Appl. Phys. Lett. **80**, 89 (1964).
- [2] M. T. Borgström, G. Immink, B. Ketelaars, R. Algra, and E. P. A. M. Bakkers, *Synergetic nanowire growth*, Nature Nanotech. **2**, 541 (2007).
- [3] K. A. Dick, K. Deppert, T. Mårtensson, B. Mandl, L. Samuelson, and W. Seifert, *Failure of Vapor-Liquid-Solid Mechanism in Au-Assisted MOVPE Growth of InAs Nanowires*, Nano Lett. **5**, 761 (2005).
- [4] A. I. Persson, M. W. Larsson, S. Stenström, B. J. Ohlsson, L. Samuelson, and L. R. Wallenberg, *Solid-phase diffusion mechanism for GaAs nanowire growth*, Nature Mat. **3**, 677 (2004).
- [5] L. E. Persson, A. I. Fröberg, S. Jeppesen, M. T. Björk, and L. Samuelson, *Surface diffusion effects on growth of nanowires by chemical beam epitaxy*, J Appl. Phys. **101**, 034313 (2007).
- [6] F. Glas, J.-C. Harmand, and G. Patriarche, *Why Does Wurtzite Form in Nanowires of III-V Zinc Blende Semiconductors?*, Phys. Rev. Lett. **99**, 146101 (2007).
- [7] R. E. Algra, M. A. Verheijen, M. T. Borgström, L.-F. Feiner, G. Immink, W. J. P. van Enckevort, E. Vlieg, and E. P. A. M. Bakkers, *Twinning superlattices in indium phosphide nanowires*, Nature **456**, 369 (2008).
- [8] P. Caroff, K. A. Dick, J. Johansson, M. E. Messing, K. Deppert, and L. Samuelson, *Controlled polytypic and twin-plane superlattices in III-V nanowires*, Nature Nanotech. **5**, 50 (2009).
- [9] K. Hiruma, M. Yazawa, T. Katsuyama, K. Ogawa, K. Haraguchi, M. Koguchi, and H. Kakibayashi, *Growth and optical properties of nanometer-scale GaAs and InAs whiskers*, J. Appl. Phys. **77**, 447 (1995).

- [10] E. P. A. M. Bakkers, J. A. van Dam, S. De Franceschi, L. P. Kouwenhoven, M. Kaiser, M. Verheijen, H. Wondergem, and P. van der Sluis, *Epitaxial growth of InP nanowires on germanium*, Nature **3**, 769 (2004).
- [11] P. Nguyen, H. T. Ng, T. Yamada, M. K. Smith, J. Li, J. Han, and M. Meyyappan, *Direct Integration of Metal Oxide Nanowire in Vertical Field-Effect Transistor*, Nano Lett. **4**, 651 (2004).
- [12] C. Affentauschegg and H. H. Wieder, *Properties of InAs/InAlAs heterostructures*, Semicond. Sci. Tech. **16**, 708 (2001).
- [13] C. Nguyen, K. Ensslin, and H. Kroemer, *Magneto-transport in InAs/AlSb quantum wells with large electron concentration modulation*, Surf. Sci. **267**, 549 (1992).
- [14] I. J. Gelfand, S. Amasha, D. M. Zumbühl, M. A. Kastner, C. Kadow, and A. C. Gossard, *Surface-gated quantum Hall effect in an InAs heterostructure*, Appl. Phys. Lett. **88**, 252105 (2006).
- [15] J. A. van Dam, Y. V. Nazarov, E. P. A. M. Bakkers, S. De Franceschi, and L. P. Kouwenhoven, *Supercurrent reversal in quantum dots*, Nature **442**, 667 (2006).
- [16] A. Pfund, I. Shorubalko, K. Ensslin, and R. Leturcq, *Suppression of Spin Relaxation in an InAs Nanowire Double Quantum Dot*, Phys. Rev. Lett. **99**, 036801 (2007).
- [17] C. Buizert, F. H. L. Koppens, M. Pioro-Ladrière, H.-P. Tranitz, I. T. Vink, S. Tarucha, W. Wegscheider, and L. M. K. Vandersypen, *In Situ Reduction of Charge Noise in GaAs/Al<sub>x</sub>Ga<sub>1-x</sub>As Schottky-Gated Devices*, Phys. Rev. Lett. **101**, 226603 (2008).

# 4

## ANISOTROPIC $g$ -FACTOR IN A SINGLE ELECTRON NANOWIRE QUANTUM DOT

This chapter presents transport measurements on a gate-defined single quantum dot in an InAs nanowire. The number of electrons on the dot is fully tunable, down to the last electron. Excited state spectroscopy in the Coulomb blockade regime allows us to extract the Zeeman splitting energy. When magnetic field is rotated, a change in the  $g$ -factor of a single electron spin is observed. Tuning the size of the dot *in situ* using electrostatic gates alters the amplitude of the anisotropy. The orientation of the magnetic field for which the minimum and maximum values of the  $g$ -factor are measured changes by  $6^\circ$ . The observed anisotropy is consistent with wurtzite crystal structure of InAs nanowires.

---

This chapter is in preparation for publication.

## 4.1 INTRODUCTION

Control and manipulation of single electron spins is one of the main focus points in spintronics and quantum information processing. Semiconductor quantum dots present an effective means to isolate and control a single electron spin [1]. Coherent manipulation of the Zeeman split spin states in a static magnetic field can be done using electron spin resonance (ESR) [2] achieved by applying oscillating magnetic fields. However, addressing single spins using this technique has been proven challenging [2, 3] since producing strong and localized oscillating magnetic fields is technically demanding.

Control over the Zeeman splitting via the electron  $g$ -factor would make spins selectively addressable [4]. Since the  $g$ -factor depends strongly on confinement geometry, low-dimensional structures, such as nanowires, are interesting systems for studying the  $g$ -factor [5, 6]. In InAs nanowires, the effects of system size and dimension are enhanced by strong spin-orbit interaction, which gives rise to a large electron  $g$ -factor. In addition, the wurtzite crystal symmetry in these nanowires is predicted to cause the anisotropy of the  $g$ -factor [7]. Another source of anisotropy can be asymmetric confinement of an electron in a quantum dot [8]. Control over the  $g$ -factor in multiple coupled quantum dots opens up possibilities for reading out single spins via a difference in Zeeman energy [9] or to control spins via  $g$ -tensor modulation resonance ( $g$ -TMR) [10].

This chapter presents transport measurements on a gate-defined, tunable quantum dot in an InAs nanowire. With proper design of the gate geometry we can bring the number of electrons down to zero [11]. Transport measurements allow us to directly extract the Zeeman splitting of the last electron on the dot, and measure an anisotropy of the  $g$ -factor. The measured values of the  $g$ -factor are largest for the orientation of magnetic field which is almost parallel to the nanowire axis. By adjusting the voltages that define the quantum dot we can change the size of the dot and the number of electrons *in situ*. Making quantum dot larger increases the overall Zeeman splitting and reduces the anisotropy. The direction corresponding to the largest value of  $g$ -factor changes however for only  $6^\circ$ .

## 4.2 FEW-ELECTRON QUANTUM DOT

InAs nanowires are grown in a Metal Organic Vapor Phase Epitaxy (MOVPE) chamber via the Vapor-Liquid-Solid (VLS) process [12]. The nanowires have wurtzite crystal structure and a diameter of 40-80 nm. The nanowires are deposited on an array of five 30 nm wide bottom gates, that are covered by 20 nm of  $\text{Si}_3\text{N}_4$  to isolate the gates from the nanowire [11]. This fabrication method eliminates leakage problems often observed in top gated nanowire structures, where the native InAs oxide is used as the gate dielectric (see chapter 3). In addition, it allows for very small (25-30 nm) gate spacing. This is required to be able to measure a current when the number of electrons on the dot is reduced to one. The entire structure is placed on a p-doped silicon substrate, covered with a 285 nm layer of  $\text{SiO}_2$ . We use the doped substrate as a global back gate to control the electron density in the nanowire. Source and drain contacts on the nanowire and the contacts to the bottom gates are fabricated in the last lithography step. The nanowire measured in this experiment has a diameter  $55 \pm 5$  nm. A scanning electron microscope (SEM) image of the device is shown in Fig. 4.1a.

Measurements are performed in a  $^3\text{He}$  refrigerator equipped with a 2-coil magnet. In the experiment, magnetic field can be applied in any direction in the plane of the sample. We define  $\Theta$  as the angle between the nanowire and the external magnetic field. Nanowires are n-type conducting, due to the large number of donor states at the InAs surface [13]. By applying negative voltage to the gates, a nanowire can be locally depleted. In the experiment, we apply a source-drain voltage  $V_{SD}$  on the two ends of the nanowire and measure current through a single quantum dot formed using gates 2 and 4, which are forming the tunnel barriers (see Fig. 4.1b). Typically voltages  $\sim -1$  V are sufficient to deplete the nanowire and form tunnel barrier. Gate 3 is used as a plunger *i.e* to control the number of electrons on the dot. The back gate and the outer two bottom gates, 1 and 5, are set to positive voltage ( $\sim +500$  mV) to create high electron density in the dot leads.

By sweeping gate 3 versus the source-drain bias voltage across the nanowire,  $V_{SD}$ , Coulomb blockade diamonds are mapped out, as shown in Fig. 4.2a. Inside each diamond, the electron number  $N$  on the dot is fixed. For voltages below  $\sim -200$  mV applied on gate 3, the last diamond opens up and the edges do not close anymore. We have verified that no additional diamond

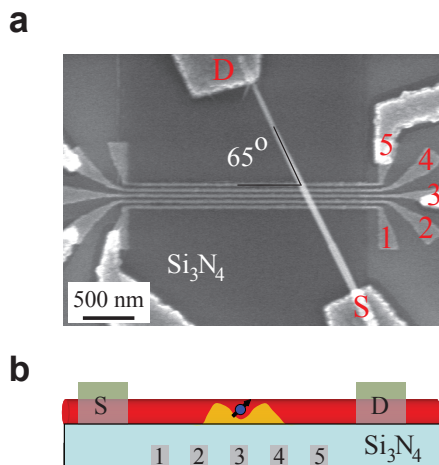


**Figure 4.1:** (a) Scanning electron microscope (SEM) image of the nanowire on top of five bottom gates. The diameter of the wire is  $55 \pm 5$  nm and it forms an angle of  $65^\circ$  with the bottom gates. (b) Schematic of the cross-section of a nanowire device with five bottom gates embedded in  $\text{Si}_3\text{N}_4$  dielectric. The quantum dot is formed using the middle three gates.

edges appear for large source-drain voltages, up to  $|V_{SD}| = 50$  meV, see Fig. 4.2a. The edges of the last diamond do not show any kinks either, which indicates that the last electron has been removed from the quantum dot [11]. For a larger number of electrons on the dot, the transparency of the barriers increases rapidly due to the larger wavefunction overlap with the leads (not shown).

From the change in current outside the Coulomb diamonds we can extract the energy of a single electron first excited orbital state,  $E_{\text{orb}} = 13.5$  meV. The smallest orbital energy corresponds to the largest confinement dimension. Based on the orbital energy the dot size can be estimated  $l_0 = \hbar / \sqrt{E_{\text{orb}} m^*} \sim 10 - 15$  nm. Here  $m^*$  is the effective mass for electrons in wurtzite InAs. Note that the effective mass in wurtzite InAs has not been measured. It is predicted to be anisotropic with values  $0.06m_e$  for momenta parallel to the nanowire axis, and  $0.042m_e$  for momenta perpendicular to the nanowire axis [14].

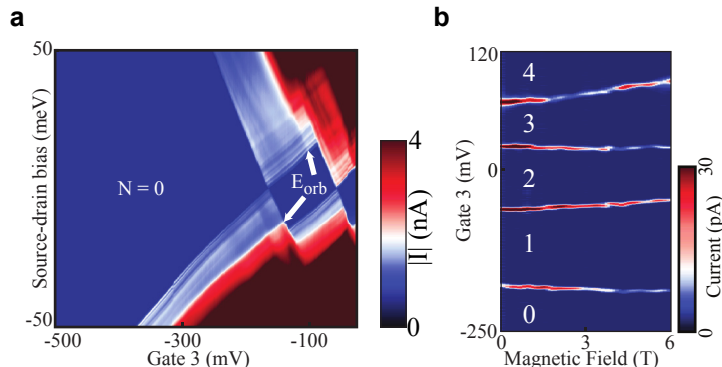


**Figure 4.2:** (a) High bias measurement of Coulomb diamonds for the last electron and empty ( $N=0$ ) quantum dot.  $E_{orb}$  indicates the first orbital excited state for  $N = 1$ . (b) Magnetic field dependence of the Coulomb peaks for the first few electrons on the dot ( $V_{SD} = 500 \mu V$ ). The angle between the nanowire axis and magnetic field is  $\Theta = 115^\circ$ .

### 4.3 ZEEMAN SPLITTING

When a magnetic field  $\mathbf{B}$  is applied, the distance between Coulomb peaks corresponding to an odd number of electrons increases linearly, as can be seen from Fig. 4.2b. The first orbitals are only twofold degenerate due to spin. From the Coulomb peaks corresponding to  $N = 0 \leftrightarrow N = 1$  and  $N = 2 \leftrightarrow N = 3$  transitions, we see a small shift related to the orbital magnetic moment of the electrons in the quantum dot [11].

We now focus on the crossing between the Coulomb diamonds for  $N = 0$  and  $N = 1$ . Fig. 4.3a shows the splitting of the orbital ground state for  $B=2.9\text{T}$  at an angle  $\Theta = 171^\circ$ . From the splitting, the Zeeman energy  $E_Z = 1.54 \pm 0.03\text{meV}$  is obtained. In addition, Fig. 4.3a shows several more resonances in the current which have similar slope as the Zeeman split line. We attribute these resonances to the states in the leads (see section 4.5 for more information). We use the difference in capacitive coupling of these lines to the bottom gates to correctly identify the Zeeman split single electron groundstate. The  $g$ -factor is  $|g| = E_Z/(\mu_B |\mathbf{B}|) = 9.1 \pm 0.2$ , where  $\mu_B$  is the Bohr magneton. The theoretical calculation predicts a negative sign of the  $g$ -factor in quantum dots in InAs [8]. Although we only measure absolute value of the  $g$ -factor throughout the chapter, the values are assumed to be negative.

Fig. 4.3b shows the extracted Zeeman energy for a single electron for



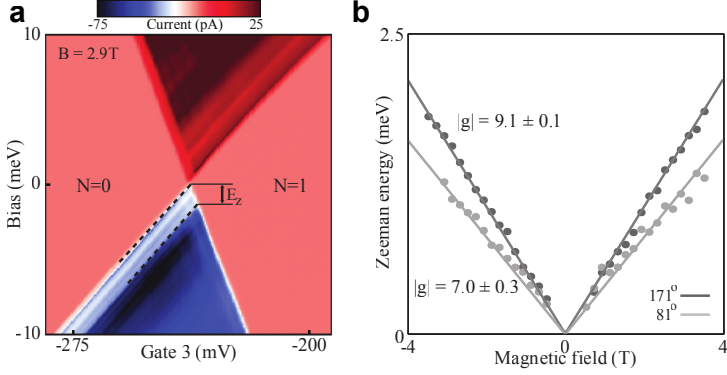


**Figure 4.3:** (a) Excited state spectroscopy is performed by measuring the current through the quantum dot. The Zeeman splitting of the  $N = 1$  groundstate,  $E_Z = 1.2\text{meV}$  at a field of  $B=2.9\text{T}$  ( $\Theta = 171^\circ$ ) can be identified as an increase in current. (b) Minimum and maximum Zeeman splitting for a single electron in a quantum dot. The Zeeman splitting is linear with magnetic field over the entire range.

different magnetic field, at  $\Theta = 171^\circ$ . The Zeeman energy increases linearly with magnetic field. From the fit, a  $g$ -factor of  $|g| = 9.1 \pm 0.1$  is obtained. When the direction of magnetic field is changed by  $90^\circ$  ( $\Theta = 81^\circ$ ), a smaller Zeeman splitting is measured, corresponding to  $|g| = 7.0 \pm 0.3$ . In the following we will discuss possible reasons for measured anisotropy.

#### 4.4 $g$ -FACTOR ANISOTROPY

There are several mechanisms that influence Zeeman splitting. Importantly, in our nanowires we can exclude the effects due to strain [15] and composition differences [10]. In wurtzite materials, the  $g$ -factor depends on the crystal direction and can be described with two  $g$ -factors: one parallel to the  $[0001]$  direction,  $g_{\parallel}$ , and one perpendicular to this direction,  $g_{\perp}$ . In nanowires used in this experiment the  $[0001]$  axis corresponds to the growth direction of the nanowire.

Analytical expressions for wurtzite  $g$ -factors can be found in Refs. [7, 8]. By comparing the contributions of the different bulk energy bands, we can understand that  $g_{\parallel} < g_{\perp}$ . Unfortunately, for InAs the band parameters for wurtzite are not known experimentally. Using theoretical values for bulk we get  $g_{\perp} = -8.1$  and  $g_{\parallel} = -13.8$ , assuming zincblende values for the momentum

matrix elements [8].

To study the dependence of the  $g$ -factor on field orientation in more detail we measure the Zeeman splitting for a full,  $360^\circ$  rotation of the magnetic field. The extracted  $g$ -factors are shown in figure 4.4a with error-bars given by the linewidth of the excited state ( $\sim 170\mu\text{eV}$ ). The extracted values of the  $g$ -factor show a strong anisotropy in field orientation with a minimum and a maximum around  $\sim 171^\circ$  and  $\sim 81^\circ$ , respectively which is  $\sim 10^\circ$  off from the nanowire axis. The fit corresponds to  $-\sqrt{(g_{max} \cos(\Theta + \phi))^2 + (g_{min} \sin(\Theta + \phi))^2}$  using  $|g_{min}| = 6.8 \pm 0.2$ ,  $|g_{max}| = 9.3 \pm 0.2$  and  $\phi = 9 \pm 2$  [16].

Note that the measured values of the  $g$ -factors are smaller than for bulk InAs (in zincblende InA  $g \approx -14.7$ , see for example [17]). This is related to the confinement in the quantum dot, which pushes the  $g$ -factor towards the free electron value of  $g_0 \approx 2$  [5, 8]. As can be seen from Figure 4.4a, the measured anisotropy direction is offset from the nanowire alignment, i.e.  $\phi \neq 0$ . This can be related to asymmetrical confinement in the quantum dot, which can also result in an anisotropic modification to the  $g$ -factor [5].

To determine the influence of confinement on the  $g$ -factor we increase the size of our quantum dot *in situ* by changing the voltage on the gates. From capacitive coupling to the gates we can see that the position of the dot has shifted to the right as can be seen from Figure 4.4c. For this tuning, we measure an orbital energy of 3.5 meV, which corresponds to dot size  $l_{dot} \approx 20$  nm. The number of electrons in the quantum dot of this size could not be reduced to zero before the tunnel barriers become too opaque to measure any current. We estimate the number of electrons on the dot to be  $\lesssim 15$ . The  $g$ -factor as a function of  $\Theta$  is plotted in Figure 4.4b. From the fit we get  $|g_{min}| = 8.1 \pm 0.2$ ,  $|g_{max}| = 9.8 \pm 0.2$  and  $\phi = 3 \pm 2^\circ$ . The absolute values of  $g$ -factors in Fig. 4.4b are smaller compared to the values in Fig. 4.4a. This supports the conclusion that the overall size of the  $g$ -factor is related to the strength of the quantum dot confinement [18]. Importantly, the angles for the minimum and the maximum Zeeman splitting change only by  $6^\circ$  for the two quantum dot configurations. This indicates that the anisotropy of the  $g$ -factor is not dominated by the microscopic differences in the confinement potential.

In conclusion, we have studied anisotropy of  $g$ -factor in electrostatically defined quantum dots in InAs nanowires containing few electrons. The Zeeman splitting of a single spin in such a quantum dot is determined. We observed a large anisotropy in the  $g$ -factor, which is consistent with the anisotropy

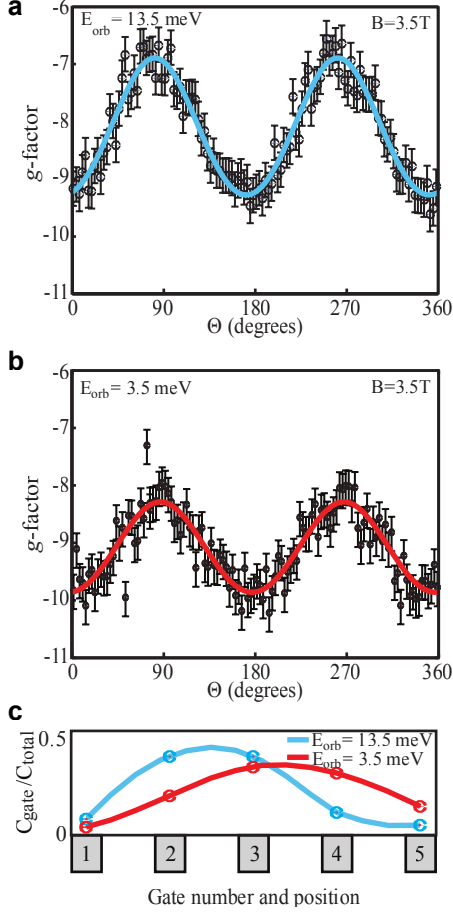


**Figure 4.4:** (a,b) Anisotropy of the  $g$ -factor measured at  $|\mathbf{B}|=3.5$  T for the small (a) and large (b) dot. Line fits are  $-\sqrt{(g_{\text{max}} \cos(\Theta + \phi))^2 + (g_{\text{min}} \sin(\Theta + \phi))^2}$ . (c) Capacitances between the dot and individual bottom gates  $C_{\text{gate}}$  which are normalized with the total capacitance of the gates,  $C_{\text{total}}$ , for the small dot (blue) and large dot (red). The line connecting the data-points serves as a guide to the eye.

predicted for the wurtzite crystal symmetry. By tuning *in situ* the size and position of the quantum dot we can change the  $g$ -factor. The dependence of the  $g$ -factor on the quantum dot shape provides an alternative means to address spin states in single or double quantum dots and to manipulate them

using their difference in Zeeman energy.

## 4.5 ADDITIONAL INFORMATION

Multiple conductance resonances parallel to the edge of the Coulomb diamond are sometimes observed. Although resonances in the conductance can be expected for excited states of the quantum dot, they can have other origins and do not necessarily correspond to dot states [19]. Fig. 4.5a shows the conductance through the dot in a magnified section around the  $N = 0$  to  $N = 1$ . Several of these lines end in the zero electron diamond, where there can be no excited states [20]. For nanowires, attempts have been made to explain these lines [11, 21], but they have never been identified conclusively. Due to presence of these line, it is difficult to identify excited states of the quantum dot.

The difference in capacitive coupling of the bottom gates to the quantum dot can be used to discriminate between states that correspond to the dot and states that have a different origin. The tunnel barriers of the dot are tuned to be asymmetric. States that are aligned with the incoming barrier are now sharply defined with a width limited by the electron temperature in the device. States aligned with the outgoing barrier are broadened due to an enhanced wavefunction overlap with the lead. This gives rise to lines that run parallel to only one of the diamond edges, as is shown in Fig. 4.5b.

Sweeping the voltage on gate 3, while applying an appropriate voltage to an outer gate, gate 1 or gate 5, we measure the current at a fixed cross-section through the diamond edge, as indicated in Fig. 4.5b. The point from which the ground state of the quantum dot enters the bias window will now remain roughly fixed in gate space. States that do not belong to the dot have a different capacitive coupling and will move with a finite slope, while excited states of the dot will remain parallel to the ground state.

In Fig. 4.5c the dependence of the resonances can be seen as a function of gate 1 and 3. Only one line can be found that has the same capacitive coupling to the gates as the ground state. We identify this as the point where the chemical potential for the excited state of an electron enters the bias window  $\mu_{SD}$ . From the difference in applied bias we can directly find the excited state energy,  $\Delta V_{SD} = \alpha E$ , where  $\alpha$  converts the measured bias difference into energy by taking into account for the capacitive coupling of the leads to the

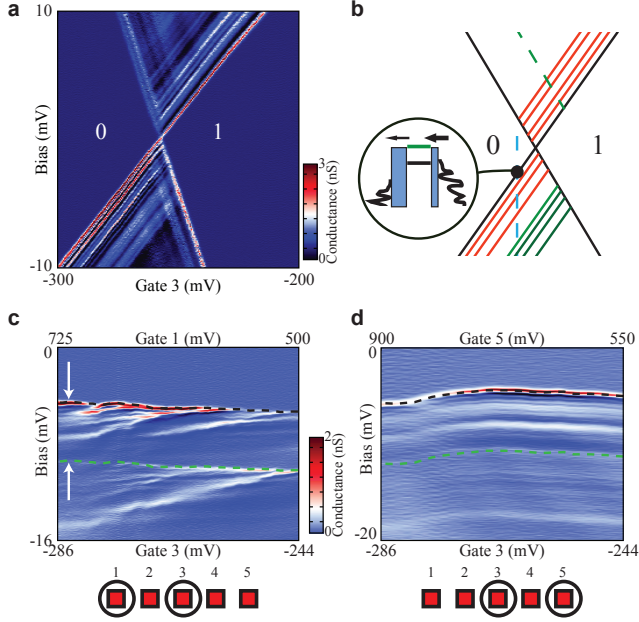


**Figure 4.5:** (a) Conductance through the quantum dot at the crossing between the Coulomb diamonds for  $N = 0$  and  $N = 1$ . Multiple lines can be seen that run parallel to the ground state of the dot. A number of lines end in the  $N = 0$  diamond. (b) Schematic diagram of the conductance plot in (a). Red lines correspond to transitions via the ground state, green via the excited state. Inset shows the asymmetric tuning of the tunnel barriers at the cut through the diamond. (c,d) Different cuts through the diamond at the  $N = 0 \leftrightarrow 1$  while sweeping two gates simultaneously. In (c), gate 1 is swept simultaneously with 3 and in (d), gate 5 is swept simultaneously with 3. In (c) the resonances have different slopes, corresponding to different capacitive couplings. In (d) the couplings are approximately equal. From the coupling of the lines the Zeeman splitting between the first electron ground state and the spin excited state at  $B = 8$  T can be deduced. The bottom row diagrams show the different gates. The encircled ones were swept in the measurement.

dot. From the slope of the lines that do not correspond to a dot excited state we can infer that they couple more strongly to gate 1 than to gate 3.

In Fig. 4.5d the voltages on gate 3 and 5 are changed. All lines are parallel to the ground state, indicating that their capacitive coupling is the same. By comparing Fig. 4.5c and 4.5d, we conclude that the lines that we see correspond to states in the left lead of the quantum dot. We have confirmed that by

reversing the asymmetry of the tunnel barriers the resonance lines couple more strongly to gate 5 instead of 1. As expected for this barrier asymmetry, for negative bias no line can be found that runs parallel to the ground state.

From the differences in capacitive coupling we can understand that the lines in figure 4.5a are due to states in the lead that result in an increased tunnel probability. When the bias over the dot is increased, the current through the dot shows an increase whenever a resonance in the density of states in the lead enters the bias window. Therefore, the resonances will precisely reflect this density of states. For each excited state in the dot, a copy of these resonances can be seen. At larger bias window, multiple states can contribute to transport and resonances may overlap.

Interestingly, these lead resonances are strongly dependent on both magnetic field strength and orientation and on the gate voltages that define the dot. Based on this, we conclude that they correspond to a modulation in the density of states in the leads due to localization. This is in line with the relatively short mean free path for InAs nanowires (50-100 nm), which is of the same order as our nanowire diameter  $\sim 60 - 80$  nm and much smaller than the length of the semiconductor part of nanowire leads ( $\sim 1 \mu\text{m}$ ). In fact, these lines are suppressed in a semiconductor systems with longer electron mean free path [1] or when the leads of the dot are metallic [22].

This work has been performed in collaboration with Juriaan W. W. van Tilburg, Sergey M. Frolov, Moïra Hocoëvar, Erik P. A. M. Bakkers and Leo P. Kouwenhoven.

## REFERENCES

- [1] R. Hanson, L. P. Kouwenhoven, J. R. Petta, S. Tarucha, and L. M. K. Vandersypen, *Spins in few-electron quantum dots*, Rev. Mod. Phys. **79**, 1217 (2007).
- [2] F. H. L. Koppens, C. Buizert, K.-J. Tielrooij, I. T. Vink, K. C. Nowack, L. P. Meunier, T. Kouwenhoven, and L. M. K. Vandersypen, *Driven coherent oscillations of a single electron spin in a quantum dot*, Nature **442**, 776 (2006).
- [3] M. Xiao, I. Martin, E. Yablonovitch, and H. W. Jiang, *Electrical detection*

- of the spin resonance of a single electron in a silicon field-effect transistor*, Nature **430**, 435 (2004).
- [4] R. Vrijen, E. Yablonovitch, K. Wang, H. W. Jiang, A. Balandin, V. Roychowdhury, T. Mor, and D. DiVincenzo, *Electron-spin-resonance transistors for quantum computing in silicon-germanium heterostructures*, Phys. Rev. A **62**, 012306 (2000).
- [5] A. A. Kiselev, E. L. Ivchenko, and U. Rössler, *Electron  $g$  factor in one- and zero-dimensional semiconductor nanostructures*, Phys. Rev. B **58**, 16353 (1998).
- [6] M. T. Björk, A. Fuhrer, A. E. Hansen, M. W. Larsson, L. E. Fröberg, and L. Samuelson, *Tunable effective  $g$  factor in InAs nanowire quantum dots*, Phys. Rev. B **72**, 201307 (2005).
- [7] C. Hermann and C. Weisbuch,  *$\vec{k}\cdot\vec{p}$  perturbation theory in III-V compounds and alloys: a reexamination*, Phys. Rev. B **15**, 823 (1977).
- [8] A. De and C. E. Pryor, *Calculation of Landé  $g$  factors for III-V nanowhisker quantum dots and comparison with experiment*, Phys. Rev. B **76**, 155321 (2007).
- [9] H.-A. Engel and D. Loss, *Single-spin dynamics and decoherence in a quantum dot via charge transport*, Phys. Rev. B **65**, 195321 (2002).
- [10] Y. Kato, R. C. Myers, D. C. Driscoll, A. C. Gossard, J. Levy, and D. D. Awschalom, *Gigahertz Electron Spin Manipulation Using Voltage-Controlled  $g$ -Tensor Modulation*, Science **299**, 1201 (2003).
- [11] C. Fasth, A. Fuhrer, L. Samuelson, V. N. Golovach, and D. Loss, *Direct Measurement of the Spin-Orbit Interaction in a Two-Electron InAs Nanowire Quantum Dot*, Phys. Rev. Lett. **98**, 266801 (2007).
- [12] R. S. Wagner and W. Ellis, *Vapor-liquid-solid mechanism of single crystal growth*, Appl. Phys. Lett. **80**, 89 (1964).
- [13] S. A. Dayeh, E. T. Yu, and D. Wang, *Transport Coefficients of InAs Nanowires as a function of Diameter*, Small **5**, 77 (2009).

- 
- [14] A. De and C. E. Pryor, *Predicted band structures of III-V semiconductors in the wurtzite phase*, Phys. Rev. B **81**, 155210 (2010).
- [15] T. Nakaoka, T. Saito, J. Tatebayashi, S. Hirose, T. Usuki, N. Yokoyama, and Y. Arakawa, *Tuning of g-factor in self-assembled In(Ga)As quantum dots through strain engineering*, Phys. Rev. B **71**, 205301 (2005).
- [16] T. P. Mayer Alegre, F. G. G. Hernández, A. L. C. Pereira, and G. Medeiros-Ribeiro, *Landé g Tensor in Semiconductor Nanostructures*, Phys. Rev. Lett. **97**, 236402 (2006).
- [17] J. Konopka, *Conduction electron spin resonance in InAs*, Physics Letters A **26**, 29 (1967).
- [18] C. E. Pryor and M. E. Flatté, *Landé g Factors and Orbital Momentum Quenching in Semiconductor Quantum Dots*, Phys. Rev. Lett. **96**, 026804 (2006).
- [19] C. C. Escott, F. A. Zwanenburg, and A. Morello, *Resonant tunnelling features in quantum dots*, Nanotechnology **21**, 274018 (2010).
- [20] L. P. Kouwenhoven, D. G. Austing, and S. Tarucha, *Few-electron quantum dots*, Rep. Prog. Phys. **64**, 701 (2001).
- [21] M. Möttönen, K. Y. Tan, K. W. Chan, F. A. Zwanenburg, W. H. Lim, C. C. Escott, J.-M. Pirkkalainen, A. Morello, C. Yang, J. A. van Donkelaar, et al., *Probe and control of the reservoir density of states in single-electron devices*, Phys. Rev. B **81**, 161304 (2010).
- [22] T. S. Jespersen, M. Aagesen, C. Sørensen, P. E. Lindelof, and J. Nygård, *Kondo physics in tunable semiconductor nanowire quantum dots*, Phys. Rev. B **74**, 233304 (2006).





# 5

## DISENTANGLING THE EFFECTS OF SPIN-ORBIT AND HYPERFINE INTERACTIONS ON SPIN BLOCKADE

We have achieved the few-electron regime in InAs nanowire double quantum dots. Spin blockade is observed for the first two half-filled orbitals, where the transport cycle is interrupted by forbidden transitions between triplet and singlet states. Partial lifting of spin blockade is explained by spin-orbit and hyperfine mechanisms that enable triplet to singlet transitions. The measurements over a wide range of interdot coupling and tunneling rates to the leads are well reproduced by a simple transport model. This allows us to separate and quantify the contributions of the spin-orbit and hyperfine interactions.

---

This chapter has been published in *Phys. Rev. B* **81**, 201305(2010).

## 5.1 INTRODUCTION

Spins in semiconductor quantum dots are possible building blocks for quantum information processing [1]. The ultimate control of spin states is achieved in electrically defined single and double quantum dots [2]. Many semiconductors that host such dots exhibit strong spin-orbit and hyperfine interactions. On the one hand, these interactions provide means of coherent spin control [3, 4]. On the other hand, they mix spin states. In double quantum dots, mixing of singlet and triplet states weakens spin blockade [5–9], which is a crucial effect for spin qubit operation [10, 11]. Spin mixing due to hyperfine interaction was studied in GaAs double quantum dots, where spin-orbit coupling was weak [5, 6, 12]. In InAs, besides the hyperfine interaction, also spin-orbit interaction has a considerable effect on spin blockade. Previous measurement on many electron double dots in InAs nanowires demonstrated that spin blockade is lifted by both interactions [7, 8]. However, the effects of these two interactions could not be separated. As a consequence, the exact determination of the spin-orbit mechanism was lacking.

In this chapter, we establish the individual roles of spin-orbit and hyperfine interactions in the spin-blockade regime. Spin blockade is observed in tunable gate-defined few-electron double quantum dots in InAs nanowires. In the few-electron regime, the quantum states involved in transport can be reliably identified and the effects from excess electrons in the dots can be ruled out. This enables a careful comparison to theory which includes random nuclear magnetic fields as well as spin-orbit mediated tunneling between triplets and singlets [13]. The effects of the two interactions are traced in three distinct transport regimes, determined by the interdot coupling and the tunneling rates to the leads. The regimes are observed in two few-electron nanowire devices, results from one of them are discussed in this chapter.

## 5.2 SPIN BLOCKADE

The nanowire devices are fabricated on pre-patterned substrates, following Ref. [14] (Fig. 5.1, upper inset). The substrates are patterned with narrow metallic gates which are covered with a 20 nm layer of  $\text{Si}_3\text{N}_4$  dielectric to suppress gate leakage [15]. Single-crystalline InAs nanowires with diameters from 40-80 nm are deposited randomly on the substrate. Conveniently aligned

wires are contacted by source and drain electrodes. Simultaneously, contacts are made to the gates underneath the wire. Measurements are performed at  $T = 250$  mK in magnetic field applied perpendicular to the substrate.

The few-electron double quantum dot is formed by gates 1-4. Such tuning ensures that both dots can be emptied before the barriers become too opaque for detecting current. Gates 1 and 4 define the outer barriers, gates 2 and 3 control the interdot coupling. The charge stability diagram of a double dot is obtained by sweeping gates 2 and 3 and monitoring the source-drain current (Fig. 5.1). The empty (0,0) state is verified by Coulomb blockade measurements: no lower charge states are observed in either dot up to  $V_{SD} = 70$  mV (see also chapter 4). Large charging and orbital energies extracted from the last Coulomb diamond also support the few electron regime ( $E_c \approx 14$  meV,  $E_{orb} \approx 9$  meV) [14]. In both dots the energy to add a third electron ( $E_c + E_{orb}$ ) is higher than the energy to add the second or the fourth ( $E_c$ ), see Fig. 5.1. This indicates that the first few orbitals are doubly-degenerate due to spin.

The spin states of the double dot are probed through spin blockade. A transition is spin-blocked when it is energetically allowed, but forbidden by spin conservation [16]. Current can flow through a double dot via a cycle of charge states. For example the cycle  $(0,1) \rightarrow (1,1) \rightarrow (0,2) \rightarrow (0,1)$  transfers one electron from left to right (Fig. 5.2a). The transition  $(1,1) \rightarrow (0,2)$  is forbidden when the (1,1) state is a triplet and the only accessible (0,2) state is a singlet. Therefore, spin blockade suppresses the current at this charge cycle. We observe spin blockade at several charge cycles that involve (odd, odd)  $\rightarrow$  (even, even) transitions for the first few electrons (Fig. 5.1, lower inset), as expected from simple spin filling [17].

### 5.3 SUPPRESSION OF SPIN BLOCKADE

An incomplete spin blockade results in finite current through the double dot. This current is due to processes that enable transitions out of triplet (1,1) states (dashes in Fig. 5.2a). It was established in experiments on GaAs dots that hyperfine mixing results in transitions between different (1,1) states [5, 6, 12]. Ref. [13] predicts that spin-orbit interaction can also lift spin blockade by hybridizing triplet (1,1) states with S(0,2). Below we describe how the contributions of the two interactions can be disentangled.

Flip-flops involving the fluctuating nuclear spin bath mix the (1,1) electron

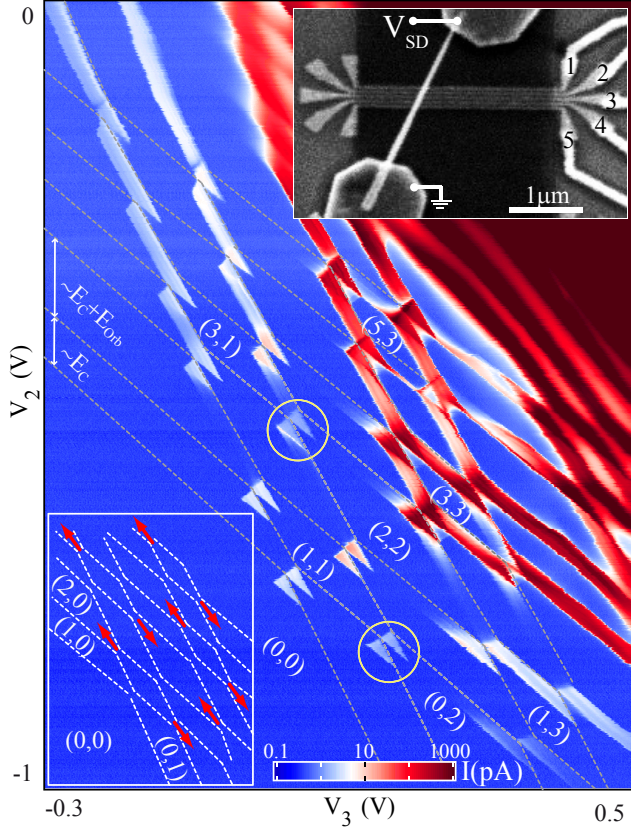


**Figure 5.1:** Few-electron double dot charge stability diagram for  $V_{SD} = 4$  mV and  $B = 0$ . The numbers in brackets correspond to the charges on the left and the right dots. Dashed lines separate the charge states. The energy required to add an extra electron is proportional to the spacing between the lines:  $\Delta E_L = 0.14e\Delta V_2$ ,  $\Delta E_R = 0.12e\Delta V_3$ . The encircled regions are investigated in Fig. 5.2. Upper inset: scanning electron micrograph of a nanowire device. Ti/Au gates with a pitch of 60 nm are labeled 1-5. The black stripe is a layer of  $\text{Si}_3\text{N}_4$ . Lower inset: Arrows pointing up/down correspond to the transitions at which spin blockade is observed for positive/negative bias.

spin states only if they are close in energy. The characteristic energy scale over which the hyperfine interaction is effective is  $E_N = AI/\sqrt{N}$  [18], where  $A$  is the hyperfine constant,  $N$  is the number of nuclei in the dot and  $I$  is the average nuclear spin. The corresponding r.m.s. of nuclear field fluctuations is

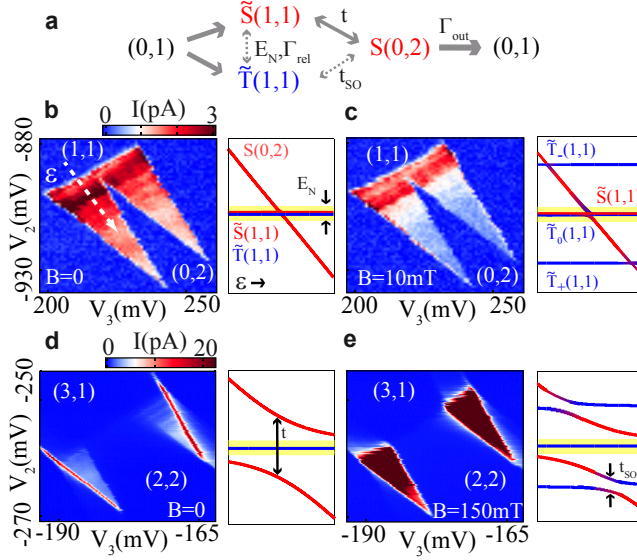


**Figure 5.2:** (a) Transport diagram through a spin-blocked charge cycle at small detuning, with the relevant transition rates. (b), (c):  $(1,1) \rightarrow (0,2)$  tuned to weak interdot coupling for  $B = 0$  and  $B = 10$  mT,  $V_{SD} = 5$  mV. (d), (e):  $(3,1) \rightarrow (2,2)$  tuned to strong interdot coupling for  $B = 0$  and  $B = 150$  mT,  $V_{SD} = 1.3$  mV. Energy levels of  $(1,1)$  and  $(0,2)$  states are calculated for the regimes in (b)-(e). The dashed line in (b) indicates a cut along the detuning axis,  $\varepsilon$ .

given by  $B_N = E_N/g\mu_B$ . (We measured the Landé g-factor  $g = 8.3 \pm 0.6$  by excited state spectroscopy.)

Due to spin-orbit interaction the  $(1,1)$  eigenstates become superpositions of spin triplets and the  $(1,1)$  singlet. We denote these  $(1,1)$  eigenstates with  $\tilde{T}_-$ ,  $\tilde{T}_0$ ,  $\tilde{T}_+$  and  $\tilde{S}$ . The spin singlet admixture in  $\tilde{T}$  states is of the same order as the ratio of the dot size to the spin-orbit length  $l_{dot}/l_{SO}$ . Because they contain a singlet component,  $\tilde{T}$  states are coupled to  $S(0,2)$ , which remains a spin singlet since both electrons in it belong to the same orbital. The exact coupling between  $\tilde{T}(1,1)$  and  $S(0,2)$  depends on the microscopic properties of the spin-orbit interaction in InAs nanowires and on the details of confinement [19]. Here we simply parametrize this coupling with  $t_{SO} \sim (l_{dot}/l_{SO})t$ , where  $t$  is the tunnel coupling between  $S(1,1)$  and  $S(0,2)$ .

The energy levels calculated for weakly and strongly coupled double dots

are shown in Figs. 5.2b-e as a function of the energy detuning  $\varepsilon$  between the (1,1) and (0,2) states. The calculation of the levels includes  $t_{SO}$  while disregarding the effect of nuclear spins. The effect of  $E_N$  is represented by a gray stripe: the (1,1) states within the stripe are mixed by the nuclei.

The principal roles of spin-orbit and hyperfine interactions can be illustrated by tuning the interdot tunnel coupling (Fig. 5.2). For small  $t, t_{SO} \ll E_N$ , the hyperfine-induced spin mixing dominates. The energy levels appear the same as for real spin singlets and triplets (Figs. 5.2b and 5.2c) [2]. In this limit the current is high at zero magnetic field, but is suppressed by a small magnetic field. This occurs for fields  $B \gtrsim B_N$  when the hyperfine mixing of the split-off states  $\tilde{T}_+$  and  $\tilde{T}_-$  with the decaying (1,1) state is reduced.

The energy levels become noticeably modified when  $t_{SO} \propto t$  is large (Fig. 5.2d and 5.2e). But the effect of this modification can only be seen at finite magnetic field. At zero field only one of the four (1,1) states is coupled to S(0,2) by the strength  $t$  (Fig. 5.2d). The hyperfine mechanism cannot facilitate the escape from the uncoupled states because of the large singlet anticrossing, so the current is suppressed [5]. At finite field, however, the eigenstates  $\tilde{T}_+$  and  $\tilde{T}_-$  are coupled to the singlet S(0,2) by a large  $t_{SO}$  and the current increases (Fig. 5.2e). The current at finite field is limited by the escape rate from the remaining one blocked state.

In a nutshell, hyperfine interaction lifts spin blockade for weak coupling and small fields, spin-orbit interaction - for strong coupling and large fields. The current may exhibit either a hyperfine-induced peak at zero magnetic field, or a dip due to spin-orbit interaction. The interplay of the two contributions gives rise to three distinct regimes as shown in Fig. 5.3. In the first regime, for weakest coupling, a zero field peak is observed for any detuning (Fig. 5.3a). In the intermediate regime, a dip around zero detuning becomes a peak at higher detuning. For the strongest coupling, the current only shows a dip at zero field (Fig. 5.3c). In all regimes the high-detuning behavior extends up to  $\varepsilon = 5 - 7$  meV, where the (1,1) states are aligned with  $\tilde{T}(0,2)$  and spin blockade is lifted. The three regimes were observed at several spin-blockaded transport cycles, here we show the data from two of them (circles in Fig. 5.1).

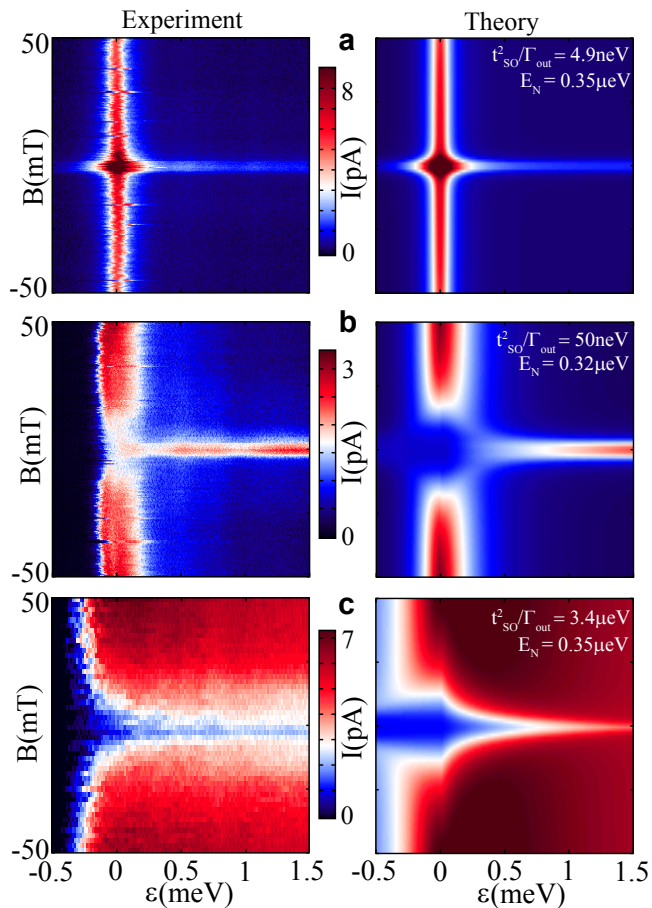


**Figure 5.3:** (Left) Measured double dot current as a function of detuning and magnetic field. (Right) Simulations of current for different values of  $t_{SO}^2/\Gamma_{out}$  averaged over  $N_f = 1000$  random nuclear configurations. (a) and (b) data from  $(1, 1) \rightarrow (0, 2)$  transition, (c) data from  $(1, 3) \rightarrow (2, 2)$  to illustrate large  $\Gamma_{rel}$  and  $\Gamma_{inel}$  (see Fig. 5.4). Simulation parameters: (a)  $\Gamma_{out} = 100 \mu\text{eV}$ ,  $t = 6.6 \mu\text{eV}$ ,  $t_{SO} = 0.7 \mu\text{eV}$ ,  $\Gamma_{rel} = 0$ ; (b)  $\Gamma_{out} = 70 \mu\text{eV}$ ,  $t = 32 \mu\text{eV}$ ,  $t_{SO} = 1.8 \mu\text{eV}$ ,  $\Gamma_{rel} = 0.2 \text{ MHz}$ ; (c)  $\Gamma_{out} = 20 \mu\text{eV}$ ,  $t = 45 \mu\text{eV}$ ,  $t_{SO} = 8.2 \mu\text{eV}$ ,  $\Gamma_{rel} = 5.4 \text{ MHz}$ ;

## 5.4 COMPARISON WITH A TRANSPORT MODEL

The data are in good agreement with our simple transport theory that accounts for spin-orbit and hyperfine interaction [13]. The three regimes are



distinguished by the rate  $t_{SO}^2/\Gamma_{out}$ , where  $\Gamma_{out}$  is the rate of escape from the S(0,2) into the outgoing lead (in  $\mu\text{eV}$ ). Intuitively,  $t_{SO}^2/\Gamma_{out}$  is the  $\tilde{T}(1,1)$  escape rate due to  $t_{SO}$ . When  $t_{SO}^2/\Gamma_{out} \ll E_N$  hyperfine mixing is the most effective process in lifting the spin blockade, see Fig. 5.2a. This is the case in Fig. 5.3a, where we observe a zero-field peak in the current. As  $t_{SO}^2/\Gamma_{out}$  is increased, we observe intermediate regime (Fig. 5.3b). Still, zero field peak persists at large detuning since  $t_{SO}^2/\Gamma_{out}$  becomes suppressed  $\propto 1/\varepsilon^2$  due to a reduced overlap of the (1,1) states with S(0,2). Around zero detuning, however, the hyperfine mixing at small fields is weaker than the spin-orbit coupling at finite fields, leading to a zero-field dip. In the third regime, for even higher  $t_{SO}^2/\Gamma_{out} \gg E_N$ , the zero-field dip is extended to high positive detuning (Fig. 5.3c). It should be stressed that the effects of both hyperfine and spin-orbit interactions are observed in all three regimes: current at higher fields is always enabled by spin-orbit interaction, and around zero magnetic field current is in part due to hyperfine mixing even for  $t_{SO}^2/\Gamma_{out} > E_N$ .

The peaks, dips and their widths, as well as the current levels are reproduced by a numerical simulation of transport through the spin-orbit eigenstates. The double dot current is obtained from stationary solutions of master equations [13]. Spin mixing due to hyperfine interaction is included by averaging over thousands of random nuclear fields. While the original model of Ref. [13] considered only elastic tunneling, here current at high positive detuning is modeled by the inelastic transition rate,  $\Gamma_{inel} = t^2 f(\varepsilon)$  from S(1,1) and  $\Gamma_{inel} = t_{SO}^2 f(\varepsilon)$  from  $\tilde{T}(1,1)$  states. The function  $f(\varepsilon)$  reflects the phonon density of states in the nanowire. We determine this function by matching the inelastic current in each regime. The inclusion of  $\Gamma_{inel}$  makes it possible to closely match the magnetic field evolution of the detuning cuts (Fig. 5.3, right column). All three regimes are reproduced with  $t_{SO} = (0.12 \pm 0.07)t$  and  $E_N = 0.33 \pm 0.05 \mu\text{eV}$ . The spin-orbit length  $l_{SO} \approx (t/t_{SO})l_{dot} = 250 \pm 150 \text{ nm}$  can be estimated using  $l_{dot} = \hbar/\sqrt{E_{orb}m_{eff}} \approx 20 \text{ nm}$  ( $m_{eff} = 0.023m_e$  in InAs). The values for  $E_N$  are in agreement with the  $N = 10^6$  nuclei estimated from the dot size and  $AI \approx 350 \mu\text{eV}$ . The values for  $l_{SO}$  and  $E_N$  are as expected for InAs nanowires quantum dots [7, 14].

We now turn to more quantitative analysis. The model is especially successful in reproducing the data in Fig. 5.3a, where  $t_{SO}^2/\Gamma_{out} \ll E_N$ . In Figures 5.4a and 5.4b the linecuts along magnetic field and detuning are fitted using the same set of model parameters. The model allows to trace the influences

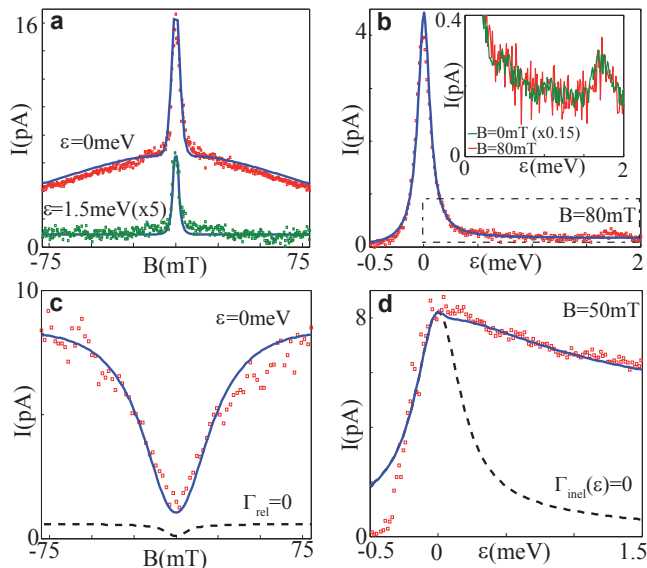


**Figure 5.4:** (a),(b) Linecuts from Fig. 5.3a. The traces at  $\varepsilon = 1.5$  meV and  $B = 0$  mT are scaled by factors of 5 and 0.15 respectively. Dashed area in (b) is shown in the inset. (c),(d) Linecuts from Fig. 5.3c and fits to the model for various  $\Gamma_{rel}$  and  $\Gamma_{inel}$ . In the entire figure solid lines are simulations using parameters from Fig. 5.3 averaged over  $N_f = 30000$  (a) and  $N_f = 5000$  (b)-(d) random nuclear configurations.

of spin-orbit and hyperfine interactions through various features of the data. The narrow peak at zero field is mainly due to hyperfine mixing (Fig. 5.4a), similar to that observed in GaAs dots [5, 6, 12]. However, the wider Lorentzian background at zero detuning is due to the strong spin-orbit coupling in InAs nanowires. The elastic current drops for  $B \gtrsim \Gamma_{out}/2g\mu_B \approx 100$  mT, where the detuning between  $\tilde{T}_{\pm}(1,1)$  exceeds the level broadening of S(0,2) set by  $\Gamma_{out}$ .

The current is suppressed in the inelastic regime, that is for detuning  $\varepsilon \gtrsim \Gamma_{out}$  (Fig. 5.4b). The remaining current, however, conveys information about the strength of spin-orbit interaction. At zero magnetic field the current is limited by the singlet tunneling  $\sim t$ , which is weak in this regime. At higher field the slowest process is the tunneling from  $\tilde{T}_{\pm}$  states with a rate limited by  $t_{SO}$ , which is even weaker. The model [13] predicts a simple relation  $I(B = 0)/I(B \gg B_N) = t^2/12t_{SO}^2$ . The inset to Fig. 5.4b shows that the current at zero field scales to the current at finite field. From the ratio we determine

$t_{SO} = (0.11 \pm 0.02)t$  for this regime.

The model helps identify another spin relaxation mechanism present in some of the data, such as shown in Figs. 5.3c and 5.4c. A zero-field dip in the elastic current is reproduced by including the hyperfine mixing and the spin-orbit hybridization. However, the predicted current is much lower than in the experiment (dashed line in Fig. 5.4c). This discrepancy can be reconciled by introducing a field-independent rate of spin relaxation  $\Gamma_{rel} \approx 6$  MHz which mixes all (1,1) states [13]. This spin relaxation may be induced by electron-nuclear flip-flops mediated by phonons [20], spin-spin interactions mediated by charge fluctuations and spin-orbit interaction [21, 22] or by virtual processes such as cotunneling or spin exchange with the leads. The magnitude of  $\Gamma_{rel}$  depends on the gate settings, and is not directly related to the magnitudes of  $t$  or  $\Gamma_{out}$ .

In this regime we also observe a large inelastic current (Fig. 5.3c), which implies a high inelastic rate  $\Gamma_{inel}$ . Figure 5.4d shows the contribution of inelastic current compared to the expected elastic current. Some peculiarities of the data in Figs. 5.3b and 5.3c are not captured by the model. The current onset is unexpectedly sharp as the detuning is increased (Figs. 5.3b-d). A possible reason for this discrepancy could be dynamic nuclear polarization not included in our model. It is known that dynamic nuclear polarizations can cause sharp current switches [7, 23]. Another explanation is that a sharp inelastic resonance at small detuning enhances the current [24]. In conclusion, we separate the effects of spin-orbit and hyperfine interactions in the spin-blockade regime of a double quantum dot. These findings will guide the development of spin-orbit controlled qubits. Further insights into spin-orbit interaction in nanowires can be obtained from direct measurements of spin coherence times.

This work has been done in collaboration with S. M. Frolov, J. W. W. van Tilburg, J. Danon, Yu. V. Nazarov, R. Algra, E. P. A. M. Bakkers and L. P. Kouwenhoven.

We thank M. Triff, D. Loss, K.C. Nowack, L.M.K. Vandersypen and M.C. van der Krogt for their help. This work has been supported by NWO/FOM (Netherlands Organization for Scientific Research) and through the DARPA program QUEST.

---

**REFERENCES**

- [1] D. Loss and D. P. DiVincenzo, *Quantum computation with quantum dots*, Phys. Rev. A **57**, 120 (1998).
- [2] R. Hanson, L. P. Kouwenhoven, J. R. Petta, S. Tarucha, and L. M. K. Vandersypen, *Spins in few-electron quantum dots*, Rev. Mod. Phys. **79**, 1217 (2007).
- [3] K. C. Nowack, F. H. L. Koppens, Y. V. Nazarov, and L. M. K. Vandersypen, *Coherent Control of a Single Electron Spin with Electric Fields*, Science **318**, 1430 (2007).
- [4] S. Foletti, H. Bluhm, D. Mahalu, V. Umansky, and A. Yacoby, *Universal quantum control of two-electron spin quantum bits using dynamic nuclear polarization*, Nature Phys. **5**, 903 (2009).
- [5] F. H. L. Koppens, J. A. Folk, J. M. Elzerman, R. Hanson, L. H. Willems van Beveren, I. T. Vink, H.-P. Tranitz, W. Wegscheider, L. P. Kouwenhoven, and L. M. K. Vandersypen, *Control and Detection of Singlet-Triplet Mixing in a Random Nuclear Field*, Science **309**, 1246 (2005).
- [6] A. C. Johnson, J. R. Petta, J. M. Taylor, A. Yacoby, M. D. Lukin, C. M. Marcus, M. P. Hanson, and A. C. Gossard, *Triplet-singlet spin relaxation via nuclei in a double quantum dot*, Nature **435**, 925 (2005).
- [7] A. Pfund, I. Shorubalko, K. Ensslin, and R. Leturcq, *Suppression of Spin Relaxation in an InAs Nanowire Double Quantum Dot*, Phys. Rev. Lett. **99**, 036801 (2007).
- [8] A. Pfund, I. Shorubalko, K. Ensslin, and R. Leturcq, *Spin-state mixing in InAs double quantum dots*, Phys. Rev. B **76**, 161308 (2007).
- [9] H. O. H. Churchill, A. J. Bestwick, J. W. Harlow, F. Kuemmeth, D. Marcos, C. H. Stwertka, S. K. Watson, and C. M. Marcus, *Electron-nuclear interaction in  $^{13}\text{C}$  nanotube double quantum dots*, Nature Phys. **5**, 321 (2009).

- [10] J. R. Petta, A. C. Johnson, J. M. Taylor, E. A. Laird, A. Yacoby, M. D. Lukin, C. M. Marcus, M. P. Hanson, and A. C. Gossard, *Coherent Manipulation of Coupled Electron Spins in Semiconductor Quantum Dots*, Science **309**, 2180 (2005).
- [11] F. H. L. Koppens, C. Buizert, K.-J. Tielrooij, I. T. Vink, K. C. Nowack, L. P. Meunier, T. Kouwenhoven, and L. M. K. Vandersypen, *Driven coherent oscillations of a single electron spin in a quantum dot*, Nature **442**, 776 (2006).
- [12] O. N. Jouravlev and Y. V. Nazarov, *Electron Transport in a Double Quantum Dot Governed by a Nuclear Magnetic Field*, Phys. Rev. Lett. **96**, 176804 (2006).
- [13] J. Danon and Y. V. Nazarov, *Pauli spin blockade in the presence of strong spin-orbit coupling*, Phys. Rev. B **80**, 041301 (2009).
- [14] C. Fasth, A. Fuhrer, L. Samuelson, V. N. Golovach, and D. Loss, *Direct Measurement of the Spin-Orbit Interaction in a Two-Electron InAs Nanowire Quantum Dot*, Phys. Rev. Lett. **98**, 266801 (2007).
- [15] C. Buizert, F. H. L. Koppens, M. Pioro-Ladrière, H.-P. Tranitz, I. T. Vink, S. Tarucha, W. Wegscheider, and L. M. K. Vandersypen, *In Situ Reduction of Charge Noise in GaAs/Al<sub>x</sub>Ga<sub>1-x</sub>As Schottky-Gated Devices*, Phys. Rev. Lett. **101**, 226603 (2008).
- [16] K. Ono, D. G. Austing, Y. Tokura, and S. Tarucha, *Current Rectification by Pauli Exclusion in a Weakly Coupled Double Quantum Dot System*, Science **297**, 1313 (2002).
- [17] A. C. Johnson, J. R. Petta, C. M. Marcus, M. P. Hanson, and A. C. Gossard, *Singlet-triplet spin blockade and charge sensing in a few-electron double quantum dot*, Phys. Rev. B **72**, 165308 (2005).
- [18] I. A. Merkulov, A. L. Efros, and M. Rosen, *Electron spin relaxation by nuclei in semiconductor quantum dots*, Phys. Rev. B **65**, 205309 (2002).
- [19] V. N. Golovach, A. Khaetskii, and D. Loss, *Spin relaxation at the singlet-triplet crossing in a quantum dot*, Phys. Rev. B **77**, 045328 (2008).

- [20] S. I. Erlingsson and Y. V. Nazarov, *Hyperfine-mediated transitions between a Zeeman split doublet in GaAs quantum dots: The role of the internal field*, Phys. Rev. B **66**, 155327 (2002).
- [21] M. Trif, V. N. Golovach, and D. Loss, *Spin dynamics in InAs nanowire quantum dots coupled to a transmission line*, Phys. Rev. B **77**, 045434 (2008).
- [22] C. Flindt, A. S. Sørensen, and K. Flensberg, *Spin-Orbit Mediated Control of Spin Qubits*, Phys. Rev. Lett. **97**, 240501 (2006).
- [23] K. Ono and S. Tarucha, *Nuclear-Spin-Induced Oscillatory Current in Spin-Blockaded Quantum Dots*, Phys. Rev. Lett. **92**, 256803 (2004).
- [24] C. Weber, A. Fuhrer, C. Fasth, G. Lindwall, L. Samuelson, and A. Wacker, *Probing Confined Phonon Modes by Transport through a Nanowire Double Quantum Dot*, Phys. Rev. Lett. **104**, 036801 (2010).



# 6

## SPIN BLOCKADE ANISOTROPY IN INAS NANOWIRE DOUBLE QUANTUM DOTS

Spin blockade in InAs nanowire double quantum dots can be lifted by strong spin-orbit interaction when a finite magnetic field is applied. Here, we demonstrate that even in the presence of spin-orbit interaction, spin blockade is restored if magnetic field is applied along a certain axis. We offer an explanation of this effect in the framework of tunnel-coupled triplet and singlet states.

---

This chapter is in preparation for publication.



## 6.1 INTRODUCTION

Single electron spins confined in semiconductor quantum dots can be operated as solid state quantum bits [1, 2]. Single spin coherence is currently being investigated through transport measurements in a number of semiconducting systems including two-dimensional electron gases, donors in silicon, self-assembled dots, carbon nanotubes and semiconductor nanowires. Among those, InAs nanowires offer the advantage of strong spin-orbit interaction [3–5], which can facilitate coherent spin control using a.c. electric fields [6]. Spin-orbit interaction also modifies electronic states allowing additional transport paths through quantum dots [7]. Such effects are undesirable from the spin qubit perspective because they can lead to leakage currents reducing the visibility of blocked states. Recent experiments have demonstrated that spin-orbit interaction combined with an external magnetic field lifts triplet-singlet spin blockade in double quantum dots [4, 5, 8]. While spin-orbit effects are often highly anisotropic in confined geometries, in the double dot measurements reported so far, the orientation of magnetic field was fixed.

In this chapter we study the anisotropy of spin blockade in InAs nanowire few-electron double quantum dots. By rotating the magnetic field, spin blockade can be either strongly suppressed or fully recovered. These measurements offer an insight into the spin-orbit mechanism of singlet-triplet coupling in InAs double quantum dots. We analyze the anisotropy using a model in which the direction of the restored spin blockade is determined by the amplitudes of spin-orbit mediated tunneling from the triplet states to a singlet.

Nanowires with diameters of 40-80 nm are randomly deposited on a Si/SiO<sub>2</sub> substrate with pre-patterned local gates (Fig. 6.1a) [3]. The gates are electrically isolated from the nanowires by a 20 nm thick top layer of Si<sub>3</sub>N<sub>4</sub> dielectric. After nanowire deposition, select nanowires are contacted by Ti/Al electrodes. Measurements are performed at  $T = 275$  mK in a setup containing a two-axis vector magnet. The two magnet coils allow magnetic field to be rotated in the plane of the substrate. The magnetic field angle  $\Theta = 0$  is defined along the nanowire. Local gates 1-5 are used to define double quantum dots in nanowires. We have previously demonstrated that an InAs nanowire double dot can be tuned to the few-electron regime [5]. In this chapter we focus on the  $(1,1) \rightarrow (0,2)$  charge transition, where  $(n_L, n_R)$  corresponds to having  $n_L(n_R)$  electrons on the left(right) dot. The results were reproduced at other

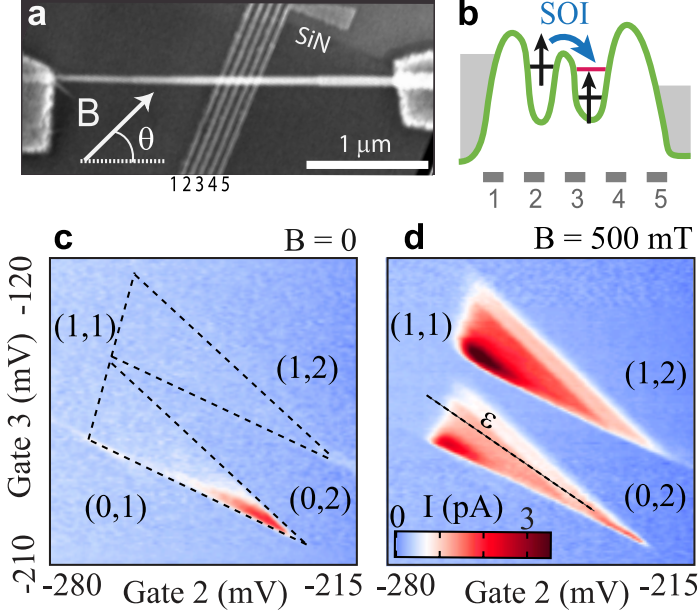


**Figure 6.1:** (a) Scanning electron microscope image of an InAs nanowire device with gates 1-5 underneath. (b) Energy level arrangement that corresponds to spin blockade with two electrons in T(1,1) state. The decay from T(1,1) can be mediated by spin-orbit interaction (SOI). (c-d) Double dot charge stability diagrams near (1,1)→(0,2) at the source-drain voltage bias of 5 meV for (c)  $B=0$ , and (d)  $B = 500$  mT,  $\Theta = 166^\circ$ . Dashed line in (d) indicates detuning axis  $\varepsilon$ .

(odd,odd)→(even,even) charge transitions.

At (1,1)→(0,2) charge transition spin blockade is observed in transport through the double dot. Spin blockade occurs when the left electron and the right electron form a triplet state T(1,1) (Fig. 6.1b). For small double dot energy level detuning  $\varepsilon$  the T(0,2) state is not energetically accessible. Therefore, the left electron can only tunnel into S(0,2). This cannot occur in the absence of spin-flip processes, therefore the average lifetime in (1,1) charge configuration can be extended due to spin blockade (Fig. 6.1c). However, in InAs nanowires T(1,1)→S(0,2) transitions can be mediated by spin-orbit interaction (Fig. 6.1b). A distinct signature of spin-orbit mechanism is in the magnetic field dependence of the double dot current. At zero magnetic field the

effect of spin-orbit interaction is cancelled due to the time-reversal symmetry, and the double dot current is suppressed (spin-blockade is robust, Fig. 6.1c). At finite field the spin-orbit mechanism is activated, and the current is restored (spin blockade is suppressed, Fig. 6.1d).

## 6.2 SPIN BLOCKADE ANISOTROPY

Data in Figures 6.1 and 6.2 correspond to the regime of strong interdot tunnel coupling. With increased tunnel coupling, the effect of spin-orbit interaction that couples triplets and singlets at finite field increases [7]. At the same time, the effect of hyperfine interaction, which mixes spin states around zero field, is reduced. As a result of these two factors, the double dot current exhibits a sharp rise as soon as small magnetic field is applied, as shown in Fig. 6.2a for magnetic field oriented at  $\Theta = 166^\circ$ .

A dramatic difference is observed when magnetic field is rotated by 90 degrees: the current remains zero up to high magnetic fields in a wide range of detuning. For this field orientation, the coupling between triplet (1,1) states and  $S(0,2)$  is strongly reduced and spin blockade is restored. A small current is observed only at high fields, where the triplet ground state is on resonance with  $S(0,2)$ . This is probably due to a residual spin-orbit effect: the magnetic field can only be rotated in the plane of the substrate, however the field direction for perfect restoration of the blockade does not necessarily have to lie within this plane.

The observed cancellation of the effect of spin-orbit interaction can be understood from general principles. For a better illustration of the role of the rotating magnetic field it is convenient to work not in the usual basis of spin-orbit eigenstates  $\tilde{T}_-$ ,  $\tilde{T}_0$  and  $\tilde{T}_+$ , but in the real-space basis  $T_z = \tilde{T}_0$ ,  $T_x = (\tilde{T}_- - \tilde{T}_+)/\sqrt{2}$ , and  $T_y = i(\tilde{T}_+ + \tilde{T}_-)/\sqrt{2}$ . The  $z$ -direction is the direction of the applied magnetic field, it gives the quantization axis along which the usual unpolarized triplet  $\tilde{T}_0 = (|\uparrow\downarrow\rangle + |\downarrow\uparrow\rangle)/\sqrt{2}$  is defined. The two new states  $T_x$  and  $T_y$  are the unpolarized triplet states along the orthogonal  $x$ - and  $y$ -axes. In other words,  $T_x$  and  $T_y$  have the same spin structure as  $T_0$ , but with a spin-quantization axis pointing along the  $x$ - and  $y$ -axis respectively, such as indicated in Fig. 6.2c.

Due to spin-orbit interaction, not only the singlet (1,1) state is coupled to  $S(0,2)$  with the amplitude  $t_s$ , but also the three triplets  $T_x$ ,  $T_y$  and  $T_z$  with

amplitudes  $t_x$ ,  $t_y$ , and  $t_z$ . The coefficients  $t_x$ ,  $t_y$ ,  $t_z$  are real numbers due to the time-reversal symmetry of the basis states  $T_x$ ,  $T_y$ ,  $T_z$  [7]. Since these three coefficients describe tunneling from the three triplets that lie along the three coordinate axes, the coupling vector  $\mathbf{t}_{SO} \equiv \{t_x, t_y, t_z\}$  can be treated as a vector in real space. Indeed, any rotation of the coordinate system is equivalent to a rotation of the basis  $\{T_x, T_y, T_z\}$ . The orientation of  $\mathbf{t}_{SO}$  itself in real space is independent of the chosen basis, because it is fixed by the spin-orbit interaction and by the double dot wavefunction. Importantly, it should be possible to perfectly align the magnetic field with the vector  $\mathbf{t}_{SO}$ , so that  $t_x = t_y = 0$ . In this case  $T_x$  and  $T_y$ , and therefore the spin-orbit eigenstates  $\tilde{T}_+$  and  $\tilde{T}_-$ , are no longer coupled to  $S(0,2)$ , so the double dot cannot decay from these states. We argue that such nearly perfect alignment of  $\mathbf{B}$  and  $\mathbf{t}_{SO}$  is responsible for the recovery of spin blockade at  $\Theta = 76^\circ$  in Fig. 6.2b.

We now take a closer look at the angle dependence of spin blockade. As the angle  $\Theta$  is changed from  $166^\circ$  to  $76^\circ$ , the spin-orbit-induced dip in the double dot current becomes wider (Fig. 6.2d). This evolution can be understood qualitatively as follows. At finite magnetic field the spin-orbit eigenstates  $\tilde{T}_+$  and  $\tilde{T}_-$  decay to  $S(0,2)$  with an amplitude  $\sim B\sqrt{t_x^2 + t_y^2}/\sqrt{t_s^2 + t_{SO}^2}$ . Assuming that the spin-orbit mechanism is the bottleneck of transport, the current through the double dot scales as  $\propto B^2(t_x^2 + t_y^2)/(t_s^2 + t_{SO}^2) = B^2 \sin^2 \alpha |\mathbf{t}_{SO}|^2/(t_s^2 + t_{SO}^2)$ , where  $\alpha$  is the angle between the vectors  $\mathbf{B}$  and  $\mathbf{t}_{SO}$ . The field at which this spin-orbit mediated decay channel starts to contribute significantly to the current depends on the strength of the other competing channels, such as flip-flops with nuclear spins or spin relaxation described by the rate  $\Gamma_{rel}$ . In any case however, the *width* of the zero-field dip will scale as  $\propto \sqrt{t_s^2 + t_{SO}^2}/(|\mathbf{t}_{SO}| \sin \alpha)$ .

The evolution of the zero-field dip in Fig. 6.2d can be reproduced numerically using the rate equation model described in Refs. [5, 7]. The model includes the triplet-singlet coupling vector  $\mathbf{t}_{SO}$  as described above, as well as the hyperfine interaction of the electron spins with randomly polarized baths of nuclear spins. The fits are obtained with  $\mathbf{t}_{SO}$  pointing along  $\Theta = 76^\circ$  with the magnitude  $|\mathbf{t}_{SO}| = 10.5 \mu\text{eV}$ . The conventional  $S(1,1) \rightarrow S(0,2)$  coupling  $t_s = |\mathbf{t}_{SO}|/0.13$  is in agreement with earlier findings [5]. The outgoing barrier strength was  $\Gamma_{out} = 7 \mu\text{eV}$  and the relaxation rate  $\Gamma_{rel} = 0.003 \mu\text{eV}$ . We averaged over 1000 effective nuclear fields in both dots, taken from a normal distribution with an r.m.s. of  $g\mu_B B_N = 0.4 \mu\text{eV}$ . Since in this experiment

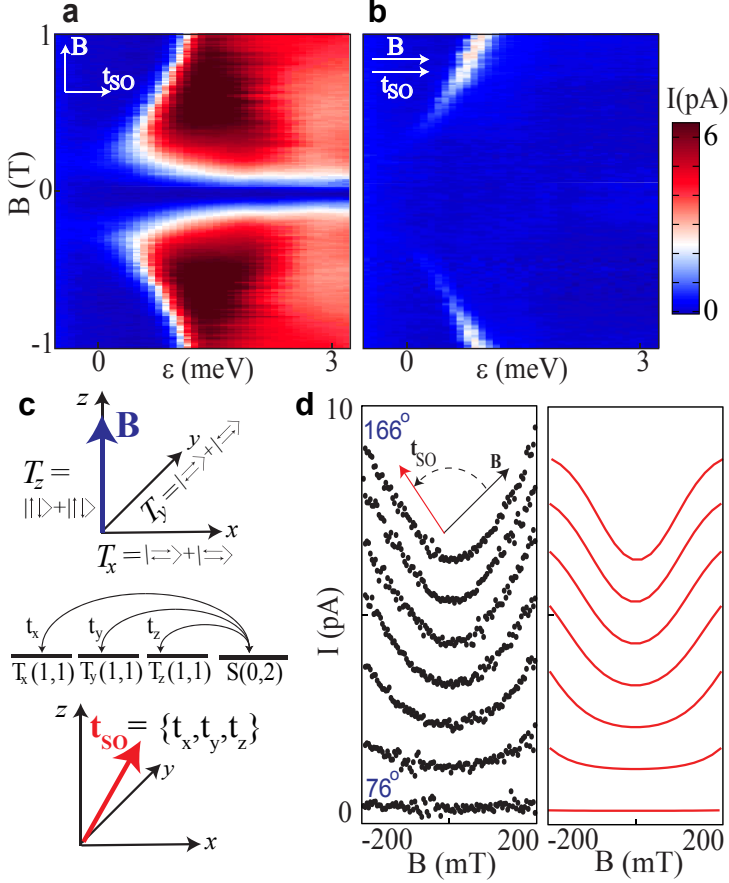


**Figure 6.2:** (a-b) Current as a function of dot detuning and magnetic field strength for (a)  $\Theta = 166^\circ$  and (b)  $\Theta = 76^\circ$ . (c) (top) Spatial orientation and spin arrangement that corresponds to states  $T_x, T_y, T_z$ . (middle)  $T_x, T_y, T_z$  are coupled to  $S(0,2)$  with amplitudes  $t_x, t_y, t_z$  which form a vector  $t_{SO}$  (bottom). (d) Zero-field dip at  $\epsilon = 1$ meV for different angles  $\Theta$  in steps of  $15^\circ$ . On the right, current levels reproduced using the model described in the text are shown. Both experimental and calculated curves are offset by 1 pA for clarity.

magnetic field can be rotated in the plane of the substrate, the cancellation of the effect of spin-orbit interaction on spin blockade is limited by the out-of-plane component of  $t_{SO}$ , i.e. there is a minimal angle  $\alpha$  corresponding to the maximal width of the dip. From the fits in Fig. 6.2d and the high magnetic

field data in Fig. 6.2b, we estimate that the minimal angle  $\alpha$  is smaller than  $10^\circ$ .

We note that the suppression of the current is not likely related to hysteresis effects due to dynamic nuclear polarization [4]. Smooth evolution of the zero-field dip in Fig. 6.2d is not consistent with dynamic nuclear polarization effects which typically manifest in time-dependent current and spontaneous jumps between the low and the high current states [4]. This device also exhibits a  $g$ -factor anisotropy with a minimum of  $\sim 6$  and a maximum of  $\sim 8$  (see Chapter 4). Since the zero-field dip in the strong coupling regime simply scales with the Zeeman energy [7], this change in  $g$ -factor is expected to change the dip width by 30% in two orthogonal directions. This cannot explain the dramatic increase in the dip width in Fig. 6.2d.

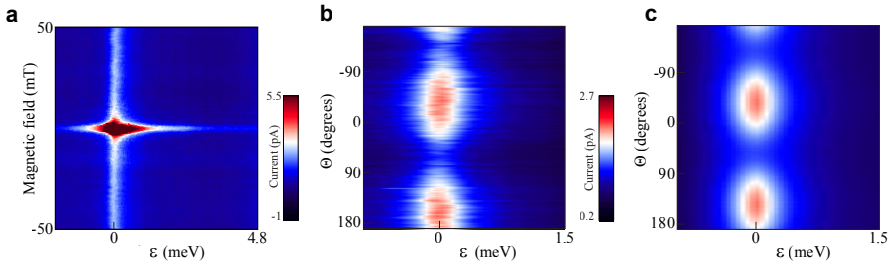


**Figure 6.3:** (a) Magnetic field dependence of the current through spin-blockade versus detuning for a weakly coupled double dot,  $t \sim 0.1 \mu\text{eV}$ . (b) Rotating the magnetic field results in a modulation of the elastic current around zero detuning. The magnitude of the field is  $|\mathbf{B}| = 20$  mT. (c) Using the transport model we can reproduce the observed angle dependence with  $t_x = 0.09t \sin(\Theta - 63^\circ) + t_y$  and  $t_y < 0.1t_x$ .

## 6.3 WEAK COUPLING

Spin blockade anisotropy was also observed in the regime of weak interdot coupling (Fig. 6.3). In this regime, spin blockade is stronger influenced by the hyperfine interaction than in the strong coupling. The hyperfine interaction mixes T(1,1) states with S(1,1) around  $\mathbf{B} = 0$ , inducing a peak in current at zero field (Fig. 6.3a). The effect of hyperfine interaction is suppressed for magnetic fields  $|\mathbf{B}| \gg B_N$ , where  $B_N$  is the r.m.s. nuclear field experienced by an electron in a dot [9]. Beyond the hyperfine peak, finite current can still

be enabled by spin-orbit interaction [5]. Figs. 6.3b and 6.3c show that when the magnetic field  $B = 20$  mT is rotated in the substrate plane the current is modulated, as in the strong coupling regime in Fig. 6.2. The minimum current corresponds to the best alignment of the magnetic field with the  $\mathbf{t}_{SO}$  vector, as confirmed by a numerical simulation in Fig. 6.3c. The anisotropy in this regime is reproduced by the model in Ref. [7].

The vector  $\mathbf{t}_{SO}$  was found to point in different directions in Figs. 6.2 and 6.3, below we discuss this in more detail. The direction of  $\mathbf{t}_{SO}$  in a double quantum dot can be influenced by three main factors. The first is the bulk spin-orbit interaction in the nanowire which includes terms due to the breaking of the bulk inversion symmetry and of the structure inversion symmetry. The interference of these two terms may lead to anisotropic spin-orbit interaction. The second factor is the confinement of single electrons. The shapes of left and right orbitals determine the orientations of the effective spin-orbit magnetic fields in left and right dots. A change in the shapes of the orbitals may lead to a change in the direction of spin-orbit effect suppression. The third factor is the exact overlap of the wavefunctions in the two dots. This overlap directly influences the tunneling rates between singlet or triplet (1,1) states and S(0,2) and hence the direction of  $\mathbf{t}_{SO}$ . The theory in Ref. [7] suggests that the third factor, an exact overlap between the wavefunctions in the two dots determines the direction of anisotropy. In other words, small changes in tuning of the double dot can induce large fluctuations of  $\mathbf{t}_{SO}$ . Although our measurements show that changing of the double dot potential can indeed induce changes in the direction of  $\mathbf{t}_{SO}$ , we did not observe strong fluctuations of this directions which would unambiguously prove that microscopic details of confining potential determine the preferential direction of spin blockade anisotropy.

In conclusion, we have demonstrated that spin blockade in a double quantum dots is anisotropic. This anisotropy can be described by a real-space triplet-singlet tunneling vector the result of spin-orbit coupling. The alignment of the magnetic field to this vector suppresses spin mixing between the dots. The result is that spin blockade can be sustained up to large magnetic fields. Further understanding of the effect of the anisotropy of spin-orbit coupling on electron's spin in a nanowire quantum dot can be gained from measurements of spin coherence.

---

This work has been done in collaboration with J. W. W. van Tilburg, S.M. Frolov, K. Zuo, J. Danon, Yu. V. Nazarov, M. Hocevar, E. P. A. M. Bakkers and L. P. Kouwenhoven.

## REFERENCES

- [1] D. Loss and D. P. DiVincenzo, *Quantum computation with quantum dots*, Phys. Rev. A **57**, 120 (1998).
- [2] R. Hanson, L. P. Kouwenhoven, J. R. Petta, S. Tarucha, and L. M. K. Vandersypen, *Spins in few-electron quantum dots*, Rev. Mod. Phys. **79**, 1217 (2007).
- [3] C. Fasth, A. Fuhrer, L. Samuelson, V. N. Golovach, and D. Loss, *Direct Measurement of the Spin-Orbit Interaction in a Two-Electron InAs Nanowire Quantum Dot*, Phys. Rev. Lett. **98**, 266801 (2007).
- [4] A. Pfund, I. Shorubalko, K. Ensslin, and R. Leturcq, *Suppression of Spin Relaxation in an InAs Nanowire Double Quantum Dot*, Phys. Rev. Lett. **99**, 036801 (2007).
- [5] S. Nadj-Perge, S. M. Frolov, J. W. W. van Tilburg, J. Danon, Y. V. Nazarov, R. Algra, E. P. A. M. Bakkers, and L. P. Kouwenhoven, *Disentangling the effects of spin-orbit and hyperfine interactions on spin blockade*, Phys. Rev. B **81**, 201305 (2010).
- [6] K. C. Nowack, F. H. L. Koppens, Y. V. Nazarov, and L. M. K. Vandersypen, *Coherent Control of a Single Electron Spin with Electric Fields*, Science **318**, 1430 (2007).
- [7] J. Danon and Y. V. Nazarov, *Pauli spin blockade in the presence of strong spin-orbit coupling*, Phys. Rev. B **80**, 041301 (2009).
- [8] A. Pfund, I. Shorubalko, K. Ensslin, and R. Leturcq, *Spin-state mixing in InAs double quantum dots*, Phys. Rev. B **76**, 161308 (2007).
- [9] I. A. Merkulov, A. L. Efros, and M. Rosen, *Electron spin relaxation by nuclei in semiconductor quantum dots*, Phys. Rev. B **65**, 205309 (2002).





# 7

## SPIN-ORBIT QUBIT IN A SEMICONDUCTOR NANOWIRE

In this chapter, we demonstrate universal coherent control of single spin-orbit qubits in an InAs nanowire. To prepare and detect qubit states we use spin blockade. We observe Rabi oscillations driven, by electric dipole spin resonance (EDSR) and mediated by spin-orbit interaction. The highest Rabi frequency achieved is  $58 \pm 2$  MHz. Due to a difference in Landé  $g$ -factors for the two quantum dots we can selectively address the two qubits with high-frequency electric fields. The Ramsey decay time of  $8 \pm 1$  ns suggests that nuclear spin bath is the main source of dephasing for this system. The coherence time is extended to  $\sim 200$  ns using dynamical decoupling techniques.

---

This chapter is accepted for publication in Nature.

## 7.1 INTRODUCTION

Motion of electrons can influence their spins through a fundamental effect called spin-orbit interaction. This interaction provides a way to electrically control spins and as such lies at the foundation of spintronics [1]. Even at the level of single electrons, spin-orbit interaction has proven promising for coherent spin rotations [2]. Here we report a spin-orbit quantum bit implemented in an InAs nanowire, where spin-orbit interaction is so strong that spin and motion can no longer be separated [3, 4]. In this regime we realize fast qubit rotations and universal single qubit control using only electric fields. We enhance coherence by dynamically decoupling the qubit from the environment. Our qubits are individually addressable: they are hosted in single-electron quantum dots, each of which has a different Landé  $g$ -factor. The demonstration of a nanowire qubit opens ways to harness the advantages of nanowires for use in quantum computing. Nanowires can serve as one-dimensional templates for scalable qubit registers. Unique to nanowires is the possibility to easily vary the material even during wire growth [5]. Such flexibility can be used to design wires with suppressed decoherence and push semiconductor qubit fidelities towards error-correction levels. Furthermore, electrical dots can be integrated with optical dots in p-n junction nanowires [6]. The coherence times achieved here are sufficient for the conversion of an electronic qubit into a photon, the flying qubit, for long-distance quantum communication.

## 7.2 EDSR DETECTION

Figure 7.1a shows a scanning electron microscope image of our nanowire device. Two electrodes, source and drain, are used to apply a voltage bias of 6 mV across the InAs nanowire. Voltages applied to five closely spaced narrow gates underneath the nanowire create a confinement potential for two electrons separated by a tunnelling barrier. The defined structure is known as a double quantum dot in the (1,1) charge configuration [7].

Each of the two electrons represents a spin-orbit qubit (Fig. 7.1b). In the presence of the strong spin-orbit coupling neither spin nor orbital number are separately well defined. Instead, the two qubit states are a spin-orbit doublet,  $\uparrow$  and  $\downarrow$ . Similar to pure spin states, magnetic field  $B$  controls the energy splitting between spin-orbit states  $E_Z = g\mu_B B$ , where  $g$  is the Landé  $g$ -factor

in a quantum dot,  $\mu_B$  is the Bohr magneton. The crucial difference from a spin qubit is that in a spin-orbit qubit the orbital part of the spin-orbit wavefunction is used for qubit manipulation [2, 8].

The qubit readout and initialization rely on the effect of spin blockade [9, 10]. A source-drain bias induces a current of electrons passing one-by-one through the double dot. The process of electron transfer between the dots can be energetically allowed but blocked by a spin selection rule. For instance, a (1,1)-triplet state cannot go over into a (0,2)-singlet state. This stops the left electron from tunnelling onto the right dot and thereby blocks the current. In practice the double dot becomes blocked only in a parallel configuration, *i.e.* in either a ( $\uparrow, \uparrow$ ) or a ( $\downarrow, \downarrow$ ) state, because antiparallel states decay quickly to a non-blocked singlet state [11, 12]. By simply idling in the parameter range of spin blockade the qubits will be initialized in one of the two parallel states with equal probability. We note that spin-orbit and hyperfine interactions also mediate a slower decay of parallel states into (0,2) [7, 9, 10]. This reduces the readout fidelity to 70-80 % (see section 7.5.5).

A microwave frequency electric field applied to gate 4 oscillates electrons inside the nanowire (Fig. 7.1b). This motion can induce resonant transitions between spin-orbit states via an effect called electric-dipole spin resonance (EDSR) [2, 8, 13–16]. Such transitions are expected when the frequency of the a.c. electric field is equal to the Larmor frequency,  $f_0 = g\mu_B B/h$ . At resonance the spin-orbit state of the double dot rapidly changes from parallel to antiparallel. The antiparallel state does not experience spin blockade, so the left electron tunnels to the right and thereby contributing to the current. Figure 7.1c shows the resonance as a "V" shape which maps out the Larmor frequency in the plane of microwave frequency and magnetic field.

The "V" resonance signal vanishes in the vicinity of zero magnetic field. This behaviour is consistent with spin-orbit mediated EDSR: the effect of spin-orbit interaction must cancel at zero field due to time-reversal symmetry [2, 16]. The field-dependent EDSR strength rules out a.c. magnetic field and hyperfine field gradient as possible mechanisms. A  $g$ -tensor modulation in our nanowires is estimated to be too weak to drive EDSR (see section 7.5.2 for discussion of EDSR mechanisms). The current peak near zero magnetic field arises from the hyperfine interaction between electron spin and nuclear spin bath [11, 12]. From the width of this hyperfine-induced peak we extract the r.m.s. magnetic field generated by the fluctuating nuclear spins  $B_N = 0.66 \pm 0.1$  mT [17].

The width of the EDSR line at low microwave power is also consistent with a broadening due to fluctuating nuclear spins (*i.e.* the side EDSR peaks and the central hyperfine peak have comparable widths in Fig. 7.1d) [18].

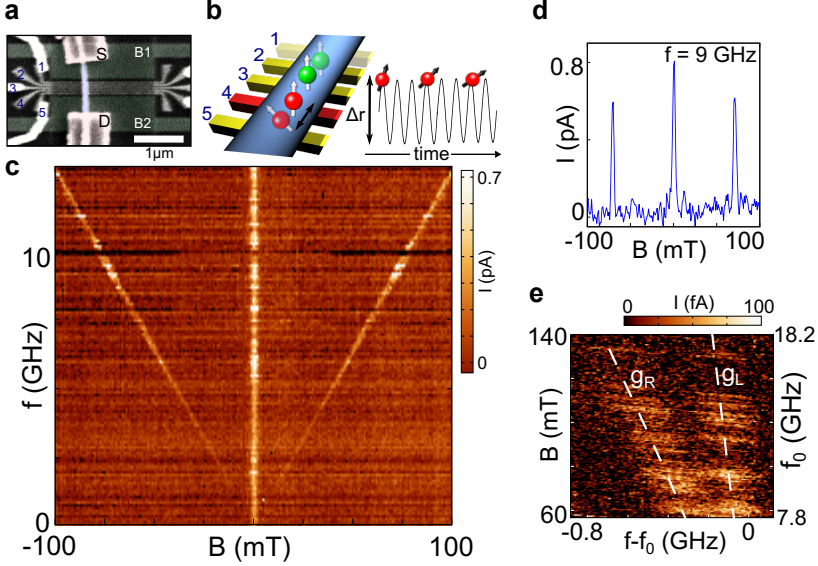


**Figure 7.1:** Electric-dipole spin resonance. (a) scanning electron microscope image of a prototype device showing source (S) and drain (D) contacts, narrow gates 1-5 and wide gates B1 and B2. (b) schematic of spin-orbit qubit manipulation. Two quantum dots are formed between gates 2-5. Microwave electric field applied to gate 4 oscillates both electrons with amplitude  $\sim \Delta r$ . When only the left (red) electron is on resonance, EDSR rotates the left qubit. The right (green) electron is operated as a spin blockade detector. (c) spin blockade is lifted near  $B = 0$  and on resonance when the microwave frequency,  $f$ , matches the qubit precession frequency,  $g\mu_B B/h$ . Here, microwave power is  $P = -42$  dBm. (d) trace extracted from (c) at  $f = 9$  GHz. (e) Zoom in on the EDSR line which is split at high  $B$  due to a difference between  $g_L$  and  $g_R$ . At each magnetic field, the frequency is swept in a fixed range around  $f_0 = g\mu_B B/h$  calculated with  $g = 9.28$ . Current on resonance varies along due to non-monotonic microwave transmission.

At higher magnetic field the resonance line splits up (Fig. 7.1e), indicating that the  $g$ -factors in the left and right dots,  $g_L$  and  $g_R$ , are different. This is expected for quantum dots of different sizes since confinement changes the effective  $g$ -factor [19]. We measured the confinement as the orbital excitation energy at the  $(1, 0) \leftrightarrow (0, 1)$  transition and found  $7.5 \pm 0.1$  meV for the left

dot and  $9.0 \pm 0.2$  meV for the right dot. A smaller orbital energy should correspond to a larger  $g$ -factor in InAs, therefore we assign  $|g_L| = 9.2 \pm 0.1$  and  $|g_R| = 8.9 \pm 0.1$ . At frequencies above 10 GHz the two resonances are more than a linewidth apart, allowing us to control the left or the right qubit separately [8].

### 7.3 COHERENT OSCILLATIONS

Coherent control over spin-orbit states is demonstrated in a time-resolved measurement of Rabi oscillations, [2, 18, 21] explained in Figs. 7.2a and 7.2b. Periodic square pulses shift the relative positions of the energy levels in the two dots between spin blockade (SB) and Coulomb blockade (CB). First, the double dot is initialized in a parallel state by idling in SB. This is followed by a shift to CB from which electrons cannot escape. While in CB, a resonant microwave burst is applied for a time  $\tau_{burst}$  to induce qubit rotation. Finally, the double dot is brought back into SB for readout. At the readout stage the probability of the left electron to tunnel out is proportional to the projection of the final state onto the singlet (1,1). This cycle is repeated continuously.

The singlet component in the final state is measured as the d.c. current. The current oscillates as  $\tau_{burst}$  is varied reflecting Rabi oscillations of the driven qubit (Fig. 7.2c). Rabi oscillations are observed in the range of driving frequencies  $f \approx 9 - 19$  GHz. Rabi oscillations are not observed at lower frequencies (and lower magnetic fields) because the effective spin-orbit field  $B_{SO} < B_N$ , such that nuclear fluctuations average out the coherent qubit dynamics. We note that the observation of incoherent EDSR (Fig. 7.1c) requires a much smaller  $B_{SO}$ , because even qubit rotations with a random phase contribute to extra current near resonance.

Our highest Rabi frequency is  $f_R = 58 \pm 2$  MHz (Fig. 7.2d), achieved at  $f = 13$  GHz. The field  $B_{SO}$  is expected to grow with  $B$  [22], however at higher driving frequencies the Rabi frequency is limited by the maximum microwave source power and by the reduced transmission of the microwave circuit. With the strongest driving the amplitude of the orbital oscillation is estimated to reach 1 nm. The qubit state is flipped in  $\sim 110$  microwave periods, and thus rotated by  $\sim 1.6^\circ$  per cycle of the orbital motion.

We can resolve up to 5 Rabi oscillation periods. The damping of the oscillations at  $P < -32$  dBm is consistent with a  $\sim (\tau_{burst})^{-0.5}$  decay envelope

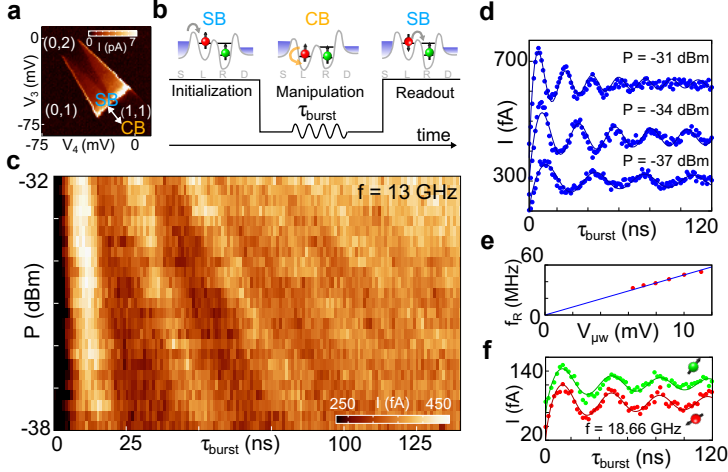


**Figure 7.2:** Rabi oscillations. (a) charge stability diagram near the  $(1, 1) \leftarrow (0, 2)$  transition. Gate voltages  $V_3$  and  $V_4$  on gates 3 and 4 are swept and current,  $I$ , is measured. The labels 'CB' and 'SB' indicate the qubit working points of Coulomb Blockade and Spin Blockade. The observed non-zero current in SB arises from spin-orbit interaction [7, 10]. (b) each measurement cycle consists of an initialization, manipulation and readout stage. Diagrams on top show electrochemical potentials of the source (S), drain (D), left dot (L) and right dot (R). Square pulses are applied synchronously to gates 2 and 4. Microwave bursts are applied to gate 4. (c) Rabi oscillations at for a range of microwave burst power  $f = 13$  GHz,  $B = 102$  mT. (d) Rabi traces at  $f = 13$  GHz with fits to  $a \cdot \cos(f_R \tau_{burst} + \varphi) / \tau^d + b$  ( $d = 0.8$  for top trace and  $d = 0.5$  for the two bottom traces) [20]. Rabi frequencies,  $f_R$ , are  $58 \pm 2$ ,  $43 \pm 2$  and  $32 \pm 2$  MHz (top to bottom). Linear slopes of  $2\text{fA/ns}$ ,  $1\text{fA/ns}$  and  $0.3\text{fA/ns}$  (top to bottom) are subtracted to flatten the average. They are attributed to photon-assisted tunneling. Traces are offset vertically for clarity. (e) dependence of  $f_R$  on driving amplitude,  $V_{\mu w}$  ( $V_{\mu w} = 2(P \cdot 50\Omega)^{0.5}$ ) with a linear fit. (f) Separate Rabi oscillations of the left (red) and right (green) qubit at  $f = 18.66$  GHz with  $f_R = 29 \pm 2$  MHz fitted to the expression used in (d). The magnetic field is tuned to 144 mT and 149 mT for the upper and the lower trace respectively.

observed previously for rotations of a single spin interacting with a slow nuclear bath [20]. We have verified that spin relaxation does not limit coherent evolution on timescales up to  $1 \mu\text{s}$  (see section 7.5.3). The qubit manipulation fidelity is  $48 \pm 2\%$  estimated by comparing the values of  $B_{SO}$  and  $B_N$  (see section 7.5.5) [18]. As expected, the Rabi frequency is proportional to the square root of the microwave power  $P$  applied to the gate (Fig. 7.2e). Absorption of microwave photons enables interdot tunnelling regardless of the qubit state.

This effect likely accelerates the decay of Rabi oscillations near the highest power (Fig. 7.2d, upper trace)[2, 18]. However, the apparent photon-assisted tunnelling is substantially reduced for  $P < -32$  dBm, while Rabi frequencies remain high.

In Figures 7.2c, 7.2d only the left qubit is rotated. Figure 7.2f shows coherent rotations of either the left or the right qubit induced at the same microwave frequency but at two different magnetic fields, which correspond to the two EDSR resonance conditions shown in Figure 7.1e (see section 7.5.4 for more data) [23].

## 7.4 FREE EVOLUTION AND DYNAMICAL DECOUPLING

In the Rabi experiment the spin-orbit state is rotated only around one axis. This is not enough for qubit operation, which ultimately requires the preparation of an arbitrary superposition of  $\uparrow$  and  $\downarrow$ , known as universal control [24–26]. Such ability is demonstrated in a Ramsey experiment (Figs. 7.3a, 7.3b). Now two short bursts with a different microwave phase are applied during the manipulation stage. In the reference frame that rotates at the Larmor frequency, the qubit is initially rotated from  $|+z\rangle$  to  $|-y\rangle$  on the Bloch sphere by applying a  $\pi/2$  rotation around the x-axis. After a delay time  $\tau$  we apply a  $3\pi/2$  pulse. The tunable phase of the microwave signal  $\phi$  sets the axis of the second rotation ( $\phi = 0$  corresponds to a rotation around x,  $\phi = \pi/2$  corresponds to a rotation around y). The final z-component depends on the axis of the second rotation as well as on dephasing. The double dot current oscillates with  $\phi$  revealing the Ramsey fringes (Fig. 7.3a). The contrast of the Ramsey fringes decreases with increasing  $\tau$ , allowing us to determine the inhomogeneous dephasing time  $T_2^* = 8 \pm 1$  ns (Fig. 7.3b).

Coherence can be extended by a Hahn echo technique, which partially cancels dephasing coming from a slowly varying nuclear magnetic field (Figs. 7.3c, 7.3d). In the echo sequence a  $\pi$  pulse is applied half way between the two  $\pi/2$  pulses. The contrast of the Ramsey fringes is extended to longer coherent evolution times by performing Hahn echo (Fig. 7.3c). The phase of the fringes can be flipped depending on whether the  $\pi$  rotation is around the  $x$ -axis ( $\pi_x$ ) or around the  $y$ -axis ( $\pi_y$ ). Both  $\pi_x$  and  $\pi_y$  Hahn echo's increase the coherence time to  $T_{echo} = 50 \pm 5$  ns (Fig. 7.3d).



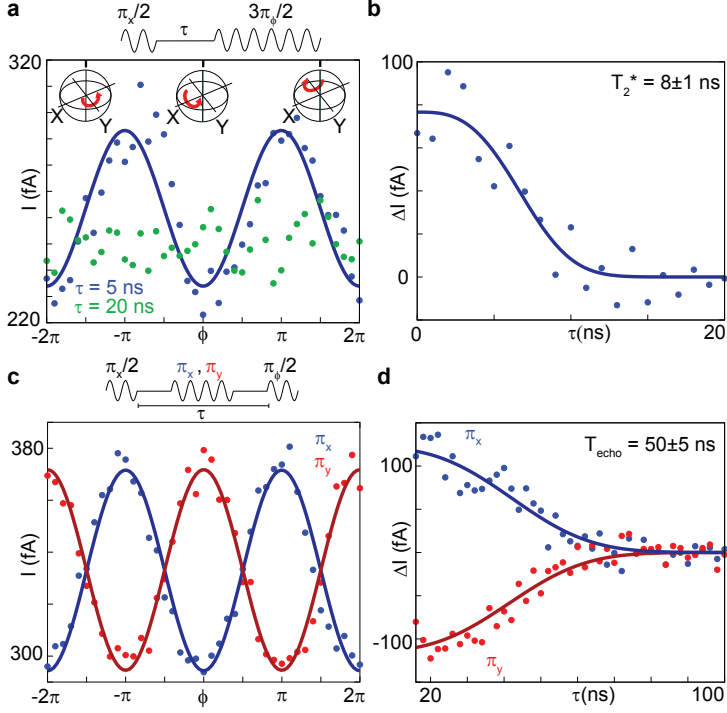


**Figure 7.3:** Universal qubit control and coherence times. (a) Ramsey schematic (top) and measurement. A Ramsey fringe  $I(\phi)$  is observed for short delays  $\tau < 10$  ns, but the contrast vanishes for  $\tau = 20$  ns indicating a fully dephased state. The axes of the second rotation are indicated with red arrows on the Bloch spheres for three values of  $\phi$ . (b) Decay of the Ramsey fringe contrast  $\Delta I = I(\phi = \pi) - I(\phi = 0)$  fit to  $\exp(-(\tau/T_2^*)^2)$ . (c) Hahn echo sequence (top) extends fringe contrast beyond  $\tau = 34$  ns. Fringes for two orthogonal phases of the  $\pi$  pulse are out of phase. (d) decay of the contrast of the fringes obtained for the two Hahn echo sequences is used to extract  $T_{echo}$  from a fit to  $\exp(-(\tau/T_{echo})^3)$ . A fit to  $\exp(-(\tau/T_{echo})^4)$  gives a similar value of  $T_{echo}$ . In this figure the duration of a  $\pi$  pulse is 14 ns using  $P = -35$  dBm,  $f = 13$  GHz,  $B = 102$  mT.

Gate-defined spin qubits were previously only realized in lateral quantum dots in GaAs/AlGaAs two-dimensional electron gases [9]. Due to the much stronger spin-orbit interaction in InAs, the Rabi frequencies in our InAs nanowire spin-orbit qubits are more than an order of magnitude higher than in GaAs dots [2]. Dephasing times  $T_2^*$  are of the same order in InAs and GaAs

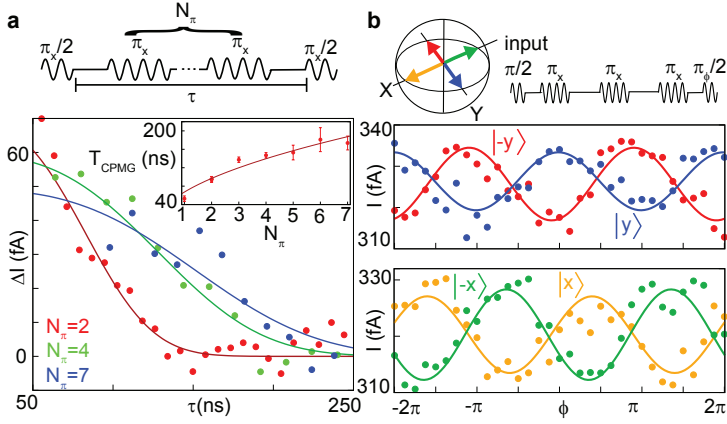


**Figure 7.4:** Dynamical decoupling. (a) decay of the contrast of the Ramsey fringes for CPMG sequences (top) with the increasing number of  $\pi$  pulses  $N_\pi$ . Solid lines are fits to  $\exp(-(\tau/T_{CPMG})^3)$ . Inset: the coherence times  $T_{CPMG}$  vs.  $N_\pi$  are fit to  $N_\pi^d$  with  $d = 0.53 \pm 0.1$ . Error bars are standard deviations of  $\Delta I(\tau)$  fits. (b) Ramsey fringes for four different phases of the initial  $\pi/2$  pulse obtained for a  $N_\pi = 3$  CPMG sequence (shown above the panel) with  $\tau = 150$  ns. The input states are indicated with arrows on the Bloch sphere. In this figure the duration of a  $\pi$  pulse is 8 ns at  $P = -32$  dBm,  $f = 13$  GHz,  $B = 102$  mT.

quantum dots [24, 27]. The relatively short  $T_{echo}$  found in the present work encourages a further study. A likely reason is faster nuclear spin fluctuations caused by the large nuclear spin of indium  $I_{In} = 9/2$ . However, charge noise and nearby paramagnetic impurities cannot be ruled out as significant dephasing sources (see section 7.5.6). Nanowires offer future solutions for suppressing the effects from nuclear spins, such as nanowires with sections of nuclear spin-free silicon. The qubit can be stored in a silicon section of the nanowire, and only moved to an InAs section for manipulation using spin-orbit interaction.

Already in the present qubit longer coherence times are achieved by Carr-Purcell-Meiboom-Gill (CPMG) dynamical decoupling pulse sequences (Fig. 7.4a) [28, 29]. Now a single echo  $\pi$  pulse is replaced with an array of equidistant  $\pi$  pulses, each of which refocuses the qubit state. The total time of coherent evolution grows as the number of  $\pi$  pulses is increased (Fig. 7.4a (inset)). Importantly, arbitrary prepared qubit state in the X-Y plane is preserved during the decoupling sequence. This is verified in Fig. 7.4b which shows that

the phase of the initial  $\pi/2$  pulse determines the phase of the Ramsey fringes. Similar evaluation was carried out for CPMG sequences up to  $7\pi$  pulses. In the future more efficient dynamical decoupling can be achieved using nuclear spin state preparation [28, 30] in combination with faster  $\pi$  pulses or adiabatic pulse techniques [31].

## 7.5 SUPPLEMENTARY INFORMATION

### 7.5.1 ADDITIONAL METHODS

Devices are fabricated on undoped Si substrates. Instead of a global back gate, two wide gates B1 and B2 are located underneath the nanowire contacts (Fig. 7.1a). They are set to constant positive voltages to enhance conductance through the nanowire. The wide gates are covered by a 50 nm layer of  $\text{Si}_3\text{N}_4$  dielectric, on top of this layer narrow gates and another 25 nm layer of  $\text{Si}_3\text{N}_4$  are deposited. InAs nanowires with diameters between 50-80 nm are grown free of stacking faults using metal-organic vapour phase epitaxy (MOVPE). The wires have the wurtzite crystal symmetry with the *c*-axis along the long nanowire axis. Nanowires are transferred in air from the mother chip to the device substrates which already contain Ti/Au gates. Selected wires are contacted with ohmic Ti/Al electrodes, during the same step contacts are made to the gates. Measurements are performed in a  $\text{He}^3$  refrigerator at  $T = 300$  mK. Magnetic field is applied in the plane of the substrate at an angle of  $45 \pm 5^\circ$  with respect to the nanowire. High frequency pulses are created using two arbitrary waveform generators (1 gigasample/second) and a 20 GHz / 23 dBm microwave vector source. Pulses are delivered to the sample via silver-plated CuNi coaxial lines with 36-dB of attenuators, followed by coplanar striplines printed on the sample holder. The pulse period should remain less than  $2 \mu\text{s}$  in order to detect the double dot current, limited by the noise floor of the d.c. current amplifier. A measurement cycle lasts  $2 \mu\text{s}$  in Fig. 7.2f. In the rest of the chapter a cycle lasts 600 ns and each data point is averaged over 5-40 million cycles.

Coaxial lines with 20 GHz bandwidth are connected to gates 2 and 4 via low temperature bias tees assembled on the sample holder (Fig. 7.5a). The amplitudes of the square pulses applied from the main 2-channel arbitrary waveform generator (AWG) to both gates 2 and 4 are adjusted in order to

shift the energy levels between SB and CB along the energy detuning axis (Fig. 7.5b). This ensures that a high amplitude microwave signal, which reaches  $V_{\mu w} = 10 - 15$  mV on the gates and shifts the double dot energy levels by  $eV_{ac} = 1 - 2$  meV, does not shift the double dot out of the (1,1) state while in CB (Fig. 7.5c). A microwave signal is applied to gate 4 and is combined with a square pulse from the main AWG. Control over the phase of the microwave signal that was used for Ramsey, Hahn echo and CPMG experiments is achieved with a secondary AWG which is connected to inputs I and Q of the vector microwave source (MW). Both AWGs are synchronized with the MW source by sharing a 10 MHz reference. The secondary AWG is triggered by the main AWG with a jitter of 200 ps.

## 7.5.2 ESTABLISHING THE EDSR MECHANISM

**Spin-orbit mechanism.** We argue that in this work spin-orbit interaction mediates EDSR. Our argument is based on the fact that the resonance signal vanishes at zero magnetic field, and on the comparison of the expected strength of the effective spin-orbit magnetic field with the values extracted from Rabi oscillations. Furthermore we explain here why alternative mechanisms can be excluded.

The effective a.c. magnetic field due to the spin-orbit interaction is estimated using the expression derived for quantum dots and the Rashba spin-orbit Hamiltonian [22]:

$$B_{SO}(t) = 2B \frac{\Delta r(t)}{l_{SO}}. \quad (7.1)$$

Here  $\Delta r(t) = l_{dot} e |E(t)| l_{dot} / \Delta$  is the displacement of the electron wavefunction and  $l_{SO} = 100-200$  nm is the spin-orbit length for InAs nanowires [3]. Orbital energy and the size of the dot are  $\Delta = 7 - 9$  meV and  $l_{dot} = \hbar / \sqrt{m^* \Delta} \approx 15$  nm,  $m^*$  is the effective mass for electrons in wurtzite InAs. Note that the effective mass in wurtzite InAs has not been measured. It is predicted to be anisotropic with values  $0.06m_e$  for momenta parallel to the nanowire axis, and  $0.042m_e$  for momenta perpendicular to the nanowire axis [32]. The electric field  $E(t)$  that drives the EDSR can be estimated from Fig. 7.5b assuming that the a.c. voltage  $V_{ac}$  due to microwaves drops linearly over the nanowire diameter  $D$ :  $E = V_{ac}/D = 1-2$  mV/50 nm =  $(2-4) \cdot 10^4$  V/m. This results in a displacement amplitude of  $\Delta r = 0.5 - 1$  nm and effective spin orbit field of  $B_{SO} \sim 0.5 - 2$  mT at  $B = 100$  mT. Experimentally we can extract  $B_{SO}$

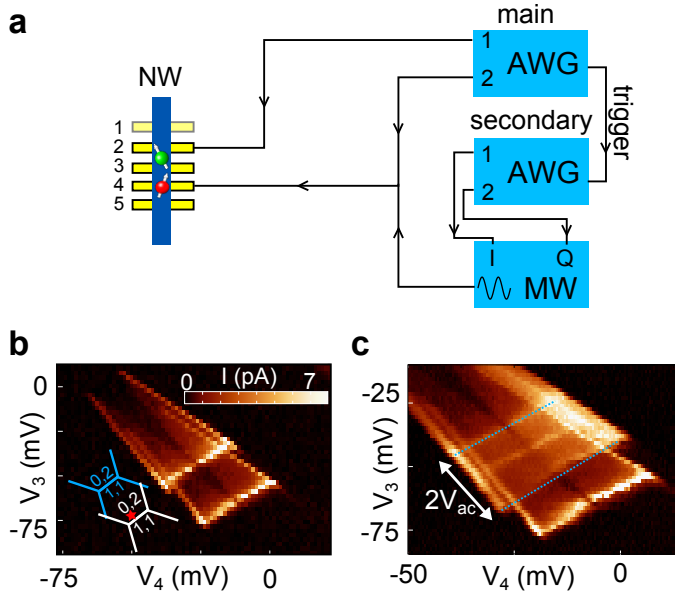


**Figure 7.5:** (a) simplified schematic of the microwave setup. (b), charge stability diagram around the  $(1,1) \rightarrow (0,2)$  transition at  $V_{SD} = 3$  mV showing the effect of the applied square pulses, without microwaves. The two triangles are displaced along the detuning axis. Charge stability diagrams for the two voltage levels of the square pulse are shown in the lower left inset. At a fixed point between the baselines of the two sets of triangles (red star) the double dot state changes between CB (upper triangle, blue diagram) and SB (lower triangle, white diagram). (c), same as panel (b), but with microwaves turned on. Microwaves detune the levels of the double dot and therefore blur the upper triangle. Voltage drop across the tunnel barrier  $V_{ac} \approx 1$  mV can be estimated from the displacement of the baseline (blue dotted lines) compared with the full size of the triangle given by the source drain bias.

from the measured Rabi frequencies. For  $f_R = g\mu_B B_{SO}/2\hbar = 60$  MHz, the highest Rabi frequency achieved at  $B = 100$  mT, we obtain  $B_{SO} \approx 0.9$  mT in good agreement with the estimate based on Equation (7.1). Equation 7.1 indicates that  $B_{SO}$  vanishes in the vicinity of zero field, meaning that the spin-orbit mechanism of EDSR becomes ineffective. Fig. 7.6 demonstrates that the EDSR signal indeed vanishes at zero field. We note that in a simple rate equation model the amplitude of the resonance peak is expected to follow a  $(B_{SO})^2$  dependence [33]. Such quadratic dependence is not apparent from the data (Fig. 7.6b), though signal-to-noise ratio here is too low to differentiate between a linear and a quadratic dependence.

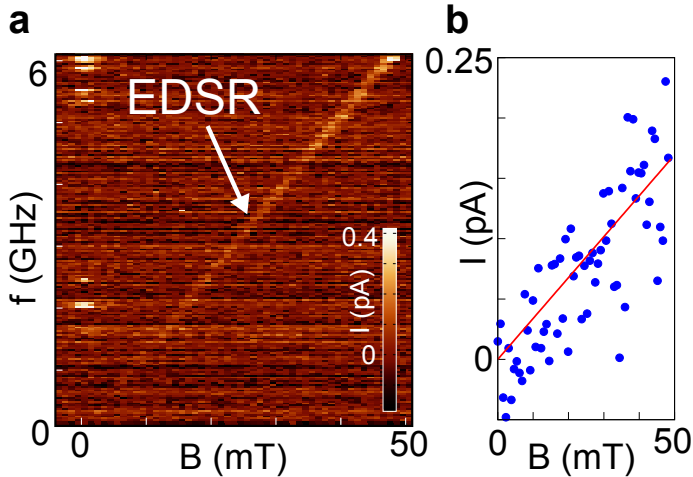


**Figure 7.6:** (a) current through the double dot measured while sweeping frequency and stepping magnetic field. Background containing resonances is subtracted for clarity. (b) blue dots correspond to the maximum current along the EDSR line (extracted from (a)). The current vanishes around zero magnetic field consistent with spin-orbit mechanism. Red line is a linear fit which serves as guide to the eye.

**Hyperfine mechanism.** Moving an electron through a gradient of a random nuclear field can also drive EDSR. However, the driving strength in this case does not depend on the external magnetic field [15] in contradiction with the data in Fig. 7.6. Furthermore, due to the fluctuations in the nuclear field gradient, and hence in the EDSR driving field, this mechanism is supposed to

prevent the observation of coherent qubit evolution. Indeed, Rabi oscillations were not observed in experiments on hyperfine-mediated EDSR [15]. This is in contrast with the Rabi oscillations observed in this work.

***g*-tensor mechanism.** Electric fields can vary the *g*-tensor, which may lead to a tilt in the spin precession axis and induce the so-called *g*-tensor modulation resonance (*g*-TMR) [14]. In order for this mechanism to work the *g*-factor must be anisotropic, which is indeed the case in our InAs nanowire quantum dots. The effective driving field due to this mechanism vanishes at zero external magnetic field, just as for the spin-orbit mechanism. However, we argue that the microwave fields in our experiment are too weak to drive *g*-TMR.

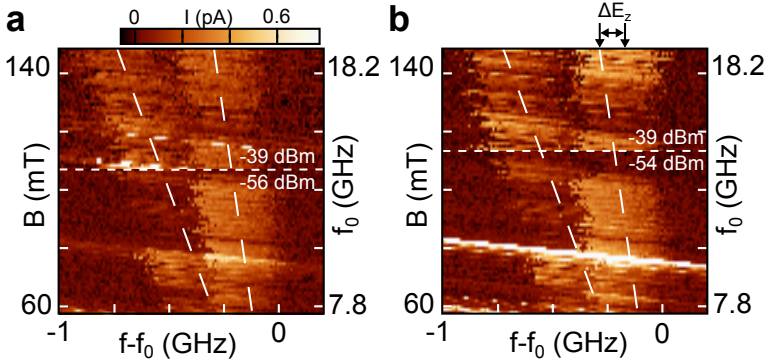


**Figure 7.7:** Splitting of the EDSR line at higher magnetic fields due to a difference between  $g_L$  and  $g_R$  measured for two different gate configurations (panels (a) and (b)). At each field the frequency is swept in a fixed range around  $f_0 = g\mu_B B/h$  calculated using  $g = 9.28$ . The wide dashed lines in both panels correspond to  $g_L$  and  $g_R$  determined for panel (a) and pasted into panel (b). Horizontal small dashed lines separate data sets obtained at different microwave powers (indicated above and below the dashed lines). For the two gate configurations the difference in  $V_4$  is more than 100 mV. The black arrows in panel (b) indicate the upper limit for possible change of the Zeeman energy ( $\Delta E_Z = 0.4 \mu eV$ ).

In order to study the relevance of *g*-TMR for this experiment we try to induce a change in *g*-factor by gate voltages. We estimate the upper bounds on the change of the left and right *g*-factors by measuring the EDSR lines for two sets of gate voltages (Figs. 7.7a and 7.7b). The gate voltage change between the two panels of Fig. 7.7 exceeds the typical gate voltage change due to microwaves by a factor of 10. For the left quantum dot the upper bound on the corresponding change in  $g_L$  is  $\Delta g_L = 0.06$ . (The change in the

EDSR line position in this measurement may originate from dynamical nuclear polarization, not from the  $g$ -factor difference. For this reason an estimate given here is an upper bound.) From this we conclude that at  $B = 100$  mT microwaves can at most produce a change in the Zeeman energy equivalent to a change in the effective magnetic field  $\Delta B = B \cdot \Delta g_L / g_L \approx 0.07$  mT, an order of magnitude smaller than the experimentally observed EDSR driving field. Note that the change in the absolute value of the  $g$ -factor yields predominantly an effective  $\Delta B$  along the  $z$ -direction. The field that drives  $g$ -TMR is orthogonal to  $z$ -axis, and therefore it is even smaller. For the right quantum dot no change in  $g$ -factor is detected between Figs. 7.7a and 7.7b. At the same time the EDSR signal is equally strong for both quantum dots. From this we conclude that while a contribution from  $g$ -TMR cannot be excluded, the strength of this effect is too small to explain the observed EDSR.

**Electron spin resonance.** Spin resonance can be driven by magnetic fields from the a.c. currents flowing through the gates. However, these fields are extremely small and can be neglected here. For the a.c. voltage bias of 1 – 10 mV applied to the gate (Fig. 7.2e) and the measured resistance of the gate contacted on both sides of 5-10 k $\Omega$ , the current is in the microampere range (assuming a gate shorted at the end) and the induced magnetic field is in the  $\mu$ T range. This field is three orders of magnitude smaller than the field that drives the resonance in Fig. 7.1c.

### 7.5.3 LOWER LIMIT MEASUREMENT OF THE RELAXATION TIME

Spin-orbit interaction in combination with electron-phonon coupling is believed to be the dominant mechanism of spin relaxation in quantum dots [9]. So far no measurements of the electron spin relaxation time  $T_1$  were reported in InAs nanowire quantum dots. Measurements in this chapter can probe relaxation on the microsecond timescale, which is 3 orders of magnitude below the theoretically predicted  $T_1$  [34]. However we can put a lower bound on the value of  $T_1$ , as shown in Fig. 7.8. A Rabi experiment is performed with two different delay times between the end of the microwave burst and the readout. The contrast of Rabi oscillations remains unchanged after the qubit is kept in CB for 1  $\mu$ s. This measurement establishes that  $T_1 \gg 1 \mu$ s and rules out the influence of relaxation on the decay of Rabi oscillations. The double dot



current becomes too small for longer pulse cycle times. In the future an exact value of  $T_1$  can be obtained using charge sensing, which can be used to probe relaxation times on timescales as long as few seconds [9].

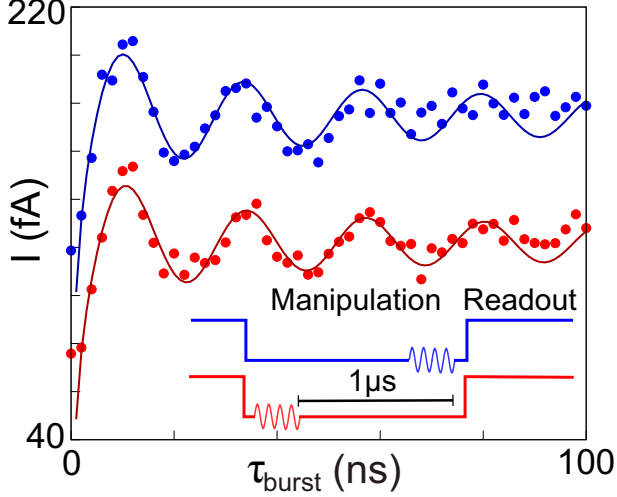


**Figure 7.8:** Rabi oscillations for two different positions of the microwave burst within the manipulation stage with the respective pulse diagrams indicated by the same color. Traces are offset vertically for clarity. The amplitudes of the two traces obtained from the fits are within error bars from each other. In this figure  $B = 102$  mT,  $f = 13$  GHz.

#### 7.5.4 INDEPENDENT CONTROL OF SPIN-ORBIT QUBITS IN TWO QUANTUM DOTS

Fig. 7.9a reveals that current at resonance is not the same for the two EDSR lines even at the same frequency. This indicates that the Rabi frequencies are different for the two qubits, and provides further support for separate qubit addressability. This is clear in the measurement of Rabi oscillations (Fig. 7.9b). The same microwave burst rotates two qubits by different angles. Depending on the driving frequency the left qubit can rotate faster (Fig. 7.9b, upper panel), at equal rate (middle panel) or slower (bottom panel) than the right qubit.

We propose that these variations in Rabi frequencies are because the a.c. electric fields on the left and right dots have non-identical frequency depen-

dencies. At frequencies above 15 GHz the transmission is dominated by sharp resonances at fixed frequency (Fig. 7.9a). These resonances correspond to the modes of the cavity formed by the copper rf shield surrounding the sample. Each mode has a unique spatial distribution of electric fields. Therefore, wires connected to the gates can exhibit different couplings to a particular mode producing different electric fields on the left and right dots.

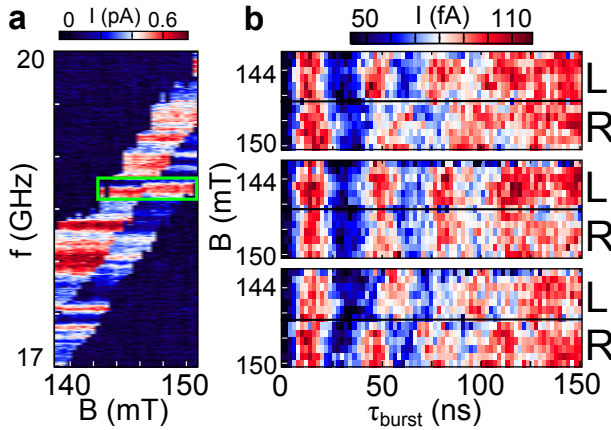


**Figure 7.9:** (a), two EDSR lines that correspond to the left and right qubits (L and R), data taken at  $P = -38$  dBm. The cavity resonance studied in panel (b) is indicated with a green rectangle. (b), Rabi oscillations for a range of magnetic field that spans the EDSR lines for L and R at three values of the driving frequency 18.51 GHz, 18.66 GHz and 18.81 GHz.

### 7.5.5 FIDELITY ESTIMATES

**Readout fidelity.** Even when the double dot is in one of the parallel states, a number of processes may result in the left electron tunneling to the right dot despite spin blockade. These processes include flip-flops with nuclear spins, spin-orbit mediated tunneling, photon-assisted tunneling and phonon-mediated relaxation. Conversely, it is possible that the left electron does not tunnel to the right during the readout stage even when the double dot is in one of the antiparallel states. This can be caused by a weak interdot tunnel coupling. We can reduce the effects of photon-assisted tunneling by slightly lowering the microwave power, without a noticeable reduction in Rabi frequency (see Fig.

7.4). The effect of relaxation is small as estimated in section 7.5.3. However, the effects of spin-orbit and hyperfine interactions, as well as the effect of the finite interdot tunnel coupling, affect the readout fidelity.

We estimate the rates of decay for the (1,1) parallel and antiparallel states,  $\Gamma_P$  and  $\Gamma_{AP}$ , from the double dot d.c. current. At finite field, transport is limited by one of the two parallel states [17]. From  $I(B > 0) \sim 0.1$  pA we extract  $\Gamma_P \sim 0.3$  MHz. At zero field the slowest process in the tunneling from the antiparallel configuration into (0,2). From  $I(B = 0) \sim 1$  pA we estimate  $\Gamma_{AP} \sim 6$  MHz. Using definitions in Ref. [35] these rates correspond to readout fidelities of 70-80 % for the readout time of 150 ns. In the future higher fidelities can be achieved by optimizing the interdot tunnel coupling and suppressing spin-orbit mediated tunneling by properly orienting the external magnetic field [17].

**Initialization fidelity.** For this experiment we used random initialization in one of the two parallel configurations. In the future, initialization in a specific state can be realized by idling the double dot in a nearby charge configuration with a well-defined state (such as the singlet (0,2) state) [27].

**Manipulation fidelity.** Qubit manipulation fidelity is limited by randomly fluctuating fields from the nuclear spin bath. For the r.m.s. hyperfine magnetic field  $B_N \sim 0.7$  mT and the EDSR driving field  $B_{SO} \sim 0.9$  mT we estimate fidelities of  $48 \pm 2\%$  using the model in Ref. [18]. This fidelity qualitatively agrees with the experimentally measured contrast of Rabi oscillations. The amplitude of the first Rabi oscillation is 100-150 fA (Fig. 7.2d) while the transfer of 1 electron per measurement cycle would correspond to the current of 260 fA. This fidelity can be improved in the future by increasing the Rabi frequency ( $B_{SO}$  increases at higher  $B$ , see Eq. 7.1) and by nuclear spin state preparation.

### 7.5.6 POSSIBLE DECOHERENCE MECHANISMS

**Fast nuclear spin bath.** Measurements of  $T_2^*$  and  $T_{echo}$  allow us to estimate the correlation time of the fluctuating environment  $\tau_c = T_{echo}(T_{echo}\sqrt{2}/T_2^*)^2/12 \sim 350$  ns [36]. This correlation time is a factor  $\sim 20$  faster than that reported in the single spin dephasing measurements in GaAs lateral quantum dots [24]. One reason why nuclear field fluctuations can be faster in InAs is the large nuclear spin of indium  $I_{In} = 9/2$  compared to gallium ( $I_{Ga} = 3/2$ ). At  $B =$

100 mT the Zeeman energy difference for an electron greatly exceeds that for nuclei, leading to a suppression of electron-mediated nuclear flip-flops. The dominant mechanisms of nuclear spin dynamics are thus dipole-dipole interaction in the nuclear bath and quadrupole coupling with electric field gradients. Both of these interactions, as well as the corresponding timescales, scale with the square of the nuclear spin. Therefore, simply the ratio of nuclear spins in In versus Ga can account for the order of magnitude shorter correlation time and  $T_{echo}$  in InAs nanowires.

**Paramagnetic impurities.** In principle, fluctuating magnetic fields can come from unpaired electron spins (paramagnetic impurities) residing on the surface of the nanowire or in the substrate. No unambiguous evidence of this effect was observed in our spin blockade measurements on multiple samples, but it cannot be ruled out. Note that, if present, paramagnetic spin fluctuations should not produce fields larger than those induced by the nuclei. Otherwise the zero-field current peak (Fig. 7.1c) should be wider, and the inhomogeneous dephasing time  $T_2^*$  should be shorter. Further investigation is needed in order to determine the relevance of this effect.

**Charge noise.** Charge noise can originate from voltage noise on the gates, gate leakage and charged impurity fluctuations. It leads to random deformations of the double dot confinement which can induce random magnetic fields through spin-orbit interaction,  $g$ -tensor modulation and hyperfine field gradients. Note that in order to be consistent with the observed Hahn echo decay envelope, charge noise must have a non-Markovian character. A simple exponential echo decay is expected for dephasing due to Markovian fluctuations.

Our InAs nanowire devices are optimized for minimal charge noise. The low probability of stacking faults ( $\sim 1$  per micron) ensures that likely no defects are present inside the nanowire. A dielectric layer between the gates and the wire suppresses gate leakage. Voltage noise on the gates is reduced by electrical filtering in the cryostat. Occasionally, low frequency charge switching is observed, but it can be suppressed by fine-tuning the gate voltages. The relevance of high frequency charge noise to dephasing is discussed below.

Spin-orbit interaction in combination with charge noise can produce a random field  $B_{SO}$ . However, in quantum dots linear-in- $\mathbf{k}$  terms of spin-orbit interaction *do not* lead to  $B_{SO}$  in the  $z$ -direction [22]. Therefore these terms *cannot* induce dephasing. Only higher order spin-orbit terms, such as cubic terms, can lead to dephasing in combination with charge noise. Little is known about the

strength of cubic spin-orbit terms in InAs nanowires. As an upper estimate, we assume that  $B_{SO} \sim 1$  mT responsible for Rabi oscillations comes entirely from cubic spin-orbit terms. The lower bound on magnetic field fluctuations can be estimated as  $\Delta B \sim h/(g\mu_B T_{echo}) = B_{SO}/(2 \cdot T_{echo} \cdot f_R) \sim 50 - 100$   $\mu$ T during the time of order  $T_{echo}$ . The corresponding charge noise would be equivalent to  $\sim 1/10$  of the a.c. gate voltage that drives EDSR. But no blurring of bias triangles on such scales is observed when microwaves are off, which strongly indicates that charge noise of the magnitude needed to explain dephasing in this way does not occur.

By similar arguments,  $g$ -tensor modulation is also too weak to induce the observed dephasing. Estimates in section 2.3 show that a very large gate voltage change ( $\sim 100$  mV) is required to change the effective field by 100  $\mu$ T through  $g$ -factor modulation. Charge fluctuations can also shift the dot through a gradient of hyperfine field. Given the r.m.s. hyperfine field  $B_N \sim 0.7$  mT, a dot must be displaced by  $\sim 1/10$  of its size, or by 1.5 nm, in order to experience a gradient of  $\Delta B \sim 50$   $\mu$ T. Such displacement is required to drive EDSR itself, and it considerably blurs the bias triangles (Fig. 7.5).

Finally, our microwave circuit is designed such that the square voltage pulses do not have slopes that can induce nanometer dot displacements on 100 ns timescales. In addition, all wires in the cryostat carefully filtered against noise from room temperature electronics. Thus electrical noise on the gates can be excluded from the discussion of dephasing rates at the present level.

This work has been done in collaboration with S. M. Frolov, E. P. A. M. Bakkers and L. P. Kouwenhoven.

We thank K. Nowack, R. Schouten, M. Laforest, K. Zuo, M. Hocevar, R. Algra, J. van Tilburg, M. Scheffler, G. de Lange, V. Dobrovitski, J. Danon, R. Hanson, R. Liu, Yu. V. Nazarov and L. Vandersypen for their help. This work has been supported by NWO/FOM Netherlands Organization for Scientific Research and through the DARPA program QUEST.

## REFERENCES

- [1] S. Datta and B. Das, *Electronic Analog of the Electrooptic Modulator*, Applied Physics Letters **82**, 1887 (2003).

- 
- [2] K. C. Nowack, F. H. L. Koppens, Y. V. Nazarov, and L. M. K. Vandersypen, *Coherent Control of a Single Electron Spin with Electric Fields*, *Science* **318**, 1430 (2007).
- [3] C. Fasth, A. Fuhrer, L. Samuelson, V. N. Golovach, and D. Loss, *Direct Measurement of the Spin-Orbit Interaction in a Two-Electron InAs Nanowire Quantum Dot*, *Phys. Rev. Lett.* **98**, 266801 (2007).
- [4] A. Pfund, I. Shorubalko, K. Ensslin, and R. Leturcq, *Spin-state mixing in InAs double quantum dots*, *Phys. Rev. B* **76**, 161308 (2007).
- [5] E. D. Minot, F. Kelkensberg, M. van Kouwen, J. A. van Dam, L. P. Kouwenhoven, V. Zwiller, M. T. Borgström, O. Wunnicke, M. A. Verheijen, and E. P. A. M. Bakkers, *Single Quantum Dot Nanowire LEDs*, *Nano Lett.* **7**, 367 (2007).
- [6] M. H. M. van Weert, N. Akopian, U. Perinetti, M. P. van Kouwen, R. E. Algra, M. A. Verheijen, E. P. A. M. Bakkers, L. P. Kouwenhoven, and V. Zwiller, *Selective Excitation and Detection of Spin States in a Single Nanowire Quantum Dot*, *Nano Letters* **9**, 1989 (2009).
- [7] S. Nadj-Perge, S. M. Frolov, J. W. W. van Tilburg, J. Danon, Y. V. Nazarov, R. Algra, E. P. A. M. Bakkers, and L. P. Kouwenhoven, *Disentangling the effects of spin-orbit and hyperfine interactions on spin blockade*, *Phys. Rev. B* **81**, 201305 (2010).
- [8] M. Pioro-Ladriere, T. Obata, Y. Tokura, Y. Shin, T. Kubo, K. Yoshida, T. Taniyama, and S. Tarucha, *Electrically driven single-electron spin resonance in a slanting Zeeman field*, *Nature Physics* **4**, 776 (2008).
- [9] R. Hanson, L. P. Kouwenhoven, J. R. Petta, S. Tarucha, and L. M. K. Vandersypen, *Spins in few-electron quantum dots*, *Rev. Mod. Phys.* **79**, 1217 (2007).
- [10] A. Pfund, I. Shorubalko, K. Ensslin, and R. Leturcq, *Suppression of Spin Relaxation in an InAs Nanowire Double Quantum Dot*, *Phys. Rev. Lett.* **99**, 036801 (2007).
- [11] F. H. L. Koppens, J. A. Folk, J. M. Elzerman, R. Hanson, L. H. Willems van Beveren, I. T. Vink, H.-P. Tranitz, W. Wegscheider, L. P.

- Kouwenhoven, and L. M. K. Vandersypen, *Control and Detection of Singlet-Triplet Mixing in a Random Nuclear Field*, *Science* **309**, 1246 (2005).
- [12] A. C. Johnson, J. R. Petta, J. M. Taylor, A. Yacoby, M. D. Lukin, C. M. Marcus, M. P. Hanson, and A. C. Gossard, *Triplet-singlet spin relaxation via nuclei in a double quantum dot*, *Nature* **435**, 925 (2005).
- [13] E. I. Rashba and A. L. Efros, *Orbital Mechanisms of Electron-Spin Manipulation by an Electric Field*, *Phys. Rev. Lett.* **91**, 126405 (2003).
- [14] Y. Kato, R. C. Myers, D. C. Driscoll, A. C. Gossard, J. Levy, and D. D. Awschalom, *Gigahertz Electron Spin Manipulation Using Voltage-Controlled  $g$ -Tensor Modulation*, *Science* **299**, 1201 (2003).
- [15] E. A. Laird, C. Barthel, E. I. Rashba, C. M. Marcus, M. P. Hanson, and A. C. Gossard, *Hyperfine-Mediated Gate-Driven Electron Spin Resonance*, *Phys. Rev. Lett.* **99**, 246601 (2007).
- [16] V. N. Golovach, M. Borhani, and D. Loss, *Electric Dipole Induced Spin Resonance in Quantum Dots*, *Phys. Rev. B* **74**, 165319 (2006).
- [17] J. Danon and Y. V. Nazarov, *Pauli spin blockade in the presence of strong spin-orbit coupling*, *Phys. Rev. B* **80**, 041301 (2009).
- [18] F. H. L. Koppens, C. Buizert, K.-J. Tielrooij, I. T. Vink, K. C. Nowack, L. P. Meunier, T. Kouwenhoven, and L. M. K. Vandersypen, *Driven coherent oscillations of a single electron spin in a quantum dot*, *Nature* **442**, 776 (2006).
- [19] C. E. Pryor and M. E. Flatté, *Landé  $g$  Factors and Orbital Momentum Quenching in Semiconductor Quantum Dots*, *Phys. Rev. Lett.* **96**, 026804 (2006).
- [20] F. Koppens, D. Klauser, W. Coish, K. Nowack, L. Kouwenhoven, D. Loss, and L. Vandersypen, *Universal phase shift and nonexponential decay of driven single-spin oscillations*, *Phys. Rev. Lett.* **99**, 106803 (2007).
- [21] J. Berezovsky, M. H. Mikkelsen, N. G. Stoltz, L. A. Coldren, and D. D. Awschalom, *Picosecond Coherent Optical Manipulation of a Single Electron Spin in a Quantum Dot*, *Science* **320**, 349 (2008).

- 
- [22] V. N. Golovach, M. Borhani, and D. Loss, *Electric-dipole-induced spin resonance in quantum dots*, Phys. Rev. B **74**, 165319 (2006).
- [23] T. Obata, M. Pioro-Ladrière, Y. Tokura, Y.-S. Shin, T. Kubo, K. Yoshida, T. Taniyama, and S. Tarucha, *Coherent manipulation of individual electron spin in a double quantum dot integrated with a micromagnet*, Phys. Rev. B **81**, 085317 (2010).
- [24] F. H. L. Koppens, K. C. Nowack, and L. M. K. Vandersypen, *Spin Echo of a Single Electron Spin in a Quantum Dot*, Phys. Rev. Lett. **100**, 236802 (pages 4) (2008).
- [25] D. Press, T. D. Ladd, B. Y. Zhang, and Y. Yamamoto, *Complete quantum control of a single quantum dot spin using ultrafast optical pulses*, Nature **456**, 218 (2008).
- [26] S. Foletti, H. Bluhm, D. Mahalu, V. Umansky, and A. Yacoby, *Universal quantum control of two-electron spin quantum bits using dynamic nuclear polarization*, Nature Phys. **5**, 903 (2009).
- [27] J. R. Petta, A. C. Johnson, J. M. Taylor, E. A. Laird, A. Yacoby, M. D. Lukin, C. M. Marcus, M. P. Hanson, and A. C. Gossard, *Coherent Manipulation of Coupled Electron Spins in Semiconductor Quantum Dots*, Science **309**, 2180 (2005).
- [28] H. Bluhm, S. Foletti, I. Neder, M. Rudner, D. Mahalu, V. Umansky, and A. Yacoby, *Long coherence of electron spins coupled to a nuclear spin bath*, ArXiv e-prints (2010), 1005.2995.
- [29] C. Barthel, J. Medford, C. M. Marcus, M. P. Hanson, and A. C. Gossard, *Interlaced Dynamical Decoupling and Coherent Operation of a Singlet-Triplet Qubit*, ArXiv e-prints (2010), 1007.4255.
- [30] D. Reilly, J. Taylor, J. Petta, C. Marcus, M. Hanson, and A. Gossard, *Suppressing Spin Qubit Dephasing by Nuclear State Preparation*, Science **321**, 817 (2008).
- [31] G. D. Fuchs, V. Dobrovitski, D. M. Toyli, F. J. Heremans, and D. D. Awschalom, *Gigahertz Dynamics of a strongly Driven Single Quantum Spin*, Science **326**, 1520 (2009).



- [32] A. De and C. E. Pryor, *Predicted band structures of III-V semiconductors in the wurtzite phase*, Phys. Rev. B **81**, 155210 (2010).
- [33] F. H. L. Koppens, C. Buizert, I. T. Vink, K. C. Nowack, T. Meunier, L. P. Kouwenhoven, and L. M. K. Vandersypen, *Detection of a single electron spin resonance in a double quantum dot*, Journal of Applied Physics **101**, 081706 (2007).
- [34] M. Trif, V. N. Golovach, and D. Loss, *Spin dynamics in InAs nanowire quantum dots coupled to a transmission line*, Phys. Rev. B **77**, 045434 (2008).
- [35] J. M. Elzerman, R. Hanson, L. H. Willems van Beveren, B. Witkamp, L. M. K. Vandersypen, and L. P. Kouwenhoven, *Single-shot read-out of an individual electron spin in a quantum dot*, Nature **430**, 431 (2004).
- [36] C. P. Slichter, *Principles of Magnetic Resonance*, 3rd ed. (Springer-Verlag, Berlin, 1990).

# CONCLUSIONS AND FUTURE DIRECTIONS

## 8.1 CURRENT STATUS

The field of electron spin qubits was pioneered in lateral quantum dots in GaAs 2DEGs. Experimentally, both single-spin rotations and two-qubit SWAP-gate had been demonstrated [1, 2]. In the meantime, the idea of realizing electron spin qubits in different material systems has emerged. The choice of materials is mainly driven by the problems observed in GaAs spin qubits. For example, nuclear spins have been identified as the main source of decoherence, dephasing electron spin in tens of nanoseconds. To overcome this limitation most scientific efforts have been invested into the realization of qubits in materials without nuclear spin, *e.g.* carbon and silicon. Although some experimental progress in the readout of spin states has recently been made [3–5], the demonstration of coherent manipulation of single spins in these materials is still lacking.

Besides extending coherence time, one can also try to make coherent control faster since the figure of merit is the ratio between coherence time and time required for a  $\pi$  rotation of a qubit. More specifically, one can use a material with strong spin-orbit coupling in which fast control can be realized with elec-

tric fields. Single quantum dots containing only a single electron were recently realized in a strong spin-orbit material, InAs nanowires, by the Lund group [6]. Moreover, spin blockade was observed in many-electron double quantum dots by the ETH group [7, 8]. This motivated us to implement coherent spin control in InAs nanowires and lead us to study several interesting effects in quantum dots caused by strong spin-orbit interaction in InAs nanowires.

The experimental results presented in this thesis can be summarized as follows:

- The  $g$ -factor anisotropy is measured for a single electron spin. The  $g$ -factor is approximately 20% smaller when the external field is aligned with the nanowire than when the field is applied perpendicular to the nanowire (Chapter 4).
- Double quantum dots tunable to the few-electron regime are realized. This allows a careful study of spin-orbit and hyperfine effects in a two-electron double dot. Large spin-orbit interaction couples spin and orbital degrees of freedom, thus enabling transitions between  $T_{11}$  and  $S_{02}$  states. This can drastically modify spin blockade (Chapter 5).
- The effects of spin-orbit coupling on spin-blockade can be suppressed to a large extent by changing the direction of a magnetic field and aligning it with the direction of the  $\mathbf{t}_{\text{SO}}$  vector (Chapter 6).
- Spin-orbit qubits in an InAs nanowire are realized. Rotations of spin-orbit qubits around arbitrary axis to any predefined superposition state are achieved by using electric-dipole spin resonance. The fastest  $\pi$  rotation is performed in 8 ns, which is an order of magnitude improvement over previous realizations (Chapter 7).
- The measured spin dephasing time  $T_2^* \approx 8$  ns is likely caused by the randomly fluctuating nuclear spin bath. The coherence time was extended to  $\sim 200$  ns using dynamical decoupling techniques (Chapter 7).

## 8.2 SHORT-TERM GOALS

This section discusses open questions which will be addressed in the near future.

### 8.2.1 REALIZATION OF A TWO-QUBIT GATE

To complete the set of requirements for quantum computation, an entangling two-qubit gate is needed [9]. In lateral quantum dots in GaAs, such a  $\sqrt{\text{SWAP}}$  gate has been realized by carefully controlling the exchange interaction between two neighboring spins. The time needed for this operation was 180 ps [2]. It was recently suggested that a quantum control-phase gate (C-Phase) can be performed when there is a difference in Zeeman energy between the two dots [10]. This gate is particularly suited for InAs nanowires due to the presence of a difference in the  $g$ -factors in the two dots (observed in the present work, see chapter 7). The realization of the C-Phase gate would eventually enable implementation of some advanced quantum algorithms, such as quantum Fourier transform, more efficiently than using the  $\sqrt{\text{SWAP}}$  gate [9, 10].

### 8.2.2 SINGLE-SHOT READOUT AND MEASUREMENT OF THE RELAXATION TIME

Another necessary requirement for quantum computation is the readout of single spin-orbit eigenstates [11]. Furthermore, in order to explore entanglement of qubit states single-shot readout is needed [12]. Single-shot readout of spin has been demonstrated in GaAs 2DEG [13] and in silicon [3]. The main requirement for a single-shot readout is the fabrication of a nearby charge sensor. Charge sensing has already been demonstrated in devices with an one-dimensional geometry by capacitively coupling a quantum dot to a single electron transistor [14], to another nearby quantum dot [4, 15] or to a quantum point contact. The last of these schemes was realized in InAs nanowires [16]. However, in this particular scheme the quantum point contact was realized in a 2D electron gas located below the nanowire, and this approach is difficult to combine with our bottom gate device design. But the first two schemes, *i.e.* a single electron transistor and a quantum dot, are compatible with bottom gate devices and should be straightforward to implement.

The readout of spin-orbit eigenstates is also required for measurement of the relaxation time  $T_1$  in order to fully characterize our qubit. Measurements in chapter 7 only gave a lower bound on the relaxation time ( $T_1 \gg 1 \mu\text{s}$ ), consistent with theoretical predictions of a  $T_1$  that should be  $\sim 1 \text{ ms}$  [17]. A more precise estimate was not possible in the experiment, since a measurement of the relaxation time requires the duration of the cycle of loading and

unloading electrons to be of the order of  $T_1$ . For cycle duration longer than  $\sim 1\ \mu\text{s}$  current becomes too small to be measured. To be able to make the measurement cycle longer and obtain better estimate of  $T_1$ , a charge sensor has to be used.

### 8.2.3 CONTROL OVER THE NUCLEAR SPIN BATH

It was shown that the preparation of the state of the nuclear spin bath in lateral double quantum dots in GaAs can improve the dephasing time considerably [18–20]. In InAs nanowires, it is also important to gain control over nuclear spins and to enhance dephasing times. At the moment, it is not clear whether the exact same schemes can lead to improved dephasing times in InAs nanowires. The nanowire geometry, strong spin-orbit interaction and possible faster relaxation of indium nuclear spins are the key differences between the GaAs 2DEG and the InAs nanowire. These differences can play an important role in defining the efficiency of control over the nuclear spin bath. The nanowire geometry may be important for the dynamics of nuclear spins, due to its finite size (a  $1\ \mu\text{m}$  long nanowire contains  $\sim 10^8$  nuclear spins). The interplay between spin-orbit and hyperfine effects may affect the nuclear spin bath. In spin blockade current can exhibit bistable levels and hysteretic behavior. These effects are likely related to the dynamics of the nuclear spin bath [7]. The quadrupole coupling of indium nuclear spins to electric field gradients affects the energy levels in the nuclear spin bath. Inhomogeneous quadrupole coupling can suppress nuclear flip-flops and hence suppress spin diffusion [21]. On the other hand quadrupole coupling also facilitates fast nuclear spin relaxation [22]. For all these reasons it is expected that the nuclear spin dynamics in InAs nanowires is different from the already studied nuclear spin dynamics in GaAs systems. Therefore, control of the nuclear spin bath remains an interesting challenge.

### 8.2.4 SPIN-ORBIT QUBITS IN INSB NANOWIRES

A promising material with even stronger spin-orbit coupling than InAs is indium antimonide (InSb). In many ways InSb is similar to InAs: it is a small band gap material with a small effective mass ( $\sim 0.015m_e$ ) and a large  $g$ -factor ( $\sim 50$ ). The small effective mass is important for realizing few-electron quantum dots. Similarly as for InAs, differences in  $g$ -factor can be used to se-

lectively address spins in a double quantum dot. Spin-orbit interaction in InSb is expected to be 5-10 times larger than in InAs [23]. Importantly, few-electron single quantum dots in InSb nanowires have recently been demonstrated [24]. Although Sb has a nuclear spin  $5/2$  which is larger than As ( $3/2$ ), it is reasonable to expect that the nuclear spin bath will still be dominated by In spins. Therefore, it is likely that in InSb nanowires faster coherent control can be achieved, while the dephasing time would remain the same as in InAs.

### 8.3 QUBITS IN NANOWIRES - OUTLOOK

The unique aspect of nanowires is the flexibility in choosing their composition. In the future this property may be used for integration of electrically defined quantum dots with optically active dots. Both types of dots have been demonstrated in nanowires [25–27]. Interesting prospect is to realize both types of dots in a *single nanowire*, and to use this geometry to couple spin qubits to light. This would enable long-distance transfer of the qubit state using photon polarization. Additionally, using materials such as indium-arsenide-phosphide (InAsP) or indium-gallium-nitride (InGaN), the band gap and thus the frequency of emitted photons can be tuned in a wide range ( $\sim 0.3 - 3$  eV). Therefore, in principle, it is also possible to couple quantum dots in nanowires to other optical emitters, such as NV-centers in diamond or Rb atoms.

A completely different direction is to find materials that are the most suitable for single spin control and therefore also good starting point for implementation of simple quantum algorithms. As mentioned the nuclear spin bath is identified as the main source of decoherence for electron spin. Therefore materials without nuclear spin, such as silicon and germanium, would be suitable for storing the spin state for a long time. In fact, the hole states in Ge/Si core-shell nanowires are already promising candidate for hosting spin qubits [15]. Interestingly, manipulation with electric fields could be also possible in these wires since the spin-orbit interaction for holes is strong ( $l_{SO} \sim 50$  nm [28]). The challenge, due to high effective mass of holes ( $\sim 0.2m_e$ ), is to isolate a single hole in a quantum dot. However, this problem might be solved by using charge sensing techniques or by creating qubits in quantum dots that are not operated in a few-hole regime.

Let us note that small bandgap materials like lead telluride (PbTe) and lead selenide (PbSe) may also be suitable for nanowire qubits. Both materials have

a small effective mass for electrons ( $\lesssim 0.1m_e$ ) and can be grown as nanowires [29, 30]. It is therefore reasonable to expect that few-electron quantum dots can be realized in these materials. Importantly, Pb, Te and Se have zero nuclear spin. In addition, spin-orbit interaction in these nanowires is strong and the  $g$ -factors are large. However, before using these nanowires for qubits, challenges related to understanding of the band structure of these materials and nanowire quality need to be addressed.

To summarize, it is still an open question which material is the most promising for spin manipulation. Besides the strength of spin-orbit coupling and the absence or presence of nuclear spins, many other factors play an important role; *e.g.* effective mass, charge noise, impurities and disorder. All these aspects need to be addressed in order to be able to reproducibly create quantum dots containing a single spin. In addition, the role of band structure properties, such as valley degeneracy, present in many material systems, still needs to be explored in order to decide on the suitability of certain materials for spin qubits.

To conclude, the field of semiconductor nanowires is still rapidly developing. It is reasonable to expect that various technical problems will be solved in the future and many new interesting ideas involving the use of nanowires for quantum information processing will emerge. Therefore, it is safe to say that the most exciting nanowire-spin-orbit-qubit experiments are still ahead of us.

## REFERENCES

- [1] F. H. L. Koppens, C. Buizert, K. J. Tielrooij, I. T. Vink, K. C. Nowack, T. Meunier, L. P. Kouwenhoven, and L. M. K. Vandersypen, *Nature* **442**, 776 (2006).
- [2] J. R. Petta, A. C. Johnson, J. M. Taylor, E. A. Laird, A. Yacoby, M. D. Lukin, C. M. Marcus, M. P. Hanson, and A. C. Gossard, *Coherent Manipulation of Coupled Electron Spins in Semiconductor Quantum Dots*, *Science* **309**, 2180 (2005).
- [3] Morello, A. et al., *Single-shot readout of an electron spin in silicon*, *Nature* **467**, 687 (2010).

- 
- [4] H. O. H. Churchill, F. Kuemmeth, J. W. Harlow, A. J. Bestwick, E. I. Rashba, K. Flensberg, C. H. Stwertka, T. Taychatanapat, S. K. Watson, and C. M. Marcus, *Phys. Rev. Lett.* **102**, 166802 (2009).
- [5] M. Thalakulam, C. B. Simmons, B. J. Van Bael, B. M. Rosemeyer, D. E. Savage, M. G. Lagally, M. Friesen, S. N. Coppersmith, and M. A. Eriksson, *Single-shot measurement and tunnel-rate spectroscopy of a Si/SiGe few-electron quantum dot*, ArXiv e-prints (2010), 1010.0972.
- [6] C. A. Fasth, A. Fuhrer, L. Samuelson, V. N. Golovach, and D. Loss, *Phys. Rev. Lett.* **98**, 266801 (2007).
- [7] A. Pfund, I. Shorubalko, K. Ensslin, and R. Leturcq, *Suppression of Spin Relaxation in an InAs Nanowire Double Quantum Dot*, *Phys. Rev. Lett.* **99**, 036801 (2007).
- [8] A. Pfund, I. Shorubalko, K. Ensslin, and R. Leturcq, *Spin-state mixing in InAs double quantum dots*, *Phys. Rev. B* **76**, 161308 (2007).
- [9] M. Nielsen and I. Chuang, *Quantum computation and information* (Cambridge University Press, Cambridge, UK, 2000).
- [10] T. Meunier, V. E. Calado, and L. M. K. Vandersypen, *Efficient C-Phase gate for single-spin qubits in quantum dots*, ArXiv e-prints (2010), 1010.0164.
- [11] D. DiVincenzo, *The physical implementation of quantum computation*, *Fortschr. Phys.* **48**, 771 (2000).
- [12] K. C. Nowack, Ph.D. thesis, Delft University of Technology (2009).
- [13] J. M. Elzerman, R. Hanson, L. H. Willems van Beveren, B. Witkamp, L. M. K. Vandersypen, and L. P. Kouwenhoven, *Single-shot read-out of an individual electron spin in a quantum dot*, *Nature* **430**, 431 (2004).
- [14] G. Oetz, G. A. Steele, W.-J. Vos, and L. P. Kouwenhoven, *Real Time Electron Tunneling and Pulse Spectroscopy in Carbon Nanotube Quantum Dots*, *Nano Letters* **8**, 4039 (2008).
- [15] Y. Hu, H. Churchill, D. Reilly, J. Xiang, C. Lieber, and C. Marcus, *A Ge/Si heterostructure nanowire-based double quantum dot with integrated charge sensor*, *Nature Nanotechnology* **2**, 622 (2007).



- [16] I. Shorubalko, R. Leturcq, A. Pfund, D. Tyndall, R. Krischek, S. Schon, and K. Ensslin, *Self-Aligned Charge Read-Out for InAs Nanowire Quantum Dots*, Nano Letters **8**, 382 (2008).
- [17] M. Trif, V. N. Golovach, and D. Loss, *Spin dynamics in InAs nanowire quantum dots coupled to a transmission line*, Phys. Rev. B **77**, 045434 (2008).
- [18] D. Reilly, J. Taylor, J. Petta, C. Marcus, M. Hanson, and A. Gossard, *Suppressing Spin Qubit Dephasing by Nuclear State Preparation*, Science **321**, 817 (2008).
- [19] H. Bluhm, S. Foletti, D. Mahalu, V. Umansky, and A. Yacoby, *Enhancing the Coherence of a Spin Qubit by Operating it as a Feedback Loop That Controls its Nuclear Spin Bath*, Phys. Rev. Lett. **105**, 216803 (2010).
- [20] H. Bluhm, S. Foletti, I. Neder, M. Rudner, D. Mahalu, V. Umansky, and A. Yacoby, *Long coherence of electron spins coupled to a nuclear spin bath*, ArXiv e-prints (2010), 1005.2995.
- [21] C. P. Slichter, *Principles of Magnetic Resonance, 3rd ed.* (Springer-Verlag, Berlin, 1990).
- [22] C. Deng and X. Hu, *Selective dynamic nuclear spin polarization in a spin-blocked double dot*, Phys. Rev. B **71**, 033307 (2005).
- [23] R. Winkler, *Spin-Orbit Coupling Effects in Two-Dimensional Electron and Hole Systems* (Springer-Verlag, 2003).
- [24] H. A. Nilsson, P. Caroff, C. Thelander, M. Larsson, J. B. Wagner, L.-E. Wernersson, L. Samuelson, and H. Q. Xu, *Giant, Level-Dependent  $g$  Factors in InSb Nanowire Quantum Dots*, Nano Letters **9**, 3151 (2009).
- [25] M. H. M. van Weert, N. Akopian, U. Perinetti, M. P. van Kouwen, R. E. Algra, M. A. Verheijen, E. P. A. M. Bakkers, L. P. Kouwenhoven, and V. Zwiller, *Selective Excitation and Detection of Spin States in a Single Nanowire Quantum Dot*, Nano Letters **9**, 1989 (2009).

- [26] E. D. Minot, F. Kelkensberg, M. van Kouwen, J. A. van Dam, L. P. Kouwenhoven, V. Zwiller, M. T. Borgström, O. Wunnicke, M. A. Verheijen, and E. P. A. M. Bakkers, *Single Quantum Dot Nanowire LEDs*, Nano Lett. **7**, 367 (2007).
- [27] M. van Kouwen, Ph.D. thesis, Delft University of Technology (2010).
- [28] X.-J. Hao, T. Tu, G. Cao, C. Zhou, H.-O. Li, G.-C. Guo, W. Y. Fung, Z. Ji, G.-P. Guo, and W. Lu, *Strong and Tunable Spin-Orbit Coupling of One-Dimensional Holes in Ge/Si Core/Shell Nanowires*, Nano Letters **10**, 2956 (2010).
- [29] G. Tai, B. Zhou, and W. Guo, *Structural Characterization and Thermoelectric Transport Properties of Uniform Single-Crystalline Lead Telluride Nanowires*, The Journal of Physical Chemistry C **112**, 11314 (2008).
- [30] M. J. Bierman, Y. K. A. Lau, and S. Jin, *Hyperbranched PbS and PbSe Nanowires and the Effect of Hydrogen Gas on Their Synthesis*, Nano Letters **7**, 2907 (2007).



# SUMMARY

In this thesis the properties of single electron spins are studied by trapping the spins in a small electrostatically defined box, a quantum dot. The dimensions of a quantum dot are typically tens of nanometers, comparable to the wavelength of an electron. The quantum dots, also called artificial atoms, can be fully engineered and thus provide a toolkit for studying quantum mechanics and spin physics. Additional motivation for this research lies in the prospect of using the spin degree of freedom of an electron as a quantum bit, the computational unit of a quantum computer. The quantum dots studied here, are made inside a semiconductor InAs nanowire. This material is particularly interesting since the electron spin inside the quantum dot is strongly coupled to the motion of the electron. Electron spin can be fully controlled by simply moving an electron back and forth between the gated sections inside the nanowire.

Following a general introductory chapter, the second chapter introduces basic theoretical concepts related to this research. First, we discuss the general properties of quantum dots and outline the idea of using electron spin for quantum computation. Spin-orbit and hyperfine interactions, relevant for spins in InAs nanowires, are introduced. Finally, we briefly discuss how these interaction may lead to decoherence of electron spin and affect the readout of spin states.

The third chapter explains nanowire growth, sample fabrication and other experimental techniques used in this research.

In the fourth chapter we studied the simplest case of a single electron trapped in a single quantum dot. We measured the energy spectrum, corresponding to the spin-up and spin-down states of a single electron, as function of a magnetic field. The energy difference between spin states, called Zeeman energy, is modified by confinement. Furthermore, we show that this energy depends strongly on the direction of the applied magnetic field.

Next, we combine two quantum dots in a more advanced double quantum dot configuration. The two dots can be depleted from the electrons which

allows control over the total electron number. We focus on the two-electron states for which some transitions are energetically possible, but forbidden by the Pauli exclusion principle. This is called Pauli spin blockade and can be used for readout of spin. Readout is affected by the interactions between electron spins and the environment. The two interactions, hyperfine and spin-orbit, may randomly flip the spin in one of the dots limiting thus fidelity of the readout. Since our double dot is fully tunable we could study regimes in which spin-flips occur due spin orbit as well as regimes where hyperfine interaction is dominant spin-flip mechanism. This allows careful characterization of the two interactions.

In the sixth chapter, further understanding is obtained by changing the orientation of the applied magnetic field. Interestingly, for certain field orientations, the effects of spin-orbit interaction on spin blockade can be fully suppressed.

Finally, in seventh chapter we demonstrate spin-orbit quantum bits (qubits) implemented in InAs nanowires. Spin-orbit interaction in these nanowires is so strong that spin and electron motion can no longer be separated. We realize fast qubit rotations and universal single qubit control using electric fields to move electrons back and forth inside the dot. Electron motion causes a spin to precess from being 'spin-down' to 'spin-up' reaching the highest frequency of  $\sim 60$  MHz. In the Ramsey experiment, we measured how fast information of the phase of the superposition state decays. The decay time of 8 ns suggests that hyperfine interaction is the main source of decoherence. Coherence time can be extended to  $\sim 200$  ns by dynamical decoupling techniques. Additionally, a difference in Zeeman energies, caused by the different size of two quantum dots, can be used to selectively address the two qubits with gigahertz electric fields.

The work presented in this thesis shows that nanowires offer new possibilities for studying single spins in quantum dots. Specially, the demonstration of a nanowire qubit opens ways to harness the advantages of nanowires for use in quantum computing. Nanowires can serve as one-dimensional templates for scalable qubit registers. Unique to nanowires is the possibility to easily vary the material during wire growth. Such flexibility can be used for future experiments to design wires with suppressed decoherence and push semiconductor qubit fidelities towards error-correction levels. Furthermore, electrical dots can be integrated with optical dots in p-n junction nanowires. Already, the

coherence times achieved here are sufficient for the conversion of an electronic qubit into a photon, a flying qubit, for long-distance quantum communication.

Stevan Nadj-Perge  
November 2010



# SAMENVATTING

In dit proefschrift worden de eigenschappen van de spin van enkele elektronen bestudeerd, door de elektronen op te sluiten in een klein, met elektrische velden gemaakt doosje. Dit noemen we een quantum dot en wordt ook wel een kunstmatig atoom genoemd. Typische afmetingen van een quantum dot zijn tientallen nanometers, vergelijkbaar met de golflengte van een elektron. De fabricage van quantum dots is goed onder controle en ze zijn een ideaal model voor het bestuderen van quantum mechanica en spin fysica. Een andere motivatie voor het onderzoek aan electron spins, is quantum rekenen. De spin van een enkel elektron kan gebruikt worden als een quantum bit (qubit), de rekeneenheid van een quantum computer. The quantum dots in dit proefschrift zijn gevormd in een halfgeleidende InAs nanodraad. Dit materiaal is in het bijzonder interessant omdat de spin van het elektron in de quantum dot sterk gekoppeld is aan de beweging (baan) van het elektron. De spin van het elektron kan veranderd worden door het elektron op en neer te bewegen tussen verschillende delen in de nanodraad.

Het eerste hoofdstuk is een algemene introductie.

In het tweede hoofdstuk worden de theoretische concepten behandeld die aan de grondslag liggen van dit onderzoek. We beginnen met de algemene eigenschappen van quantum dots en presenteren de mogelijkheden die het elektron spin biedt voor quantum rekenen. Spin-baan en kernspin wisselwerking, belangrijk voor spins in InAs nanodraden, worden hier ook geïntroduceerd. Ten slotte behandelen we hoe deze wisselwerkingen kunnen leiden tot decoherentie (verval) van een elektron spin en het effect op het uitlezen van een elektron spin.

In het derde hoofdstuk behandelen we de groei van de nanodraden, het fabriceren van het sample en andere experimentele technieken gebruikt in dit onderzoek.

In het vierde hoofdstuk bestuderen we een enkel elektron opgesloten in een enkele quantum dot. We meten het energie spectrum van de spin-op en spin-neer toestanden van dit elektron als een functie van het magnetische veld. Het



energie verschil tussen deze twee toestanden (Zeeman energie) wordt beïnvloed door de opsluiting. We laten zien dat dit energie verschil ook sterk beïnvloed wordt door de richting waarin het magnetische veld wordt aangelegd.

In het vijfde hoofdstuk presenteren we twee gekoppelde quantum dots. Alle elektronen kunnen uit de dots worden verwijderd, we hebben controle over het totaal aantal elektronen aanwezig in de quantum dots. We bestuderen de twee-elektron toestanden, voor welke sommige transitie mogelijk zijn, maar verboden door het Pauli-uitsluitings principe. Dit wordt ook wel Pauli spin blockade genoemd en kan gebruikt worden om de spin van het elektron uit te lezen. De uitlezing van een elektron spin wordt beïnvloed door interacties tussen elektron spins en hun omgeving. Kernspin en spin-baan interactie kunnen de spin in een van de dots willekeurig laten omklappen. Dit vormt een beperking op de zuiverheid van de uitlezing. Omdat we een uitstekende controle hebben over de dubbele quantum dot kunnen we gebieden onderzoeken waar spin-flips voornamelijk optreden vanwege spin-baan wisselwerking, alsmede gebieden waar de kern spin wisselwerking het dominante spin-flip mechanisme is. Dit maakt een nauwgezette karakterisatie van beide wisselwerkingen mogelijk.

In het zesde hoofdstuk gaan we dieper in op spin-baan en kernspin wisselwerking, door deze te bestuderen als functie van de richting waarin het magnetische veld wordt aangelegd. Bij sommige richtingen van het magnetische veld, kan de invloed van spin-baan wisselwerking en kernspin wisselwerking op het elektron spin volledig worden onderdrukt.

Tenslotte presenteren we in hoofdstuk zeven spin-baan qubits in InAs nanodraden. De spin-baan koppeling is in deze nanodraden dermate groot, dat de spin en de baan van het elektron niet langer los van elkaar kunnen worden gezien. We demonstreren snelle qubit rotaties en de universele enkele-qubit controle met elektrische velden, door de elektronen heen en weer te bewegen in de quantum dot. De beweging van de elektronen veroorzaakt een precessie van spin-op naar spin-neer, met een maximale frequentie van 60 MHz. In een Ramsey experiment meten we de snelheid waarmee de fase-informatie van de superpositie toestand vervalst. De vervaltijd van 8 ns is een indicatie voor de kernspins als voornamelijke bron van decoherentie. De coherentie tijd kan verlengd worden tot  $\sim 200$  ns met dynamische ontkoppelingstechnieken. Tevens zorgt een verschil in grootte tussen de twee quantum dots voor een verschil in Zeeman energie. Dit benutten we door beide qubits selectief te manipuleren met gigahertz elektrische velden.

In dit proefschrift hebben we laten zien dat nanodraden nieuwe mogelijkheden bieden voor het bestuderen van enkele spins in quantum dots. Met de demonstratie van een nanodraad-qubit hebben we een belangrijke nieuwe stap gezet op de weg naar een nanodraad quantum computer. Hier kan het gebruik van nanodraden veel voordelen hebben in vergelijking met andere systemen. Nanodraden kunnen gebruikt worden als een-dimensionale bouwsteen voor opschaalbare qubit registers. Uniek voor nanodraden is de mogelijkheid om eenvoudig de samenstelling van de nanodraad te veranderen tijdens de groei. Deze flexibiliteit kan worden benut om nanodraden met een onderdrukte decoherentie te maken, en hiermee de zuiverheid van de qubit naar de fout-correctie niveau's te brengen. Elektische quantum dots kunnen worden geïntegreerd met optische quantum dots in nanodraden met p-n juncties. De coherentietijden die in dit proefschrift gehaald worden zijn voldoende voor het omzetten van een elektrische qubit naar een foton, een vliegende qubit voor lange-afstand quantum communicatie.

Stevan Nadj-Perge  
November 2010



# CURRICULUM VITAE

Stevan NADJ-PERGE

02-07-1981      Born in Kikinda, Serbia.

## EDUCATION

1996–1998      High school "Dušan Vasiljev"  
Kikinda, Serbia

1998–2000      Mathematical high school  
Belgrade, Serbia

2000–2006      M.Sc. Theoretical Physics  
University of Belgrade, Serbia

2006–2010      Ph.D. research at Delft University of Technology  
under supervision of prof. dr. ir. L. P. Kouwenhoven.  
Subject: *Single spins in semiconductor nanowires*



# LIST OF PUBLICATIONS

1. *Spin-orbit qubit in semiconductor nanowire*  
S. Nadj-Perge, S. M. Frolov, E. P. A. M. Bakkers and L. P. Kouwenhoven,  
Accepted for publication in Nature. (chapter 7 of this theses)
2. *Spin blockade anisotropy in InAs nanowire double quantum dots*  
S. M. Frolov et al.  
in preparation. (chapter 6 of this thesis)
3. *Disentangling the effects of spin-orbit and hyperfine interactions on spin blockade*  
S. Nadj-Perge, S. M. Frolov, J. W. W. van Tilburg, J. Danon, Yu. V. Nazarov, R. Algra, E. P. A. M. Bakkers and L. P. Kouwenhoven,  
Phys. Rev. B **81**, 201305(R) (2010). (chapter 5 of this thesis)
4. *Anisotropic g-factor in a single electron nanowire quantum dot*  
S. M. Frolov et al.  
in preparation. (chapter 4 of this thesis)
5. *Diameter-dependent conductance of InAs nanowires*  
M. Scheffler, S. Nadj-Perge, L. P. Kouwenhoven, M. T. Borgström and  
E. P. A. M. Bakkers,  
J. Appl. Phys. **106**, 124303 (2009).
6. *Tunable double quantum dots in InAs nanowires*  
M. Scheffler, S. Nadj-Perge, L. P. Kouwenhoven, M. T. Borgström, and  
E. P. A. M. Bakkers,  
Physica E **40**, 1202 (2008).
7. *Bistability in superconducting rings containing an inhomogeneous Josephson junction*  
M. Gaass, S. Nadj-Perge, Z. Radović, A. Bauer, M. Aprili, W. Wegscheider, and C. Strunk  
Phys. Rev. B **77**, 024506 (2008)

# Propositions

accompanying the dissertation

## SINGLE SPINS IN SEMICONDUCTOR NANOWIRES

by

**Stevan NADJ-PERGE**

1. To improve spin-orbit qubits in nanowires, materials with stronger spin-orbit interaction compared to InAs should be considered (Chapters 7 and 8 of this thesis).
2. Refusing religious and cultural diversity is not sustainable.
3. Excluding non-free software from the scientific community would increase the productivity of researchers.
4. Although a quantum computer may not calculate anything useful within the coming 50 years, the development of such a computer will definitely change society within this period.
5. In order to speed up the development of nanoscience, more effort should be invested in new nanofabrication techniques.
6. Academic publishing would be more efficient and more fair if there were no scientific journals.
7. Since the clearest messages come in the form of one-liners, physicists will keep inventing new expressions.
8. Dull politics is a reflection of a well-functioning democracy, therefore one should not wish for an exciting political scene.
9. Introducing mandatory voting is the fastest way to increase awareness of the importance of politics.
10. Planning to complete a PhD project on time is like planning to win a boxing match in the second round.

These propositions are regarded as opposable and defensible, and have been approved as such by the supervisor prof. dr. ir. L. P. Kouwenhoven.

# Stellingen

behorende bij het proefschrift

## **SINGLE SPINS IN SEMICONDUCTOR NANOWIRES**

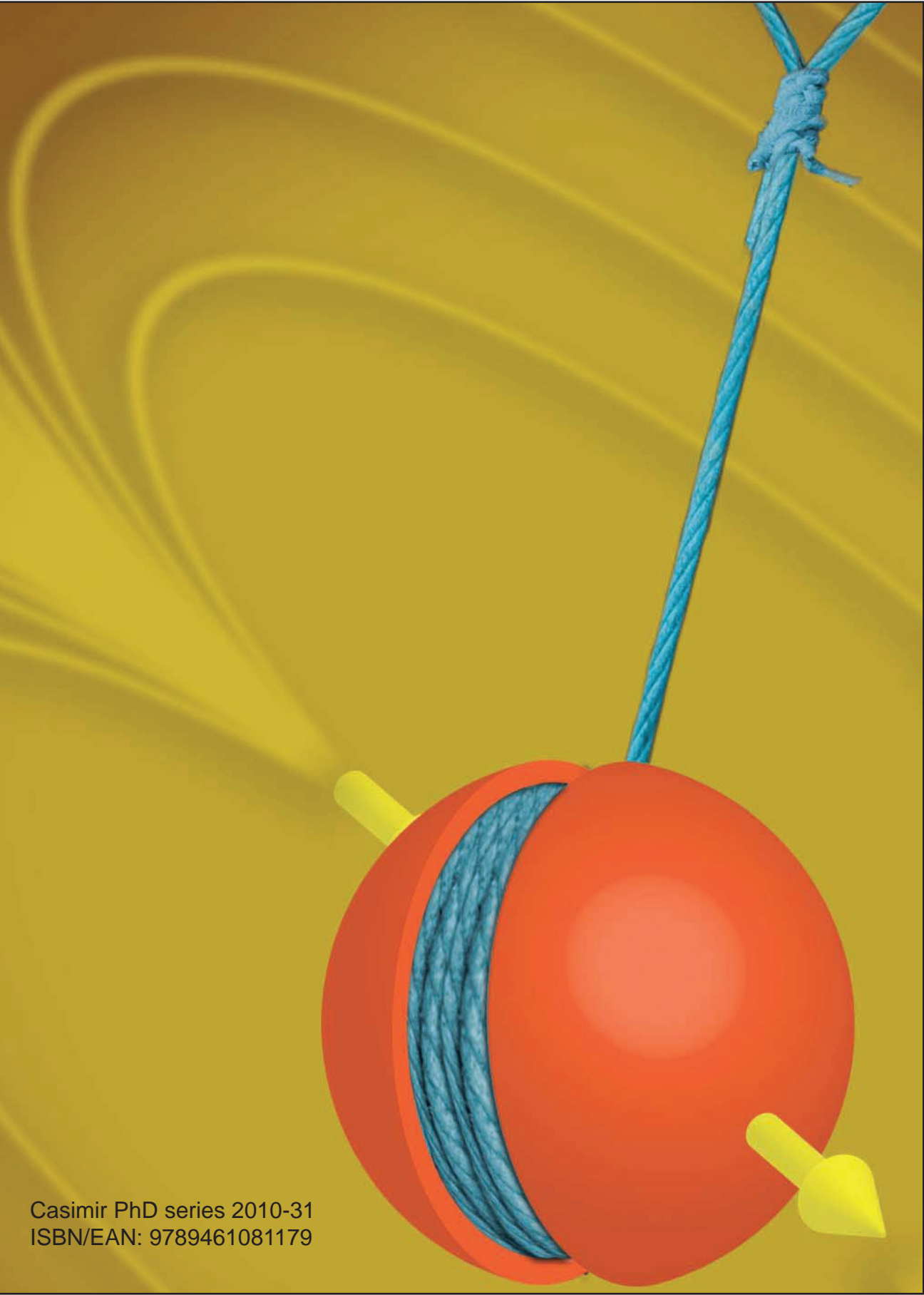
door

**Stevan NADJ-PERGE**

1. Om de spin-orbit qubits in nanodraden te verbeteren, zal het gebruik van materialen met sterkere spin-orbit interacties dan in InAs, in overweging genomen moeten worden (Hoofdstuk 7 en 8 van dit proefschrift).
2. Ontkennen van religieuze en culturele diversiteit is niet duurzaam.
3. Het onttrekken van niet-gratis software uit de wetenschappelijke gemeenschap zal de productiviteit van de onderzoekers verhogen.
4. Alhoewel een quantum computer de komende 50 jaar niets nuttigs zal berekenen, gaat de ontwikkeling van een dergelijke computer de maatschappij in dezelfde periode zeker beïnvloeden.
5. Om de ontwikkeling van nanoscience te bespoedigen, zou er meer geïnvesteerd moeten worden in nanofabricage technieken.
6. Het proces van academische publicatie zou efficiënter en eerlijker verlopen indien wetenschappelijke vakbladen niet zouden bestaan.
7. Aangezien de duidelijkste boodschappen in onliners verschijnen, zullen fysici doorgaan met het uitvinden van nieuwe termen.
8. Saaie politiek is een kenmerk van een goed functionerende democratie; daarom moet men niet verlangen naar spannende politieke taferelen.
9. Het introduceren van actieve kiesplicht, is de snelste manier om het algemene bewustzijn van het belang van politiek te vergroten.
10. Het voornemen om een PhD project op tijd te voltooien is vergelijkbaar met het voornemen een boxwedstrijd al in de tweede ronde te winnen.

Deze stellingen worden oponeerbaar end verdedigbaar geacht en zijn als zodanig goedgekeurd door de promotor prof. dr. ir. L. P. Kouwenhoven.





Casimir PhD series 2010-31  
ISBN/EAN: 9789461081179